

# Instability analysis of perovskite solar cells via short-circuit impedance spectroscopy: A case study on $\text{NiO}_x$ passivation

Cite as: J. Appl. Phys. 136, 094502 (2024); doi: 10.1063/5.0216983

Submitted: 2 May 2024 · Accepted: 16 August 2024 ·

Published Online: 4 September 2024



View Online



Export Citation



CrossMark

Osbel Almora,<sup>1,a)</sup> Pilar López-Varo,<sup>2,a)</sup> Renán Escalante,<sup>3</sup> John Mohanraj,<sup>4</sup> Lluís F. Marsal,<sup>1</sup> Selina Olthof,<sup>4</sup> and Juan A. Anta<sup>3,a)</sup>

## AFFILIATIONS

<sup>1</sup> Departament d'Enginyeria Electrònica i Automàtica, Universitat Rovira i Virgili, 43007 Tarragona, Spain

<sup>2</sup> Institut Photovoltaïque d'Ile-de-France (IPVF), 91120 Palaiseau, France

<sup>3</sup> Department of Physical, Chemical and Natural Systems, Universidad Pablo de Olavide, Sevilla 41013, Spain

<sup>4</sup> Department of Chemistry, University of Cologne, Greinstraße 4–6, Cologne 50939, Germany

<sup>a)</sup> Authors to whom correspondence should be addressed: osbel.almora@urv.cat, pilar.lopez-varo@ipvf.fr, and jaantmon@upo.es

## ABSTRACT

Perovskite solar cells (PSCs) continue to be the “front runner” technology among emerging photovoltaic devices in terms of power conversion efficiency and versatility of applications. However, improving stability and understanding their relationship with their ionic-electronic transport mechanisms continue to be challenging. In this work, a case study of  $\text{NiO}_x$ -based inverted PSCs and the effect of different interface passivating treatments on device performance is presented. Impedance spectroscopy (IS) measurements in short-circuit conditions were performed under different illumination intensities, as well as bias-stress operational stability tests under constant illumination intensity. Surface treatments that involved bulky Lewis bases resulted in better and more stable performance. In contrast, acidic anion donors could induce both an initial performance decrease with a characteristic three-arcs impedance Nyquist plot and a subsequent instability during light exposure. Drift-diffusion simulations suggest strong modifications of surface recombination at the interface with the hole transport material, and for the ion concentration and mobilities in the perovskite. Importantly, capacitance and resistance are shown to peak maximum and minimum values, respectively, around mobile ion concentration ( $N_{\text{ion}}$ ) of  $10^{16}$  and  $10^{17} \text{ cm}^{-3}$ . These features relate to the transition from a drift-, for low  $N_{\text{ion}}$  below a threshold value, to a diffusion-dominated transport in the bulk of the perovskite, for high  $N_{\text{ion}}$  beyond the threshold value. Our results introduce a general route for characterization of instability paths in PSCs via IS performed under short-circuit conditions.

14 September 2024 06:40:10

© 2024 Author(s). All article content, except where otherwise noted, is licensed under a Creative Commons Attribution-NonCommercial 4.0 International (CC BY-NC) license (<https://creativecommons.org/licenses/by-nc/4.0/>). <https://doi.org/10.1063/5.0216983>

## I. INTRODUCTION

The optimal optoelectronic properties of metal-halide perovskites have gained major attention of the semiconductor device research community during the last decade resulting in unprecedented progress in several fields, such as photovoltaics,<sup>1</sup> light emitting diodes,<sup>2</sup> lasers,<sup>3</sup> and ionizing radiation detectors.<sup>4</sup> Particularly, single junction perovskite solar cells (PSCs) with record power conversion efficiency (PCE) values >25% made by low-cost solution-based fabrications methods have been reported. These multilayer devices consist of an intrinsic halide perovskite absorber layer that is

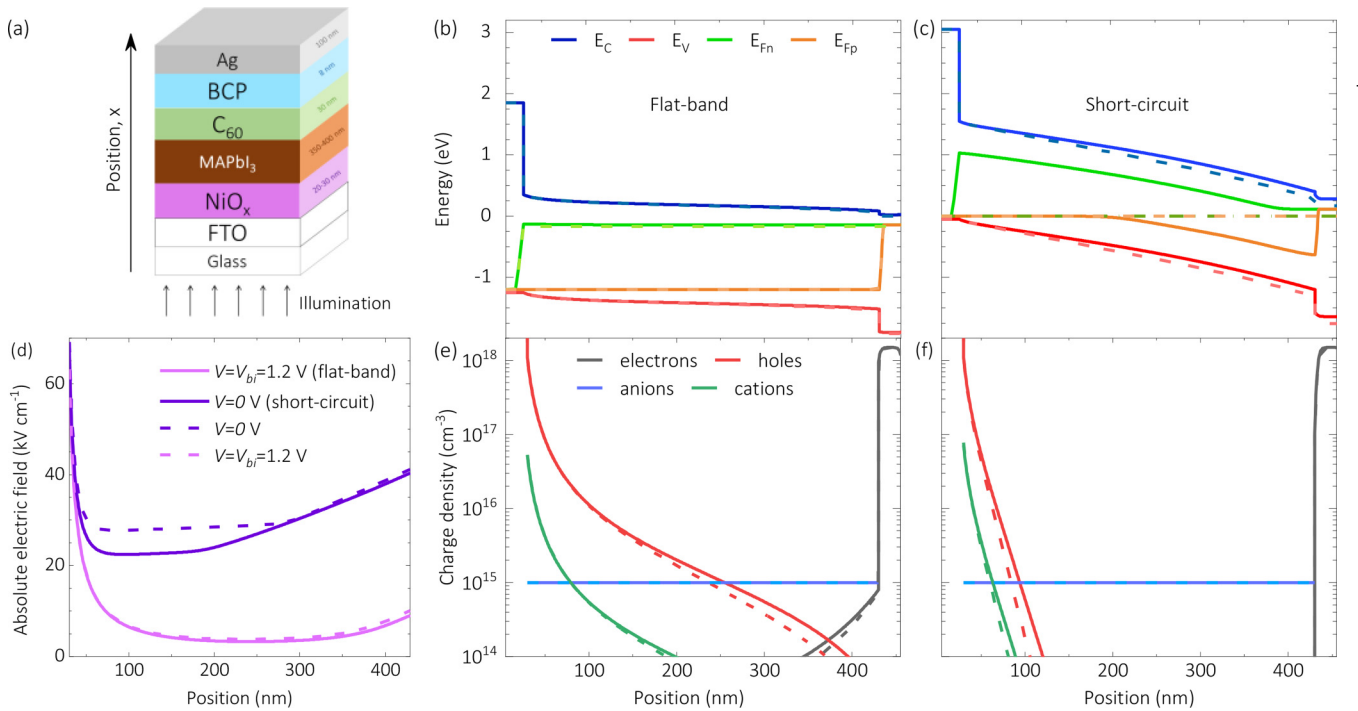
sandwiched between the electron and hole transport layers, ETL and HTL, respectively. In addition, compatibility with different substrates has produced a broad range of versatile applications, for instance, in transparent/semitransparent and flexible photovoltaics. However, an understanding of the working mechanisms of these devices is still limited. Particularly, the long-term operational stability issues in PSCs, which remain a key limiting factor for upscaling and industrial deployment, are still in the early phases of elucidation.<sup>5</sup>

The long-term instability of thin film devices, such as PSCs, is a complex process that depends on several mechanisms, parameters,

and constituting elements [see Figs. S1(a) and S1(b) in the supplementary material]. Under operational conditions, instability originates from chemical reactions creating oxidation and/or unintended products between the pristine materials and reactant leftovers of each layer,<sup>6,7</sup> interfaces,<sup>8</sup> and the air (e.g., humidity) in operational conditions.<sup>9,10</sup> Moreover, reactivity can be catalyzed and/or triggered by mechanical,<sup>9</sup> thermal,<sup>9–11</sup> and bias<sup>11–14</sup> stresses as well as photon interactions.<sup>5,9,15</sup> In addition to reactivity, the material's crystal structure of each layer and the interfaces can be modified, creating undesired defects that reduce photon absorption and enhance charge carrier recombination.<sup>16</sup> Among these non-reactive sources of defects, one can find temperature stress and the migration of various species inside the layer due to either diffusion, illumination, or the application of electrical stress.<sup>13,14,17,18</sup> Notably, species from different layers within the device can migrate, increasing the leakage current.<sup>19</sup> Additionally, ion migration of intrinsic halide vacancies and other charged defects<sup>20,21</sup> has been demonstrated in halide perovskites.<sup>22</sup> Remarkably, Thiesbrummel *et al.*<sup>23</sup> recently proposed that extra mobile ions are created during light and electrical stress, whose resultant field screening is a dominant factor leading to lower operational stability of PSCs. Therefore, assessing the individual contribution of each mechanism and element in the device is challenging, which motivates the design of

experiments where one can neglect some of the degradation agents. In this context, the use of advanced characterization techniques [beyond the routine measurement of current density-voltage ( $J - V$ ) curves] supported by numerical device simulation allows for the investigation of ionic transport properties, thermal and photo-stability, and mechanical durability.

In the literature, the device architectures of PSCs are identified as p-i-n or n-i-p depending on whether the HTL or the ETL is positioned first in the direction of the incident light path, respectively. Particularly, p-i-n structures, also known as inverted PSCs, have reported efficiencies over 25%<sup>24,25</sup> and are attractive due to their low-temperature fabrication methods<sup>26</sup> and compatibility with existing industrial techniques.<sup>27</sup> An example of such a device structure is schemed in Fig. 1(a), where non-stoichiometric nickel oxide ( $\text{NiO}_x$ ) is chosen as inorganic HTL and organic semiconductor films comprised of  $\text{C}_{60}$  and bathocuproine (BCP) serve as ETL and hole blocking layers, respectively. The use of organic ETLs in inverted PSCs has been suggested because of the facile low-temperature synthesis with orthogonal solvents and purification methods resulting in optimal performance with relatively low instability.<sup>29</sup> In addition, the fact that the p-i-n structure places the ETL behind the absorber perovskite in the direction of the light path reduces the radiative and, to some extent, temperature stresses



14 September 2024 06:40:10

**FIG. 1.** Simulated steady-state electrical response of the reference PSCs with the structure in (a) in terms of energy diagrams [(b) and (c)], electric field (d), and charge density profiles [(e) and (f)]. The depicted conditions include flatband [(b) and (e)], short-circuit [(c) and (f)], 1 sun illumination (solid lines) and dark (dashed lines). In (b) and (c),  $E_C$  and  $E_V$  are the conduction band minimum and valence band maximum energy levels, respectively, and  $E_{Fn}$  and  $E_{Fp}$  are the quasi-Fermi levels for electrons and holes, respectively. In (d),  $V_{bi}$  is the built-in voltage. In (e) and (f), the densities are  $n$ ,  $p$ ,  $a$ , and  $c$  for electrons, holes, mobile anions, and mobile cations, respectively. SETFOS Fluxim<sup>28</sup> was used for these simulations, assuming a mobile ion concentration of  $10^{15} \text{ cm}^{-3}$ .

on the organic ETL. On the other hand, the use of  $\text{NiO}_x$  is proposed considering the already demonstrated PCE values over 24% when incorporating  $\text{NiO}_x$  as a HTL.<sup>30,31</sup>

The direct contact between as-prepared  $\text{NiO}_x$  and perovskite has proven to be problematic for solar cell efficiency and stability, as, for example, summarized in the recent review by Cai *et al.*<sup>32</sup> To circumvent this issue, the  $\text{NiO}_x$ /perovskite interface has been optimized via several materials and fabrication methods. For instance, the energy level alignment between  $\text{NiO}_x$  and the perovskite has been optimized with the introduction of inorganic extrinsic doping such as the case of Wang *et al.*,<sup>33</sup> who sited Ag via a sol-gel method and Yi *et al.*,<sup>34</sup> who fabricated nanopatterned Zn: $\text{NiO}_x$  with an advantageous 1D nanoscale architecture and synergistic substitutional Zn doping. Alternatively, Hu *et al.*<sup>35</sup> used organic doping by including 4-tert-butylpyridine (tBP) as an additive in the  $\text{NiO}_x$  precursor solution, whereas Kang *et al.*<sup>36</sup> used 4-iodophenylboronic acids to modify the  $\text{NiO}_x$ /perovskite layer interface, believed to be affected by the intrinsic defects (Ni vacancies) in the  $\text{NiO}_x$  film and iodine vacancies at the buried interface of the perovskite. Similarly, high-performance devices were reported by Wang *et al.*,<sup>31</sup> who utilized a multi-fluorine organic molecule 6FPPY to optimize the buried interface of  $\text{NiO}_x$ -based p-i-n PSC. Notably, Pu *et al.*<sup>30</sup> introduced a poly[bis(4phenyl)(2,4,6-trimethylphenyl)amine] (PTAA) interlayer between  $\text{NiO}_x$  and the perovskite, resulting in high efficiency and stability. Furthermore, Shen *et al.*<sup>37</sup> proposed that the hydrophilic chain of the amphiphilic molecule Triton X100 can coordinate as a Lewis additive with  $\text{Ni}^{3+}$  on the  $\text{NiO}_x$  surface, passivating interfacial defects and hindering the detrimental reactions at the  $\text{NiO}_x$ /perovskite interface.

From the device operation point of view, the degradation of a solar cell is commonly associated with the decrease of PCE, as measured from the current density–voltage ( $J - V$ ) curve under standard 1 sun illumination incident power density ( $P_{in}$ ). The PCE value can be expressed in terms of the complementary performance parameters as  $PCE = V_{oc}J_{sc}FF/P_{in}$ , where  $V_{oc}$  is the open-circuit voltage,  $J_{sc}$  is the short-circuit current density, and FF is the fill factor. Accordingly, a decrease in PCE can be correlated with a decline in one or more of the aforementioned performance parameters [see Figs. S1(c)–S1(i) in the [supplementary material](#)]. In practice, FF and  $V_{oc}$  modifications are more likely to be correlated since these parameters relate to the near-flatband condition where the charge carrier recombination rate approaches that of the photogenerated. Note that under illumination intensities close to and above 1 sun standard, high-performance devices is typically expected to achieve a maximum power point (MPP) voltage  $V_{mpp} < V_{oc}$  in a bias range near the built-in voltage ( $V_{bi}$ ). In contrast, as the illumination intensity decreases, the values of  $V_{mpp}$  and  $V_{oc}$  move further away from that of  $V_{bi}$ .<sup>38</sup>

The near-flatband regime occurs for forward bias in a vicinity  $\delta$  near  $V_{bi}$ , with  $\delta$  typically smaller than ten times the thermal voltage ( $k_B T/q$ ). In this regime, the energy diagram is expected to resemble that shown in Fig. 1(b), which was calculated for the device structure depicted in Fig. 1(a) (see simulation parameters in Table S8 in the [supplementary material](#)). Moreover, diffusion current is comparable to, or even larger than, drift current due to the lower electric field [see Fig. 1(d)]. This results in wider

gradients in charge carrier density profiles [see Fig. 1(e)]. Diffusion-related long-term relaxations, such as ion migration, may overlap with degradation processes like oxidation, segregation, and amorphization.<sup>39</sup> Then, a question may arise on whether an unstable signal is due to slow mobile ions or because of material reactivity and degradation. Moreover, illumination intensity is not expected to produce significant changes in the energy diagram near the flatband condition [dashed lines close to solid lines in Figs. 1(b), 1(d), and 1(e)]. More importantly, radiative recombination is the main contributor to the current, which hinders the evaluation of non-radiative losses. In addition, dual electronic-ionic conductivity of metal halide perovskites not only hinders the evaluation of the MPP, which defines the FF, but also complicates transport by adding field screening by ions<sup>40</sup> to a regime where diffusion transport would otherwise be more dominant.<sup>41</sup> The field screening effect can be seen to some extent in Fig. 1(d) when comparing the lower values of the absolute electric field within the bulk of the perovskite with those toward the interfaces, for mobile ion concentrations of  $N_{ion} = 10^{15} \text{ cm}^{-3}$ . Nevertheless, it is with the increase of mobile ion density that the electric field is screened, as presented in Figs. S2(a) and S2(b) in the [supplementary material](#) for  $N_{ion} = 10^{18} \text{ cm}^{-3}$ . In summary, in the near-flatband condition, several effects may mutually mask one contribution on the other, thereby hindering the interpretation. Accordingly, despite solar cells operate close to the flatband condition, it may be convenient to explore another biasing regime for better understanding of the different contributions to device performance and stability.

At the short-circuit condition ( $V = 0 \text{ V}$ ), the electric field in the perovskite bulk is significantly higher and sensitive to the illumination intensity [see Fig. 1(d)]. Under illumination, this is a regime where the drift current and nonradiative recombination toward the interfaces is predominant due to band leaning [see Fig. 1(c)] and the lower concentrations of charge carriers located within the perovskite near the transport selective layers [see Fig. 1(f)]. In addition, the short-circuit and reverse bias regimes are commonly used for the characterization of shunt resistance, which is a parameter typically affected during long-term operation. Interestingly, PSCs have shown linear photo-shunt resistance<sup>42</sup> (see Table S1 in the [supplementary material](#) for a similar effect in other solar cells) and photo-capacitive<sup>43</sup> increase under short-circuit conditions, which can be characterized via impedance spectroscopy (IS). Notably, the use of IS analyses under short-circuit conditions is preferable due to the higher linearity of the signal response, compared to IS analysis near the flatband condition. Moreover, unlike the IS studies in quasi-open-circuit conditions,<sup>44–47</sup> little attention has been paid in the literature to the IS spectra measured under short-circuit conditions for PSCs with notable exceptions on charge extraction experiments.<sup>48</sup>

The comparison between the short-circuit and near flatband regimes is summarized in Table I, from which one can assess the suitability of each condition for designing experiments, with special focus on studies about stability.<sup>56–62</sup> Notably, the relation between external bias  $V$  and  $V_{bi}$  is illustrative for analyzing each parameter. For instance, the energy diagrams, and drift and diffusion current profiles are compared in Figs. S2(c)–S2(f) in the [supplementary material](#) for low mobile ion density. Under short-circuit conditions, the drift current is much higher than the diffusion current through

**TABLE I.** Comparative summary between short-circuit and near-flatband conditions in perovskite solar cells (with low concentration of mobile ions:  $N_{ion} < 10^{16} \text{ cm}^{-3}$ ).

Properties	Short-circuit	Near-flatband
Bias	$V = 0 \text{ V}$	$V = V_{bi} \pm \delta, \delta \sim 10 \text{ k}_B T/q$
PCE-related parameters <sup>a,49,50</sup>	$J_{sc}$	$V_{oc}, FF, V_{mpp}$
Drift vs diffusion transport <sup>a,50</sup>	Drift $\gg$ Diffusion*	Diffusion $\geq$ Drift
Recombination <sup>a,49,51</sup>	Radiative $\ll$ Nonradiative	Radiative $\gg$ Nonradiative
Mobile ion distribution in the bulk of the perovskite <sup>b,52–55</sup>	Narrower	Wider
Time response <sup>c,47,54</sup>	Faster	Slower
Linearity of the current–voltage curve <sup>47,49</sup>	Higher	Lower
Parasitic resistance <sup>a,47,50</sup>	$R_{sh}$	$R_s$

<sup>a</sup>Relative main contribution.<sup>b</sup>Near the interfaces.<sup>c</sup>Slowest ion related.<sup>\*</sup>In this work, we find that drift  $\ll$  diffusion in the bulk of the perovskite for high concentrations of mobile ions:  $N_{ion} > 10^{18} \text{ cm}^{-3}$ .

the bulk of the perovskite. In the absence of external forward bias, the main current driver is the built-in field. Additionally, under short-circuit conditions, thin selective contacts are fully depleted, and the field extends along the entire device, which shows the typical absence of the quasi-neutral region. In contrast, forward bias near-flatband conditions can reduce, or even cancel, the electric field. Shrinking of the depletion regions up to their Debye lengths creates quasi-neutral regions in the selective transport layers toward the electrodes, where diffusion becomes the main transport mechanism. In the perovskite, the balance between the small electric field-generated drift and small charge carrier density gradients-caused diffusion is illustrated in Fig. S2(f) in the **supplementary material**, where the diffusion current is only slightly higher than the drift current in certain regions. Moreover, the  $J_{sc}$  transient response time is typically on the order of seconds, as it is dominated by electronic non-radiative recombination.<sup>41,47,51,63</sup> On the other hand, slower ion-related processes arise when  $V \rightarrow V_{bi}$ , producing slower  $V_{oc}$  decays up to the order of hours, although the typical electronic radiative recombination lifetime decreases exponentially with the increase in charge carrier concentration.<sup>4,64–66</sup>

The stability tests for PSCs are typically performed at the MPP, which simulates the ideal operation regime for devices.<sup>67,68</sup> However, in practice, device operation includes bias changes due to variations in the illumination intensity and load, which trigger different degradation mechanisms.<sup>69</sup> In fact, faster PCE decays have been identified when the device is held under continuous illumination at open-circuit or short-circuit conditions in comparison to the case where the device bias is held near the MPP point.<sup>13,70,71</sup> Furthermore, the report of higher long-term stability of photoluminescence in short-circuit, in comparison to that in open-circuit and at MPP,<sup>12</sup> suggests a major contribution of degradation of charge carrier transport properties to the decrease of PCE in short-circuit.

In this work, we investigate the stability of passivated-NiO<sub>x</sub>/MAPbI<sub>3</sub>-PSCs as a suitable case study for analyzing the interface between the HTL and the perovskite layer, as well as the evolution of electrical properties. In a separate publication, these passivating surface treatments of NiO<sub>x</sub> have already been studied with respect to film formation, interface composition, and solar cell initial performance and stability.<sup>72</sup> In contrast, the focus here is set on

modeling and understanding of fundamental transport properties. Experimentally, current evolution over time under near MPP conditions was monitored for several passivation methods targeting the interface between the NiO<sub>x</sub> selective layer and the MAPbI<sub>3</sub> absorber layer. Moreover, IS spectra were measured over time and under different illumination intensities at short-circuit in each case. A novel combination of long-term biasing at voltages close to the MPP with systematic switch to short-circuit for IS measurements was introduced as a bias-stress stability test. The results were contrasted with equivalent circuit (EC) modeling and numerical simulations on SETFOS Fluxim<sup>28</sup> and *Driftfusion*<sup>73</sup> transport equation solvers. Our results correlate different modifications in electron and mobile ion concentrations and mobilities with degradation observed in the samples.

## II. METHODS

Fabrication details for the studied devices with structure FTO/NiO<sub>x</sub>/MAPbI<sub>3</sub>/C<sub>60</sub>/BCP/Ag [see Fig. 1(a)] can be found elsewhere.<sup>72</sup> The process is summarized in Sec. S2 (**supplementary material**) along with the J-V curves and PCE experimental results (see Fig. S4 and Table S2 in the **supplementary material**). For passivation, the selected materials distribute into three categories attending to the potential conductivity effect, as discussed in more detail in Ref. 72. First, PbI<sub>2</sub> is introduced as a cation donor, which is a metallic salt with the divalent Pb cation that may potentially occupy Ni<sup>2+</sup> vacant sites and corresponding anions, to interact with high valent (>2+) Ni centers. Second, 1-iodobutane (C<sub>4</sub>H<sub>9</sub>I, also labeled here as iodobutane) and 1-phenylethylamine (C<sub>8</sub>H<sub>11</sub>N, also labeled here as amine) neutral bases, which are Lewis bases, i.e., neutral organic molecules with a capacity to donate electron pairs to Ni atoms with higher formal charge (>2+). Third, HI and MAI protic anion donors, i.e., Brönsted (Lewis) acids, which are organic molecules that could donate protons (or accept electron pairs) to O atoms with increased formal charge due to Ni<sup>2+</sup> vacancies (O-defect sites) and anions to interact with Ni<sup>>2+</sup>.

The IS data were measured with an Autolab PGSTAT302N potentiostat including a FRA32M unit and a kit Autolab Optical Bench from MetroOhm. The samples were illuminated with a

white LED (CREE XM-L3 U4 on star PCB, XMLDWT-U40E1) at different steady-state illumination intensities; then, the short-circuit current was stabilized before applying 15 mV of alternating current (AC) mode perturbation. The details for IS characterization under different illumination intensities are in Sec. S3 in the [supplementary material](#). Stability assessment was carried out under 0.2 sun equivalent illumination intensity, as measured with a calibrated reference cell 91150-112/PVM 164 from Newport. The samples were under continuous N<sub>2</sub> flux at room temperature and were kept in operation at a forward bias close MPP under illumination with systematic switching to short-circuit for IS measurements (see Fig. S16 in the [supplementary material](#)). Section S4 in the [supplementary material](#) provides further details on the operational stability test procedure and current and IS data.

Equivalent circuit modeling was carried out with ZView from Scribner. Details of all equivalent circuits and fitting parameters can be found in Secs. S3 and S4 in the [supplementary material](#). SETFOS Fluxim<sup>28</sup> software and MATLAB's *Driftfusion*<sup>73</sup> code were used for the numerical simulations of the time-dependent solutions of transport equations with electronic and mobile ion charge carriers. The corresponding details can be found in Secs. S5 (Figs. S23–S31) and S6 (Figs. S31–S55) in the [supplementary material](#).

A complementary characterization with focus on the reactivity and materials properties of a similar batch of devices can also be found elsewhere,<sup>72</sup> including morphological, crystallographic x-ray diffraction, x-ray photoelectron spectroscopy, operational stability tests under 1 sun illumination, IS in quasi-open-circuit condition under different illumination intensities, and photovoltage decay experiments.

### III. RESULTS AND DISCUSSION

The different NiO<sub>x</sub> surface treatments employed in various samples in this study resulted in two main behaviors, as seen in the solar cell characteristics presented in Fig. S4 in the [supplementary material](#). On the one hand, NiO<sub>x</sub> surface passivation with 1-iodobutane, 1-phenylethylamine, and PbI<sub>2</sub> improved the performance mostly due to a slight increase in the photocurrent. The resultant PCE values ranged around 13% for the un-passivated reference sample (NiO<sub>x</sub> Ref.) and nearly 15% for the passivated samples, in line with state-of-the-art pure MAPbI<sub>3</sub> NiO<sub>x</sub>-based PSCs.<sup>74,75</sup> This suggests that the treatment with these passivation agents could reduce electrical losses due to charge carrier recombination at the interface. Nevertheless, these passivation processes could also modify the morphology and optoelectronic properties of the perovskite layers, resulting in further effects such as the reduction of optical losses due to interference and the decrease of bulk recombination in the perovskite. On the other hand, the MAI and HI passivated samples showed a significant PCE decrease to less than 6% due to the reduction of the fill factor and the photocurrent. The absence of rectifying behavior in these samples indicate major modifications of the charge carrier density profiles, large parasitic resistive effects, and large recombination rates.

For the understanding of these two different behaviors, complementary experiments were performed with a focus on the short-circuit condition, different illumination intensities, and IS analysis. This is presented in Secs. III A and S3 in the [supplementary](#)

material, where equivalent circuit modeling is used to estimate resistive, capacitive, and characteristic response times. Subsequently, the experiments on operational stability and the evolution of the IS spectra over time under constant illumination are presented in Secs. III B and S4 in the [supplementary material](#). Moreover, further analysis was conducted via drift diffusion simulation, as presented in Secs. III C and S5–S6 in the [supplementary material](#).

#### A. Different illumination intensities in short-circuit

The impedance ( $Z$ ) spectra under different illumination intensities were measured under short-circuit conditions for representative samples of the studied device set with different passivation treatments on the NiO<sub>x</sub> interface with the perovskite, as described in Sec. S3 in the [supplementary material](#) and summarized in [Fig. 2](#). The characteristic two-arcs spectra in the impedance Nyquist plots are present in the reference and optimized samples (amine, iodobutane, and PbI<sub>2</sub>), as indicated in [Fig. 2\(a\)](#). Typically, the high- and low-frequency semicircles relate to electronic and ionic-electronic resistance ( $R$ )–capacitance ( $C$ ) contributions, respectively. In the capacitance Bode plot representation, two plateaus can be identified [see [Fig. 2\(c\)](#)], where the nearly constant values toward high-frequency ( $H_f > 10$  kHz) are related to the geometrical dielectric capacitance<sup>46</sup> and the capacitance step-like increase toward low-frequency ( $L_f < 10$  Hz) has been associated with electrode polarization and mobile ion accumulation at the interfaces.<sup>47</sup> However, the HI and MAI samples not only demonstrate smaller resistances in SC but also show three arcs in the impedance Nyquist representation [see [Figs. 2\(a\)](#) and S18 in the [supplementary material](#)] and a gradual capacitance increase in the capacitance Bode plot [see [Fig. 2\(c\)](#)]. Notably, the higher the illumination intensity, the clearer the definition of the three arcs in the Nyquist plot. This behavior agrees with recent simulations by Clarke *et al.*,<sup>45</sup> which suggest that high concentrations of charge carriers are needed for a three-arc spectrum. Then, a transition from a “two (larger)” to a “three (smaller)” arcs situation complicates the “high-frequency electronic” vs “low-frequency ionic” interpretation of the IS spectra.

The equivalent circuit (EC) models used for parameterization of the IS spectra are shown in [Fig. 2\(a\)](#) for the two- and three-RC constants, respectively. For the reference and optimized samples, two resistors and two capacitors were fitted for the high- and low-frequency features of the spectra as  $R_{Hf}$ ,  $R_{Lf}$ ,  $C_{Hf}$ , and  $C_{Lf}$ , respectively. In contrast, for the MAI- and HI-treated samples, an additional set of medium-frequency resistors ( $R_{Mf}$ ) and capacitors ( $C_{Mf}$ ) were considered. Moreover, the resistance is further analyzed in Sec. S3 and Fig. S5 in the [supplementary material](#) via ECs, with particular focus on the shunt resistance ( $R_{sh}$ ) and that of the diode ( $R_d$ ).

Qualitative and quantitative differences are illustrated in the Nyquist plots of [Fig. 2\(a\)](#), and the resultant values for the resistances as a function of the short-circuit current under different illumination intensities are summarized in [Fig. 2\(b\)](#). First, in general, all samples and either Hf or Lf follow a similar trend where saturation is observed toward the dark condition and a decrease in  $R \propto J_{sc}^{-1}$  follows as the illumination intensity increases up to 0.2 sun (white LED equivalent). This is a common trend in photovoltaic

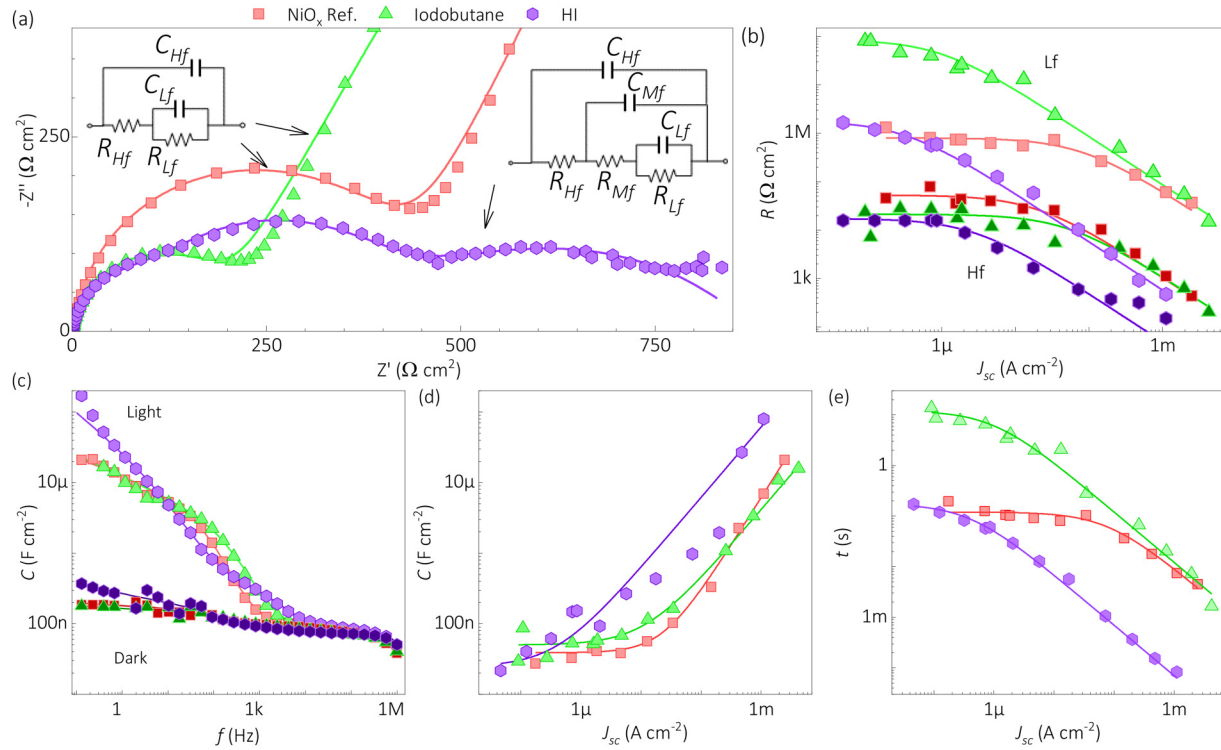


**FIG. 2.** Experimental selected IS spectra under different illumination intensities (up to 0.2 sun equivalent LED light) in short-circuit conditions ( $V=0$  V) for illustrative samples with different passivation procedures, as indicated, and equivalent circuit parameterization. In (a), there are impedance Nyquist plots under 0.2 sun equivalent LED light and (c) shows the capacitance Bode plots in perspective with the dark spectra (darker dots). Solid lines in (a) and (b) are the fitting to the equivalent circuits in the inset of (a), in each case. The corresponding (b) resistance, (d) capacitance (low-frequency), and (e) characteristic response times (low-frequency) are plotted in the lower panel with darker and lighter dot fill colors for high and low-frequency related components, respectively. The lines in (b), (d), and (e) are empirical fittings introduced in Sec. S3 in the [supplementary material](#).

14 September 2024 08:40:10

solar cells (see Table S1 in the [supplementary material](#)) due to the photoconductivity increase upon charge carrier generation. Second, the  $L_f$  resistance is always higher than that of the  $H_f$  resistance. This may suggest that in the short-circuit condition, ion migration and/or ion-related charge carrier transport is significantly hindered in comparison to the faster “pure” electronic response. Third, the higher the short-circuit resistance, the higher the device operational performance, which agrees with the general effect of  $R_{sh}$ .

The capacitance spectra in Fig. 2(c) show some qualitative differences between samples but a quantitative agreement in general. The  $L_f$  capacitance shows linear increase as a function of short-circuit current ( $C_{L_f} \propto J_{sc}$ ) for different illumination intensities, as illustrated in Fig. 2(d), whereas the constant  $H_f$  capacitance can be found in Sec. S3 in the [supplementary material](#). This increase in  $L_f$  capacitance in short-circuit is a characteristic feature of PSCs<sup>43</sup> due to mobile ion accumulation toward the interfaces [see Fig. 1(f)]. Interestingly, the reference and surface-treated (amine, iodobutane, and  $PbI_2$ ) samples show a threshold illumination value for  $J_{sc} \approx 10^{-5} \text{ A cm}^{-2}$ , indicating a transition between a nearly constant behavior and the linear trend. In contrast, the HI and MAI samples show a gradual increase in  $C_{L_f}$  without an apparent

baseline capacitance in the explored range of illumination intensity. Furthermore, by coupling the capacitors and the corresponding discharge resistors, the characteristic short-circuit charge carrier response times ( $\tau = RC$ ) can be accessed, as presented in Fig. 2(e) for the  $L_f$  times. The  $L_f$  and slower response times can be found in Sec. S3 in the [supplementary material](#), showing nearly linear or slightly increasing trends with the augmentation of illumination intensity. On the other hand, the fastest  $H_f$  response times evolve from saturated maximum values to linear decreasing trends as the illumination intensity increases. This can be interpreted as a transition of the main charge carrier recombination mechanism between non-radiative and radiative, when dark and under illumination, respectively. Notably, the longer the response time, the higher the operational performance of the samples in terms of PCE.

The experimental evidence shown in Fig. 2 and Sec. S3 in the [supplementary material](#) with IS spectra over a range of illumination intensities highlights the paramount importance of the HTL/perovskite interface for device operation. Nevertheless, several aspects require further understanding. For instance, the role of 1-iodobutane, 1-phenylethylamine, and  $PbI_2$  treatments appears to be passivating surface defects and improving the charge extraction by

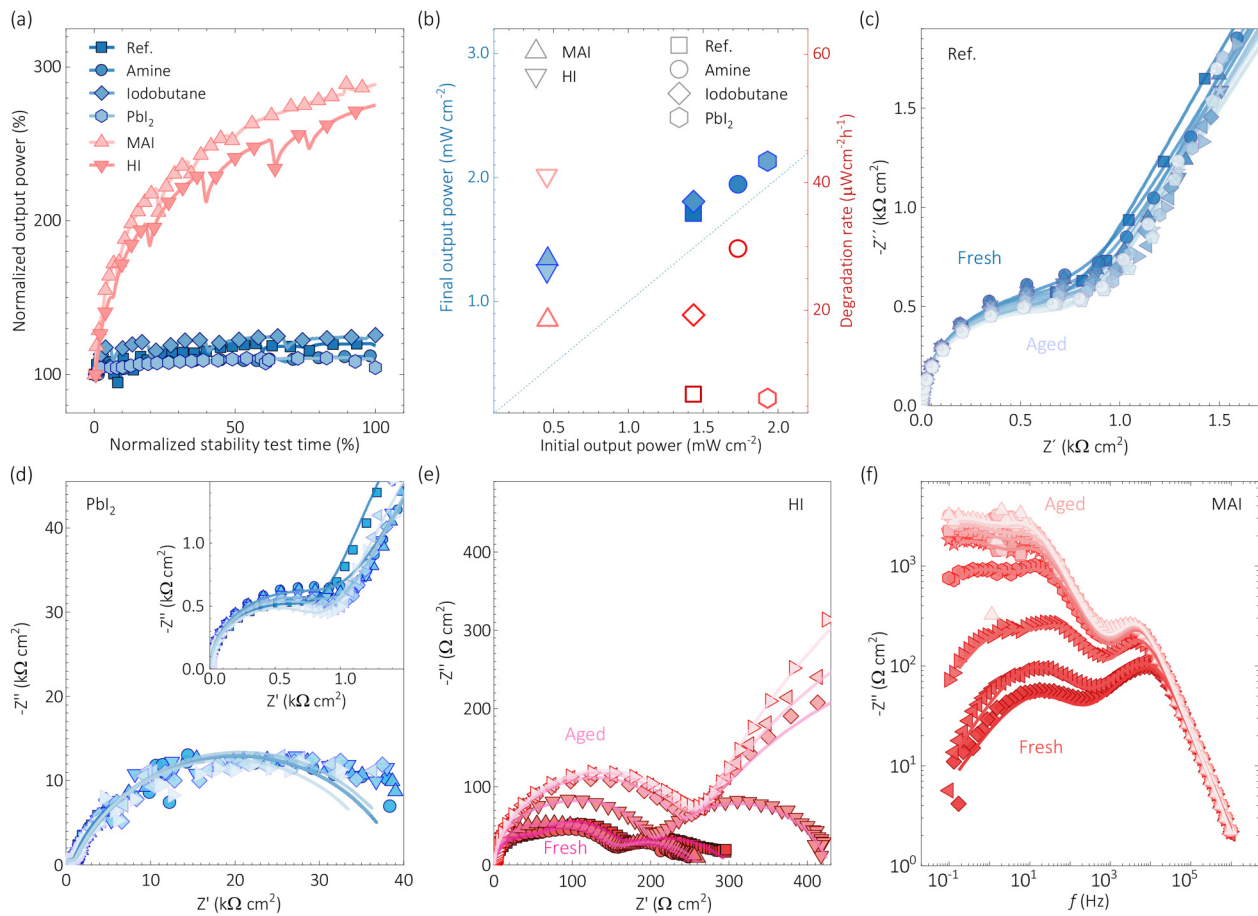
hindering recombination. However, it is unclear how the MAI and HI treatments deteriorate the rectifying barrier, reducing the overall resistance and showing the characteristic “three arcs” in the impedance Nyquist plots. Furthermore, the fact that a large low-frequency impedance arc evolves into two smaller arcs in the Nyquist plot could be related to ion migration and the modification of the nature or concentration of mobile ions and electrons in the perovskite.<sup>72</sup>

### B. Constant illumination over operational time

The operational stability of the samples was studied over time under constant illumination intensity, at room temperature, and with nitrogen flux circulation. The stability tests procedure is schemed and described in detail in Sec. S4 in the [supplementary material](#). The sample was exposed to a constant 0.2 sun (white LED

equivalent) illumination intensity. Next, a voltage  $V_{hpp}$  close to the MPP was applied, and the current was recorded for measuring the output power ( $P_{out}$ ). Subsequently, the biasing was switched to short-circuit, and IS spectra were acquired in each iteration of the loop. This process was continued until the samples broke, and the duration ranged from 20 to 50 h.

The overall  $P_{out}$  performance of the devices is depicted in Fig. 3(a), where two main trends are observed. For the reference and surface-optimized (amine, iodobutane, and  $\text{PbI}_2$ ) samples, a rather stable  $P_{out}$  with a slight increase is detected. On the other hand, the HI- and MAI-treated cells experienced a large increase of  $P_{out}$  with an apparent extrapolated saturation around 300% of the initial value. Nevertheless, despite the final tripled  $P_{out}$  values for the HI and MAI samples, the performance of the reference and optimized cells was still 30%–50% better, as summarized in Figs. 3(b) and S17 in the [supplementary material](#). When comparing final vs initial  $P_{out}$



14 September 2024 06:40:10

**FIG. 3.** Experimental stability test under 0.2 sun white LED equivalent illumination intensity. The normalized time evolution of output power in (a) is summarized in (b) with the final values (left axis, filled symbols) and degradation rates (right axis, open symbols) as a function of the initial output power for each sample, as indicated. Illustrative impedance spectra in short-circuit under constant illumination over operation time are in Nyquist representation in (c)–(e) and Bode plots (f) for different samples, as indicated. Dots and lines are the experimental data and simulated spectra from fitting to equivalent circuit models in Fig. S5 in the [supplementary material](#), respectively. The dashed line in (b) indicates the  $x = y$  coordinates. In (c)–(f), the lighter the color, the longer the operational time in the IS spectra; and the inset in (d) magnifies the high-frequency part of the spectra.

values in this plot, the closer the sample is to the “ $x=y$ ” diagonal [dashed line in Fig. 3(b)], the higher the stability. Alternatively, considering different initial performances and test durations of each sample, one can also use the concept of an effective or overall degradation rate,<sup>1</sup>

$$DR = \frac{P_{\text{out,final}} - P_{\text{out,initial}}}{t_{\text{STD}}}, \quad (1)$$

where  $P_{\text{out,initial}}$  and  $P_{\text{out,final}}$  are the initial and final output powers for the stability test of duration  $t_{\text{STD}}$ . In the definition of Eq. (1), the smaller the absolute value of  $DR$ , the better. Fundamentally,  $DR = \partial P / \partial t$  can also be understood as a measure of instability or reactivity, although it cannot be confused with an instability rate, i.e.,  $\partial DR / \partial t = \partial^2 P / \partial t^2$ . Despite that the typical decrease of performance would entail  $DR < 0$ , the report of  $DR > 0$  during the first 200 h of operation under constant illumination is well known in the literature<sup>1</sup> and typically precedes a subsequent performance decrease period with  $DR < 0$ . Therefore, a distinction is highlighted here between solar cell performance degradation and generic degradation of a material or device. Solar cell performance degradation is always understood as a decrease of PCE that leads to  $DR < 0$ . In contrast, a device or material degradation is, herein, discussed in terms of the relative change with respect to an initial state, i.e.,  $DR \neq 0$ , in such a way that a degradation process can include periods with apparent increase ( $DR > 0$ ) or decrease ( $DR < 0$ ) in performance.

The studied samples show  $DR > 0$  in Fig. 3(b) (right axis, see also Fig. S17 in the supplementary material) with the highest and lowest values for the HI and the PbI<sub>2</sub> samples, respectively. Interestingly, the reference sample resulted in a DR value close to that of the PbI<sub>2</sub>-treated device. This latter behavior mismatches that of the previous MPP tracking experiments,<sup>72</sup> where the reference device was more unstable. However, in that study,<sup>72</sup> there were not intermittent short-circuit periods for current stabilization and IS measurements. Therefore, one can hypothesize that the short-circuit and near-flatbands hinder and favor the degradation of the untreated sample, respectively, and the opposite can be true for the PbI<sub>2</sub>-treated samples.

The IS spectra in short-circuit conditions were obtained along the above-described operational stability tests, and the results are depicted in Figs. 3(c)–3(e) (see also Sec. S4 in the supplementary material). Analogous to the previous discussion, two main trends were observed. For the reference and optimized samples, a relatively stable evolution of the IS spectra was found. Figure 3(c) zooms in on the Hf region in the impedance Nyquist plots for the reference sample, which shows a slight decrease in Hf resistance over time during the degradation test. This highlights the accuracy of the IS experiments, even though the main contribution to resistance and device performance comes from the larger I<sub>f</sub> range of the spectra. In Fig. 3(d) (see also Fig. S18 in the supplementary material), the complete Nyquist plots for the PbI<sub>2</sub>-treated sample illustrate the apparent constancy of the device over the time of the degradation test. At the same time, the spectra are also shown to be similarly unchanged in the impedance and capacitance Bode plots in Figs. S19 and S20 in the supplementary material, respectively. This steadiness of the reference and optimized samples in short-circuit

suggests the stability of the device's shunt resistance, which agrees with the slight increase in the output power shown in Fig. 3(a). Furthermore, it is implied that any significant improvement in device operation performance should be mostly related to the modification of optical absorption and/or the improvement of the transport properties, which affects the near-flatband regime.

The HI and MAI cells show an unstable behavior in the IS spectra over time under constant illumination, as shown in Figs. 3(e) and 3(f) (see also Figs. S18–S20 in the supplementary material). Not only is the absolute impedance smaller in these samples with respect to the reference and optimized ones, but also a clear increase is observed over time. The longer the operation time under constant illumination, the higher the impedance of the sample, which correlates with the performance improvement in Fig. 3(a). Interestingly, the three-similar-arcs feature in the Nyquist plot evolves into the more typical two-arcs shape where the Hf arc is significantly smaller than that of the I<sub>f</sub> range. Once more, the qualitative change of the I<sub>f</sub> part of the IS spectra suggests that the nature and/or quantity of the mobile ion properties may be modified by the action of the current flow under continuous illumination.

The instability of the MAI and HI samples indicates the presence of intrinsic reactivity, which could be understood in terms of the creation of a non-stoichiometric excess of MA, I, or H that modifies the local composition of the perovskite in contact with the NiO<sub>x</sub> interface. It may appear counter-intuitive that these excess reagents contribute to performance improvement rather than further degradation. However, one must bear in mind that intrinsic reactivity transforms the material composition and properties regardless of whether it contributes to or hinders the final device operational performance. Additionally, the chemical “softness” of the perovskite under biasing is highlighted here since only 0.2 sun (white LED equivalent) illumination intensity with room temperature (<40 °C) has been sufficient to catalyze the modification of the samples, when compared with previous studies<sup>72</sup> on unbiased samples comprising MAPbI<sub>3</sub> on treated NiO<sub>x</sub> films.

Evidence that the use of non-stoichiometric formulations using volatile precursors of PSCs modifies the operational stability of the PSC,<sup>76</sup> which creates an excess of mobile ions, already exists in the literature. For instance, Lammar *et al.*<sup>18</sup> found that the excess of a protic precursor, FAI, linked to a larger concentration of mobile ionic defects, also leads to an initial increase of the PCE under illumination due to ionic redistribution. HI and MAI are not only more acidic but also smaller than the rest of the studied additives and, consequently, more likely to infiltrate in the perovskite lattice and create ionic defects.<sup>72</sup>

## C. Drift-diffusion simulations

The experiments described in Secs. III A and III B illustrate the effects of different treatments applied to the surface of the NiO<sub>x</sub> HTL before the subsequent deposition of the absorber perovskite layer. Two main trends were identified. First, 1-iodobutane, 1-phenylethylamine, and PbI<sub>2</sub> treatments result in similar or even improved device performance and stability compared to the reference untreated samples. Second, samples treated with MAI and HI exhibited very low FF values in the J-V curves and anomalous

three-arcs low impedance IS spectra in the Nyquist plots. These samples also show operational instability under constant illumination over time.

These observations raise several questions on material evolution and its implications for transport. This section presents a series of numerical simulations that qualitatively reproduce experimental behaviors. Modeling then explores the correlation between the experiments and the fundamental material and transport properties. The simulation parameters and detailed descriptions of the simulated spectra can be found in Secs. S5 and S6 in the [supplementary material](#) for the simulations made with SETFOS Fluxim software<sup>28</sup> and MATLAB's *Driftfusion* code,<sup>73</sup> respectively. The use of two simulators not only provides further validation to these analyses but also allows for the assessment of the impact of

different boundary conditions on the same problems. SETFOS assumes recombination velocities at the interfaces, while *Driftfusion* utilizes nm-thick interface layers with local bulk recombination coefficients. The simulation results presented below will demonstrate the qualitative agreement between the two simulators, along with a reasonable quantitative agreement (within the same order of magnitude) for the resulting spectra and main simulation parameters.

The initial current–voltage curves under standard 1 sun illumination were qualitatively fitted to match the DC electrical response before the simulation of the IS spectra, as shown in Figs. 4(a) and 4(b). The simulations considered a range of mobile ion concentrations ( $N_{ion}$ ) between  $10^{15}$  and  $10^{19} \text{ cm}^{-3}$ , which includes the minimum defect concentration measurable with IS

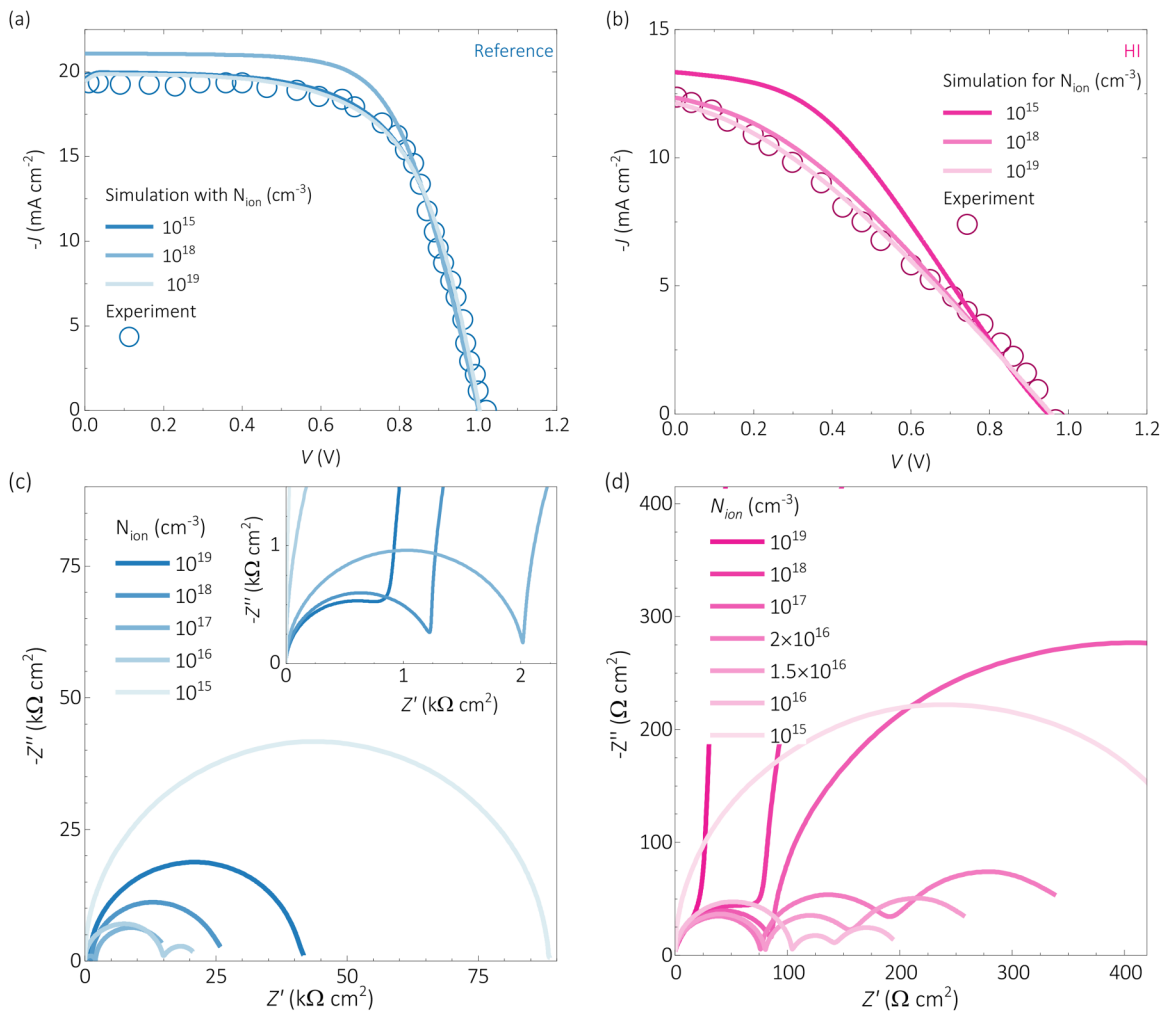


**FIG. 4.** Simulated [(a) and (b)] current–voltage under 1 sun illumination intensity and [(c) and (d)] impedance spectra in short-circuit under 0.2 sun illumination intensity for (a) and (c) the reference and (b) and (d) the HI devices considering different mobile ion concentrations, as indicated. The simulations were done with MATLAB's *Driftfusion*<sup>73</sup> code with details as described in Sec. S6 in the [supplementary material](#).

14 September 2024 06:40:10

methods and the effective density of states at the bands,<sup>77</sup> although limited depletion<sup>78</sup> was neglected. Notably, in order to reproduce the  $J - V$  response from the HI- and MAI-treated samples, three main parameters were modified with respect to those used to simulate the reference and optimized samples.

First, a change of absorptivity was considered by reducing the homogeneous charge carrier generation rate from  $G_{ref} = 3.3 \times 10^{21}$  to  $G_{HI} = 2.2 \times 10^{21} \text{ cm}^{-3}$ , mostly accounting for the  $J_{sc}$  difference between the reference and the HI samples, respectively. Note that this reduced generation rate is not necessarily linked to lower light harvesting but to a lower rate of formation of photogenerated carriers due to the modification of the morphology and crystalline properties, as shown in our simultaneous work.<sup>72</sup>

Second, an increase of series resistance from 2.5 up to  $25 \Omega \text{ cm}^2$  was taken for the HI sample that directly diminishes the FF from around 70%, for the reference and optimized cells, to less than 40% for the MAI and HI devices.

Third, the mobility of electron and hole charge carriers was reduced at the  $\text{NiO}_x$  HTL in HI sample simulations to a tenth of those used in the reference cell. The modification of this parameter can be correlated with the modification of the HTL during the surface treatment, resulting in a decrease in FF in the  $J - V$  characteristic. Moreover, the modification of the electron and hole mobilities in the perovskite layer has also been found to alter the shape of the  $J - V$  curve, accounting for some of the above-described reductions in  $J_{sc}$  and the FF.

The increase of  $N_{ion}$  decreases the  $J_{sc}$  and the FF of the simulated  $J - V$  curves in Figs. 4(a) and 4(b) (see also Fig. S45 in the supplementary material). This can be associated with electric field screening.<sup>23,40</sup> Below a threshold value, a higher  $N_{ion}$  leads to a smaller effective built-in field of the junction, which diminishes the drift current producing photocurrent around the short-circuit condition.<sup>18</sup> For instance, Fig. S24 in the supplementary material illustrates the field screening effect on the electrostatic potential for low and high concentrations of charge carriers. On the other hand, closer to the flatband condition, which for these samples approaches the open-circuit voltage ( $V_{oc}$ ), the effect of  $N_{ion}$  becomes smaller, resulting in very similar currents for the same bias. Around the flatband condition, the diffusion current becomes the main transport mechanism within the quasi-neutral region of the transport layers and gains importance in the perovskite, which is no longer as dependent on the electric field shielding effect of the mobile ions. Notably, the curves of Figs. 4(a) and 4(b) can be considered quasi-steady-state solutions since only a small hysteresis effect was obtained in the simulations.

The illumination intensity-dependent IS spectra simulated in short-circuit conditions are presented in Secs. S5.3 (Figs. S26 and S27) and S6.2 (Figs. S34–S36) in the supplementary material. Our model qualitatively reproduces the  $R_{Lf} \propto P_{in}^{-1}$  and  $C_{Lf} \propto P_{in}$  trends in the experiments of Fig. 2, where  $J_{sc}$  can be taken as a measure of the incident power density. Interestingly, the simulated total resistance  $R = (R_{Hf} + R_{Lf})$  decreases with the increment of illumination intensity,  $R \propto P_{in}^{-1}$ , regardless of the mobile ion concentration. Moreover, the appearance of the two-arc spectra including  $R_{Lf}$  and  $C_{Lf}$  is obtained as  $N_{ion}$  is increased.

Under constant 0.2 sun illumination intensity, the simulated IS spectra in short-circuit are presented in Figs. 4(c) and 4(d) for

the reference and HI/MAI samples, respectively. A common feature for both device types is that the impedance spectra do not behave smoothly with the increase of  $N_{ion}$ . The highest impedance arcs in Nyquist plot representation are obtained for the lowest and highest values of  $N_{ion}$ , whereas a minimum impedance is found for intermediate values. For  $N_{ion} < 10^{16} \text{ cm}^{-3}$ , the electric field screening is not sufficient to shield the built-in field, and the conduction is hindered. On the other hand, for  $N_{ion} > 10^{18} \text{ cm}^{-3}$ , the excess mobile ions may behave as a doping-like effect that redistribute independently of the built-in field, which favors diffusion transport in the perovskite.<sup>50,79</sup> In an intermediate range of  $10^{16} < N_{ion} < 10^{18} \text{ cm}^{-3}$ , the charge density profile of mobile ions is modified, resulting in a trade-off between drift and diffusion currents. This increase of diffusion current enhances the associated  $L_f$  capacitance, whose behavior opposes to some degree that of the resistance: minimum capacitance values are found for the lowest and the highest  $N_{ion}$  values.

Two mobile ion species were considered in this work to reproduce both the two- and the three-arcs Nyquist plot spectra. For the two-arc spectra, many reports in the literature typically use only one species of mobile ions, with the second species either neglected or kept constant and homogeneously distributed.<sup>45,47</sup> However, in our simulations under short-circuit conditions, the three-arcs spectra required the inclusion of two mobile ion species and a critical dependency between their mobilities and the concentration of charge carriers near the interfaces. For instance, Figs. S25 and S33 in the supplementary material illustrate the effect of modifying the ion concentration and mobility, which reproduces the two- or three-arc spectra in the Nyquist representation. Particularly, Fig. S25(d) in the supplementary material shows the three arcs for interface recombination velocities that are ten times higher for holes than for electrons. Additionally, the value of  $R_{sh}$  modified the relative proportions of resistance between the three arcs, aligning with the expected minimum experimental values of  $R_{sh}$  in the HI and MAI samples compared to the reference samples.

An empirical estimation of the mobile ion concentrations can be made from the IS spectra in terms of the characteristic resistance-frequency ratio,

$$\beta = \frac{R_{Lf}}{R_{Hf}}, \quad (2)$$

which expresses the balance between low-frequency-ion- and high-frequency-electron-related resistances. The values of  $\beta > 1$  ( $\beta < 1$ ) indicate a major contribution of ionic (electronic) phenomena. The direct dependency between  $\beta$  and  $N_{ion}$  is illustrated in Fig. 5: the higher the value of  $N_{ion}$  the higher that of  $\beta$ . For instance, in Fig. 5(a), horizontal lines indicate the experimental values from Figs. 3(c)–3(f) and dots are the simulated spectra in Fig. 4(c). Then, combining the quantitative and qualitative simulations of  $J-V$  curves and IS spectra in Fig. 4(a), respectively, our simulations suggest mobile ion concentrations in the range  $10^{17} < N_{ion} < 10^{18} \text{ cm}^{-3}$  for the reference sample. In the case of the HI or MAI samples, the stability test evolves from a situation where  $\beta \leq 1$  to another where  $\beta \approx 10$ , which suggests an increase from  $N_{ion} \approx 10^{16} \text{ cm}^{-3}$  to higher ion densities  $N_{ion} \approx 10^{17} \text{ cm}^{-3}$ . Notably,

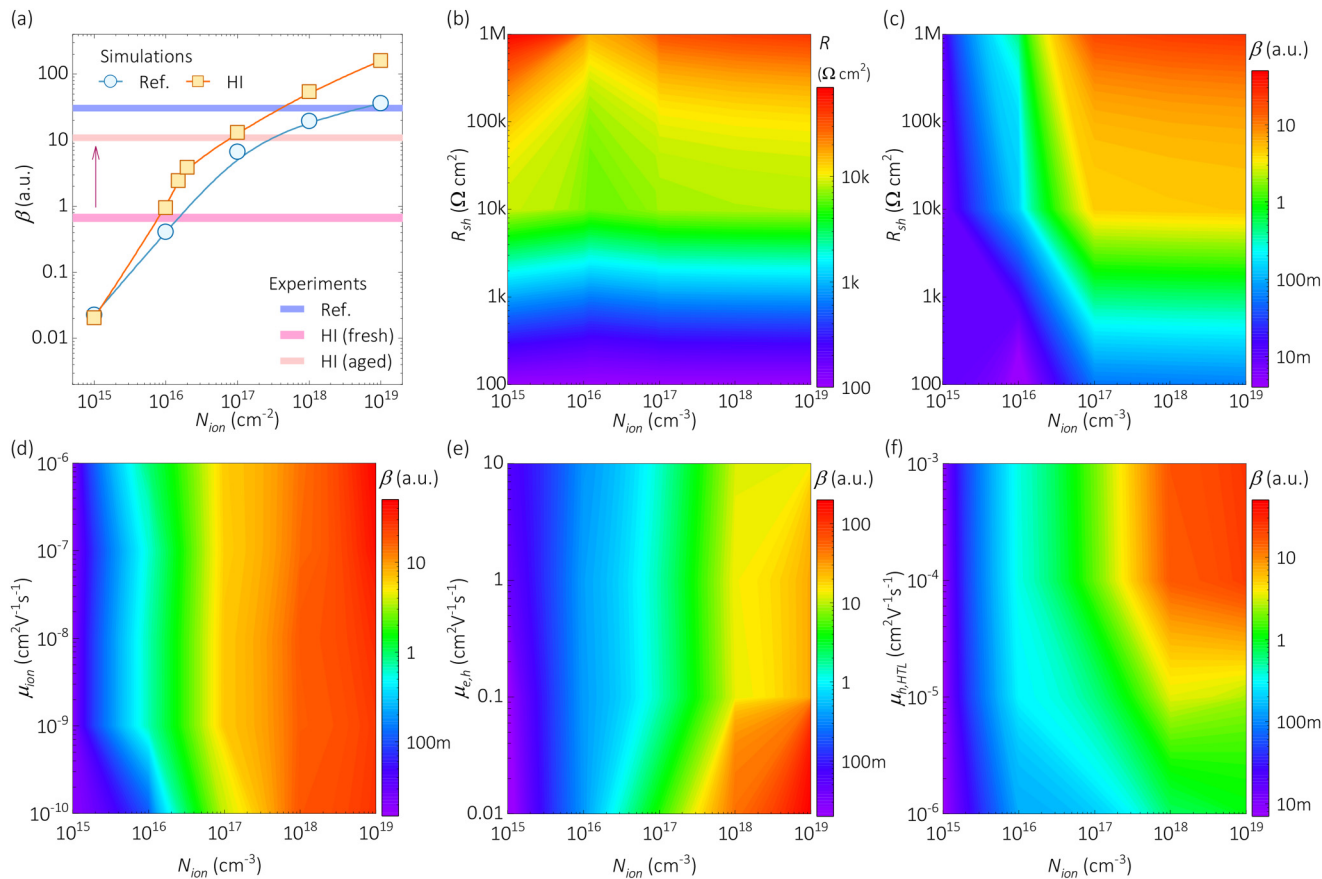


**FIG. 5.** Resistance–frequency ratio of Eq. (2) extracted from the simulated impedance spectra in short-circuit conditions under 0.2 sun illumination for different concentrations of mobile ions, shunt resistance [(b) and (c)], and mobility of (d) ions and (e) electrons and holes in the perovskite and (f) holes in the NiO<sub>x</sub> selective layer. The total resistance in (b) adds both low- and high-frequency resistances. The simulations were done with MATLAB's *Driftdiffusion*<sup>73</sup> code with details as described in Sec. S6 in the supplementary material.

14 September 2024 06:40:10

this correlation between instability and higher values of  $N_{ion}$  has also been recently reported in the literature.<sup>23</sup> However, the apparent increase of the mobile ion concentration over time, observed when comparing the performance of the as-fabricated sample with that at the end of the stability test may be affected by other parameters.

The effect of shunt resistance is analyzed in Secs S5.3 and S6.3 in the [supplementary material](#). The value of  $R_{sh}$  does not modify the capacitance of the sample in short circuit (Fig. S37 in the [supplementary material](#)). In contrast, the decrease of  $R_{sh}$  enforces a reduction on the total resistance of the sample, which is well known to reduce the FF in the  $J - V$  curve under illumination (see Figs. S4, S28, and S37 in the [supplementary material](#)). Moreover, an inconvenient side effect of the reduction of  $R_{sh}$  is the overlapping of a device's own junction or recombination resistance. This prevents the estimation of transport properties in short-circuit conditions. For instance, Fig. 5(b) displays total resistance as a function of both  $N_{ion}$  and  $R_{sh}$ . In that plot, low  $R_{sh}$  values produce the same

$R$  values, regardless of  $N_{ion}$ . It is only after the increase of  $R_{sh}$  that different  $R$  values appear as a function of  $N_{ion}$ . Concerning the HI sample in Fig. 5(a), the simulated relation between  $R_{sh}$ ,  $N_{ion}$ , and  $\beta$  is presented in Fig. 5(c). Our calculations suggest that the experimental change in  $\beta$  could be attained by increasing (i)  $\sim 10$  times  $N_{ion}$ , (ii)  $\sim 100$  times  $R_{sh}$ , or (iii) a combination of both effects [see arrows in Fig. 5(b)].

The effect of other simulation parameters on  $\beta$  was also investigated, although  $R_{sh}$  remained the one with the most direct impact. For instance, the influence of the recombination lifetime in the perovskite bulk ( $\tau_{bulk}$ ) and surface recombination lifetime at the HTL interface ( $\tau_s$ ) was explored, as presented in Secs. S5.4, S6.5, and S6.6 (Figs. S46–S49 in the [supplementary material](#)). In terms of  $\beta$ , no clear correlation with  $\tau_{bulk}$  or  $\tau_s$  is evident (see Figs. S46 and S48 in the [supplementary material](#)). Moreover, the increase of the dielectric constant of the perovskite absorber layer was also tested (see Fig. S55), but no significant change was found for  $\beta$  while a reduction of the total resistance was evident.

Importantly, the effect of different charge carrier mobilities is known to affect the impedance spectra,<sup>18</sup> which relate to our simulations presented in Secs. S5.5 and S6.7 in the [supplementary material](#). The increase of ion mobility ( $\mu_{ion}$ ) or electron/hole mobility ( $\mu_{e,h}$ ) in the perovskite resulted in small changes in  $\beta$  as shown in Figs. 5(e) and 5(f), respectively. In these contour plots, characteristic columnar patterns are formed due to the strong correlation between  $\beta$  and  $N_{ion}$  (in the abscissa axis), while  $\beta$  is nearly independent of  $\mu_{ion}$ . In contrast, a dependency of the  $\beta$  values in Fig. 5(e) is clear for the hole mobility in the HTL ( $\mu_{h,HTL}$ ) in the range  $N_{ion} > 10^{16} \text{ cm}^{-3}$ : the higher the  $\mu_{h,HTL}$ , the higher the  $\beta$ . Notably, despite the slighter correlation between  $\beta$  and the mobilities, the  $J - V$  curves and the low-frequency part of the IS spectra, specifically the capacitance, are very sensitive to the charge carrier mobilities (see Figs. S50–S54 in the [supplementary material](#)).<sup>80</sup> Interestingly, the change in  $\mu_{e,h}$  and  $\mu_{h,HTL}$  have a strong impact on the FF and the  $J_{sc}$  and no effect is evident for  $\mu_{ion}$  on the total resistance under short-circuit conditions.<sup>55</sup>

While the charge carrier recombination lifetime may be independent of  $\beta$ , the total resistance and capacitance are closely linked to the mobile ion concentration and the electrical response of the samples, as shown in Figs. S46–S49 in the [supplementary material](#). The value of  $\tau_{bulk}$  does not have a simple correlation with the total resistance and capacitance from the IS spectra in short-circuit conditions. Notably, an approximate trend can be identified: an increase in resistance correlates with a decrease in capacitance when modifying the value of  $\tau_{bulk}$ . Furthermore, the reduction of  $\tau_{bulk}$  strongly decreases  $V_{oc}$  and  $J_{sc}$  as well as the FF for low concentrations of mobile ions. However, given our focus on passivation methods at the interface with the HTL, we center the analysis on the interface recombination, which can be approached differently depending on the model. For instance, the SETFOS software by Fluxim (see Fig. S29 in the [supplementary material](#)) utilizes the recombination velocity at the interface between the  $\text{NiO}_x$  HTL and the perovskite. Using this model, we demonstrate a decrease in the impedance as the recombination velocity increases, particularly noting a more pronounced alteration in the  $L_f$  region of the spectrum. Since a large contribution to current throughout the device in the short-circuit condition is due to recombination, the faster the surface recombination velocity ( $v_s$ ), the higher the leakage current and the smaller the resistance. Alternatively, MATLAB's code *Driffusion*<sup>73</sup> simulates the interfaces with narrow interlayers where the surface recombination lifetime  $\tau_s$  is set. Our simulations with this approach suggest an analogous reduction of impedance with the decrease in  $\tau_s$ , but a clear dependency on  $R_{sh}$  and  $N_{ion}$  is also identified.

Higher values of surface recombination increase the impedance in terms of its real part, as shown in the Bode plot of Fig. 6(a), where  $\tau_s$  values of  $10^{-6}$  and  $10^{-10} \text{ s}$  are compared over a range of ion densities. While this intuitive trend is clear for the lowest ( $10^{15} \text{ cm}^{-3}$ ) and the highest ( $10^{19} \text{ cm}^{-3}$ )  $N_{ion}$  values in Fig. 6(a), it is not as evident for intermediate ion densities between  $10^{16}$  and  $10^{17} \text{ cm}^{-3}$ . Therefore, the contour plot of Fig. 6(b) is introduced in terms of the total resistance. Two main features arise in this plot. First, the resistance can be nearly independent of the surface recombination across wide ranges of  $\tau_s$  and for specific intervals of  $N_{ion}$  [see vertical arrow in Fig. 6(b)]. Second, regardless of the  $\tau_s$

value, the total resistance depends on  $N_{ion}$  with characteristic minima between  $10^{16}$  and  $10^{17} \text{ cm}^{-3}$  [see horizontal arrow in Fig. 6(b)]. This is further highlighted in Fig. 6(c), where opaque to lighter red lines qualitatively indicate different values of  $\tau_s$  and  $\mu_{ion}$ .

The capacitance shows an even stronger but inverted dependency on the surface recombination in the Bode plots of Fig. 6(d), compared to that of the resistance. The corresponding total capacitance contour plot is presented in Fig. 6(e), revealing similar but opposite key features. First, the capacitance is nearly independent of the surface recombination across wider ranges of  $\tau_s$  and for certain intervals of  $N_{ion}$  [see vertical arrow in Fig. 6(e)]. Second, regardless of the  $\tau_s$  value, the total capacitance depends on  $N_{ion}$  with characteristic maxima between  $10^{16}$  and  $10^{17} \text{ cm}^{-3}$  [see horizontal arrow in Fig. 6(e)]. This is highlighted in Fig. 6(f), where opaque to lighter blue lines qualitatively indicate different values of  $\tau_s$  and  $\mu_{ion}$ . Notably, the total capacitance is mostly composed by the low-frequency contribution, which can be orders of magnitude higher than that of the geometrical capacitance. This discards trap capture emission processes as their main contribution.<sup>81</sup> The apparent inverse proportionality of the capacitance and the resistance under short-circuit conditions may suggest a typical chemical/diffusion capacitance-like origin,<sup>43</sup> where one can approximate  $C \propto J$  and  $J \propto R^{-1}$ , leading to  $C \propto R^{-1}$ . However, when  $N_{ion}$  changes, the capacitance increases (or decreases) by a factor of nearly a hundred while the resistance decreases (or increases) by a factor of around two. Therefore, a more accurate description would be  $C \propto R^{-p}$ , with  $p > 1$ . This highlights the complex relationship between capacitance, resistance, and the concentration of mobile ions, which cannot be easily understood using traditional capacitive definitions.

The minimum (maximum) of the resistance (capacitance) for the threshold ion concentrations between  $10^{15}$  and  $10^{17} \text{ cm}^{-3}$  suggest a transition between two main transport mechanisms in the perovskite bulk. For low mobile ion concentrations, the drift is expected as the main contribution. This continues to be true as long as the built-in electric field is fully screened. Then, for sufficiently high densities of mobile ions and under short-circuit conditions, the ionic total charge in the perovskite can even exceed that of the ionized donor/acceptor doping at selective layers. In these conditions, the mobile ions would be expected to diffuse and reorder homogeneously throughout the perovskite bulk.

To show the change in the transport regime, we plot energy diagrams, charge density, electrostatic potential, and electric field profiles in Fig. 7, where different concentrations are compared for low, threshold, and high mobile ion densities. The short-circuit regime energy diagrams in the top row of that figure reveal a transition from a typical drift transport situation for  $N_{ion} = 10^{15} \text{ cm}^{-3}$ , to flatband-like diagrams for  $N_{ion} = 5 \times 10^{16}$  and  $N_{ion} = 10^{19} \text{ cm}^{-3}$ . However, it is in the corresponding charge density profiles (middle row in Fig. 7) that the radical change in the distribution of mobile ions is revealed. For low  $N_{ion} = 10^{15} \text{ cm}^{-3}$ , the ions accumulate toward the interfaces in a nearly perfect exponential decay. In contrast, for  $N_{ion} = 5 \times 10^{16} \text{ cm}^{-3}$ , the ions distribute in much wider space charge regions, and for  $N_{ion} = 10^{19} \text{ cm}^{-3}$ , homogeneous coverage of the perovskite layer is obtained. This indicates that the mobile ions reorder in a homogeneous doping-like distribution, which fully screens the electric field and creates quasi-neutral

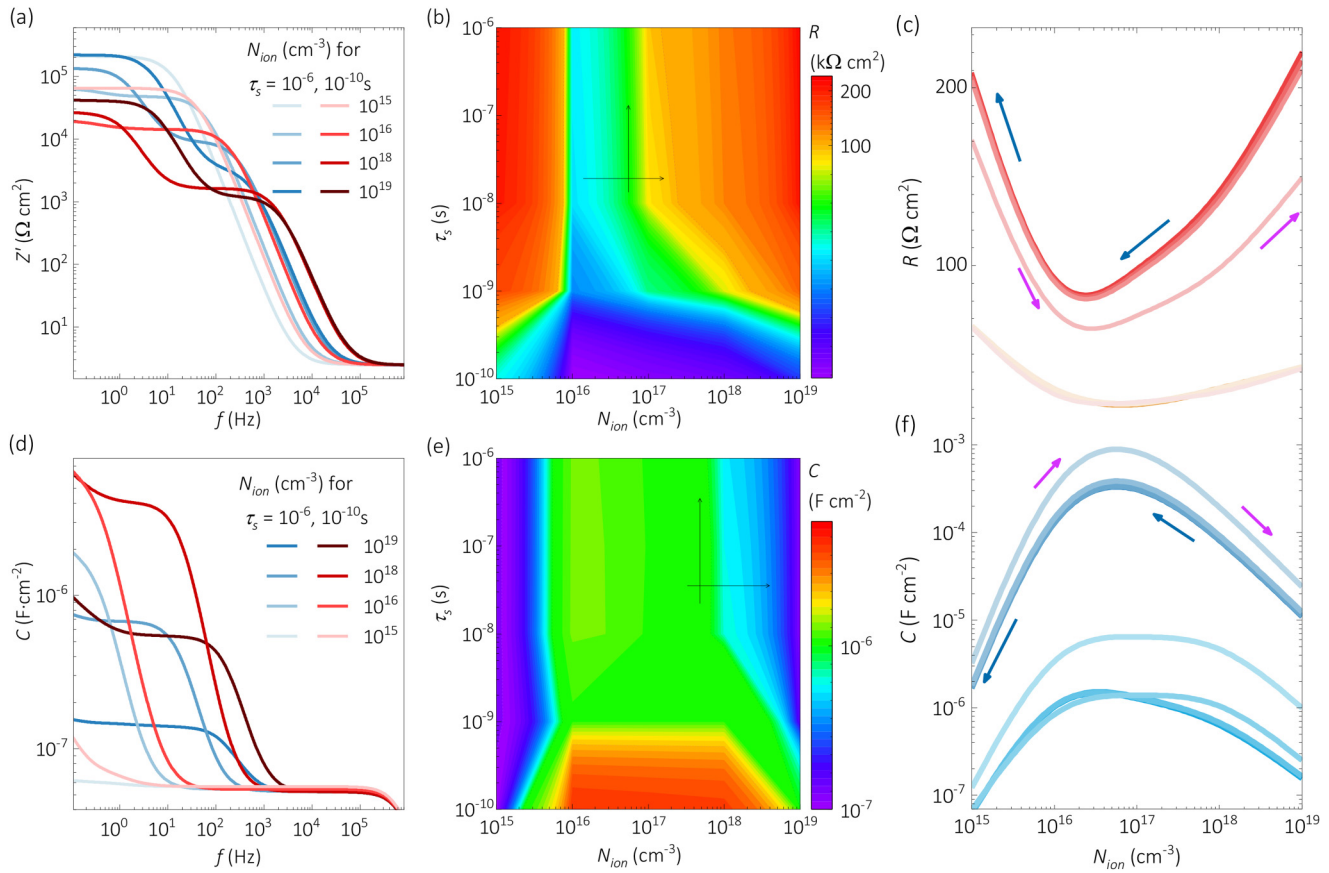


**FIG. 6.** Simulated impedance spectra in short-circuit conditions for different concentrations of mobile ions and surface recombination lifetimes at the HTL interface considering  $P_{in} = 0.2$  sun and  $R_{sh} = 1\text{ M}\Omega$ , as indicated. The representations include (a) the real part of impedance Bode plot, the total resistance (b) contour plot, and (c) 2D-plot, (d) the capacitance Bode plot, the total capacitance (e) contour plot, and (f) 2D-plot. In (c) and (f) different intensities in red and blue lines for the total resistance and capacitance, respectively, indicate different evaluations of  $\tau_s$  and  $\mu_{ion}$  values in a qualitative demonstration including degradation paths with  $N_{ion}$  increase (purple open arrows) and decrease (blue filled arrows). Simulations were done with MATLAB's *Driftfusion*<sup>73</sup> code with details as described in Sec. S6 in the supplementary material.

14 September 2024 06:40:10

regions within the perovskite. Interestingly, the increase in mobile ion density not only redistributes the ions but also the electronic charge carriers that show a sort of inversion in their location. For instance, the concentration of holes toward the HTL is reduced in favor of that near the ETL. This is a clear change that hinders the transport in the interface, which increases the resistance.

The electrostatic potential is also presented (left axis) along with the corresponding electric field (right axis) in the bottom row of Fig. 7. There, comparing the cases of  $N_{ion} = 10^{15}$  and  $N_{ion} = 5 \times 10^{16}$  cm $^{-3}$ , an apparent linear reduction occurs in the electrostatic potential drop and the effective electric field in the perovskite bulk. However, beyond the threshold value of mobile ion concentration (e.g.,  $N_{ion} = 10^{19}$  cm $^{-3}$ , right column of Fig. 7), the reduction in both the electrostatic potential drop and the effective electric field in the perovskite bulk is exponentially higher. Therefore, in the absence of an electric field, it is the diffusion transport that makes the main contribution to transport in the perovskite bulk.

Altogether, the simulations not only qualitatively reproduced the experimental results from the  $J$ - $V$  curves and the IS spectra in short-circuit conditions, but also suggested relevant correlations that contribute to a better understanding of the transport phenomena. In particular, the effect of the mobile ion concentration in the perovskite was analyzed and it was shown to strongly affect the total resistance, capacitance, and frequency ratio  $\beta$ . The value of  $\beta$  was suggested as an empirical estimation parameter for assessing  $N_{ion}$ . Interestingly, the resistance and capacitance trends complement each other with respect to  $N_{ion}$ ; they reach minimum and maximum, respectively, around a critical ion density (where  $\beta \approx 1$ ). This behavior corresponds to a threshold range of concentration of mobile ions that signifies the transition from drift- to diffusion-dominated transport in the bulk of the perovskite layer under short-circuit conditions. Interestingly, under short-circuit conditions, the diffusion-dominated regime at high concentrations of mobile ions closely resembles the near-flatband condition in terms

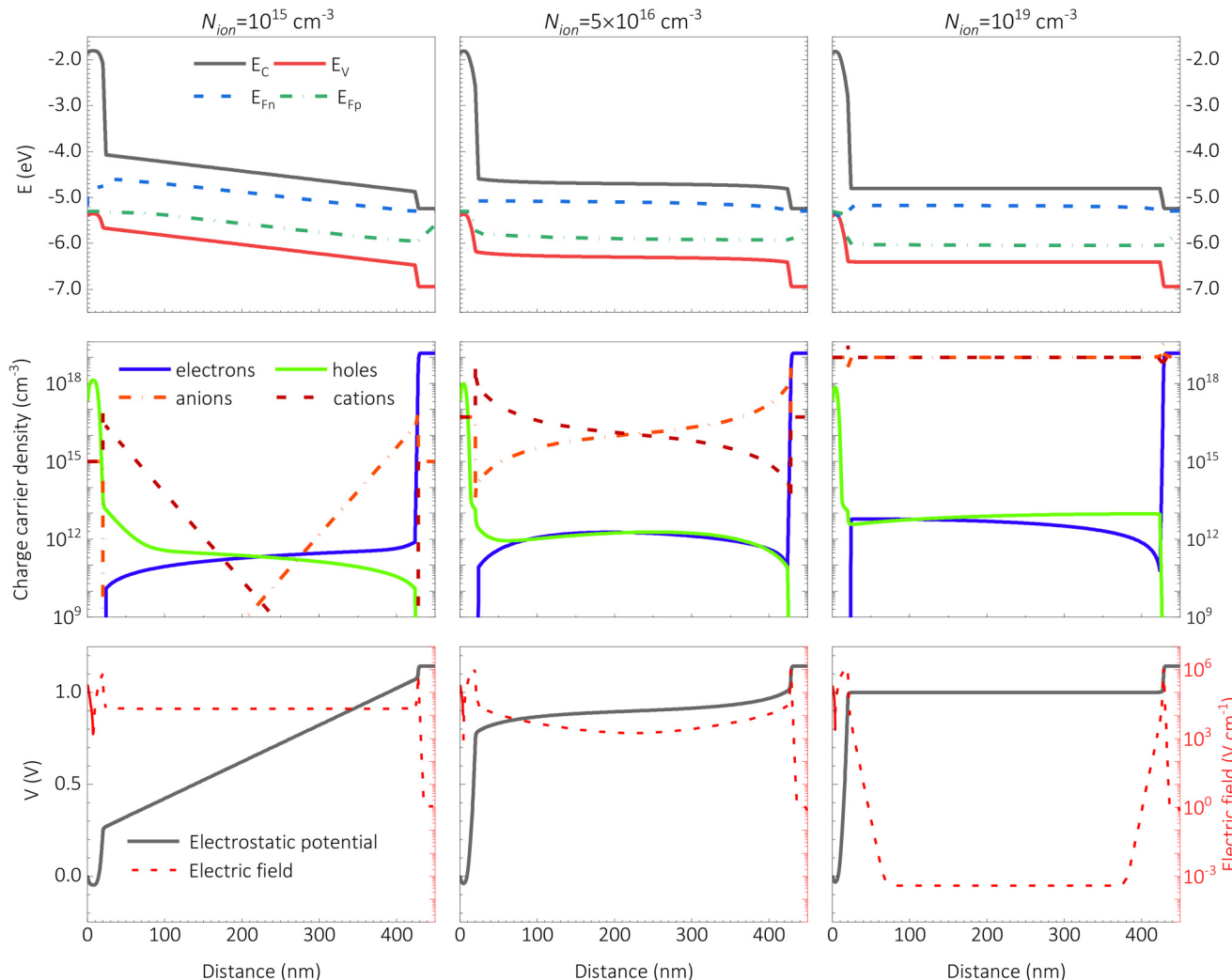


**FIG. 7.** Simulated energy diagrams (top row), charge densities (middle row), electrostatic potential (bottom row, left axis), and electric field (bottom row, right axis) profiles for ion density values of  $10^{15} \text{ cm}^{-3}$  (left column),  $5 \times 10^{16} \text{ cm}^{-3}$  (middle column), and  $10^{19} \text{ cm}^{-3}$  (right column) under short-circuit conditions. The simulations were done with MATLAB's *Driftfusion*<sup>73</sup> code with details as described in Sec. S6 in the [supplementary material](#).

of transport mechanisms and potential and field distributions. However, short-circuit and near-flatband regimes would still differ in terms of charge carrier concentrations, hence affecting the recombination processes.

#### IV. CONCLUSIONS

This work summarizes an optoelectronic characterization of perovskite solar cells with different passivation treatments on the interface between the perovskite absorber material and the  $\text{NiO}_x$  hole transport layer. From the initial assessment of device performance and the subsequent operational stability test, two main trends were identified. The untreated reference sample and those

utilizing 1-iodobutane, 1-phenylethylamine, and  $\text{PbI}_2$  as passivators resulted in relatively optimal and rather stable performances. In contrast, the MAI- and HI-treated samples not only exhibited a low fill factor and photocurrent, but also showed substantial instability with an apparent improvement of the output power up to three times the initial value during the operational stability test.

The use of IS analysis under short-circuit conditions, with varying illumination intensities and over time during operational stability tests, has been introduced, discussed, and carried out as a resourceful procedure for understanding the electrical response of solar cells. Several practical and theoretical advantages of this approach have been highlighted compared to the more common open-circuit/flatband and/or MPP studies. The experimental

spectra showed that the untreated and optimized devices behave typically: two main  $RC$  constants produce two arcs in the impedance Nyquist representation. By using equivalent circuit modeling, resistances for the low- and high-frequency ranges of spectra can be identified, and the resistance frequency ratio entails  $\beta \gg 1$  for  $R_{Lf} \gg R_{Hf}$ . Characteristically, the MAI- and HI-treated samples evidenced up to three  $RC$  constants with an extra middle-frequency feature that apparently merged with the low-frequency part of the spectra under reduced illumination intensity or prolonged exposure to light during the operational stability test. Notably, the bias-stress degradation test, consisting of continuous switching between the operational forward bias close to the MPP and the short-circuit condition, was found to break the cells, suggesting its potential use as a reliability test protocol in future works.

Our drift-diffusion simulations qualitatively reproduced most of the experimental behaviors observed in the  $J$ - $V$  and IS measurements. Despite several assumptions in modeling and the acknowledged numerical overparameterization, our simulations correlate the HI and MAI treatments on the  $\text{NiO}_x$  HTL with reductions in (i) the concentration of mobile ions, (ii) shunt resistance, (iii) mobility at the HTL, and (iv) the photogeneration rate, compared to the respective values for the non-passivated reference sample. Moreover, the characteristic three-arc spectra resulting from the passivation and evolving during the stability test indicate the presence of two species of mobile ions with significantly different mobilities. These simulation results can be used to further comprehend the working mechanism of PSCs. In particular, we propose using  $\beta$  as an empirical method for assessing the ionic properties and the chemical nature of their interfaces.

Notably, the simulated total resistance and capacitance under short-circuit conditions exhibit a characteristic behavior with respect to the concentration of mobile ions: resistance reaches a minimum while capacitance a maximum around a threshold ion density. Below this threshold, drift-dominated transport takes place in the perovskite bulk. In contrast, beyond the built-in field screening ion concentration onset, diffusion-dominated transport makes the main contribution to current in the perovskite bulk.

## SUPPLEMENTARY MATERIAL

See the [supplementary material](#) for introductory schemes on degradation mechanism, the literature summary on the dependency of short-circuit resistance; detailed description of sample fabrication methods; detailed description and data of the measurement methods and results for the stability tests and IS measurement and analyses; detailed summary on simulation parameters, simulated  $J$ - $V$  curves, and IS spectra.

## ACKNOWLEDGMENTS

J.A.A. acknowledges the Ministerio de Ciencia e Innovación of Spain, Agencia Estatal de Investigación (AEI) and EU (FEDER) under Grant Nos. TED2021-129758B-C33 (TransEL), PID2022-140061OB-I00 (DEEPMATSOLAR), and PCI2019-111839-2 (SCALEUP). O.A. acknowledges the Juan de la Cierva Fellowship Grant No. FJC2021-046887-I funded by MICIU/AEI/ 10.13039/501100011033 and by the European Union NextGenerationEU/PRTR. P.L.-V. thanks the French Government

in the frame of the program of investment for the future (Programme d'Investissement d'Avenir, No. ANR-IEED-002-01). J.M. and S.O. thank the Ministry of Economic Affairs Innovation, Digitalization and Energy of the State of North Rhine-Westphalia for funding under Grant SCALEUP (SOLAR-ERA.NET Cofund 2, id: 32).

## AUTHOR DECLARATIONS

### Conflict of Interest

The authors declare no conflicts to disclose.

### Author Contributions

**Osbel Almora:** Conceptualization (lead); Data curation (equal); Formal analysis (equal); Investigation (lead); Methodology (lead); Project administration (equal); Software (equal); Validation (equal); Visualization (equal); Writing – original draft (lead); Writing – review & editing (lead). **Pilar López-Varo:** Conceptualization (equal); Data curation (equal); Formal analysis (equal); Investigation (equal); Methodology (equal); Software (lead); Validation (equal); Visualization (equal); Writing – review & editing (supporting). **Renán Escalante:** Data curation (supporting); Investigation (supporting); Software (supporting); Validation (supporting); Visualization (supporting); Writing – review & editing (supporting). **John Mohanraj:** Data curation (supporting); Investigation (supporting); Resources (supporting); Validation (supporting); Writing – review & editing (supporting). **Lluis F. Marsal:** Funding acquisition (supporting); Project administration (supporting); Resources (supporting); Supervision (supporting); Writing – review & editing (supporting). **Selina Olthof:** Formal analysis (supporting); Funding acquisition (supporting); Investigation (supporting); Project administration (supporting); Resources (supporting); Supervision (supporting); Visualization (supporting); Writing – review & editing (supporting). **Juan A. Anta:** Conceptualization (supporting); Data curation (supporting); Formal analysis (supporting); Funding acquisition (lead); Investigation (supporting); Methodology (supporting); Project administration (lead); Resources (lead); Software (equal); Supervision (lead); Validation (supporting); Visualization (supporting); Writing – review & editing (supporting).

## DATA AVAILABILITY

The data that support the findings of this study are available from the corresponding authors upon reasonable request.

## REFERENCES

- <sup>1</sup>O. Almora, C. I. Cabrera, S. Erten-Ela, K. Forberich, K. Fukuda, F. Guo, J. Hauch, A. W. Y. Ho-Baillie, T. J. Jacobsson, R. A. J. Janssen, T. Kirchartz, M. A. Loi, X. Mathew, D. B. Mitzi, M. K. Nazeeruddin, U. W. Paetzold, B. P. Rand, U. Rau, T. Someya, E. Unger, L. Vaillant-Roca, and C. J. Brabec, "Device performance of emerging photovoltaic materials (version 4)," *Adv. Energy Mater.* **14**, 2303173 (2024).
- <sup>2</sup>G. Pacchioni, "Highly efficient perovskite LEDs," *Nat. Rev. Mater.* **6**, 108 (2021).
- <sup>3</sup>J. Moon, Y. Mehta, K. Gundogdu, F. So, and Q. Gu, "Metal-Halide perovskite lasers: Cavity formation and emission characteristics," *Adv. Mater.* **36**, 2211284 (2024).

- <sup>4</sup>A. O. Álvarez, F. Lédée, M. García-Batle, P. López-Varo, E. Gros-Daillon, J. Mayén Guillén, J.-M. Verilhac, T. Lemercier, J. Zaccaro, L. F. Marsal, G. García-Belmonte, and O. Almora, "Ionic field screening in MAPbBr<sub>3</sub> crystals from remnant sensitivity in X-ray detection," *ACS Phys. Chem. Au* **3**, 386 (2023).
- <sup>5</sup>J. Zhou, Y. Gao, Y. Pan, F. Ren, R. Chen, X. Meng, D. Sun, J. He, Z. Liu, and W. Chen, "Recent advances in the combined elevated temperature, humidity, and light stability of perovskite solar cells," *Sol. RRL* **6**, 2200772 (2022).
- <sup>6</sup>S. Ghosh, S. Mishra, and T. Singh, "Antisolvents in perovskite solar cells: Importance, issues, and alternatives," *Adv. Mater. Interfaces* **7**, 2000950 (2020).
- <sup>7</sup>A. Belous, S. Kobylanska, O. V'yunov, P. Torchyniuk, V. Yukhymchuk, and O. Hreshchuk, "Effect of non-stoichiometry of initial reagents on morphological and structural properties of perovskites CH<sub>3</sub>NH<sub>3</sub>PbI<sub>3</sub>," *Nanoscale Res. Lett.* **14**, 4 (2019).
- <sup>8</sup>Y. Gao, F. Ren, D. Sun, S. Li, G. Zheng, J. Wang, H. Raza, R. Chen, H. Wang, S. Liu, P. Yu, X. Meng, J. He, J. Zhou, X. Hu, Z. Zhang, L. Qiu, W. Chen, and Z. Liu, "Elimination of unstable residual lead iodide near the buried interface for the stability improvement of perovskite solar cells," *Energy Environ. Sci.* **16**, 2295 (2023).
- <sup>9</sup>K. Pinsuwan, C. Boonthum, T. Supasai, S. Sahasithiwat, P. Kumnorkaew, and P. Kanjanaboons, "Solar perovskite thin films with enhanced mechanical, thermal, UV, and moisture stability via vacuum-assisted deposition," *J. Mater. Sci.* **55**, 3484 (2020).
- <sup>10</sup>F. Valipour, E. Yazdi, N. Torabi, B. F. Mirjalili, and A. Behjat, "Improvement of the stability of perovskite solar cells in terms of humidity/heat via compositional engineering," *J. Phys. D: Appl. Phys.* **53**, 285501 (2020).
- <sup>11</sup>D. Lan and M. A. Green, "Combatting temperature and reverse-bias challenges facing perovskite solar cells," *Joule* **6**, 1782 (2022).
- <sup>12</sup>K. M. Anoop, M. V. Khenkin, F. Di Giacomo, Y. Galagan, S. Rahmany, L. Etgar, E. A. Katz, and I. Visoly-Fisher, "Bias-dependent stability of perovskite solar cells studied using natural and concentrated sunlight," *Sol. RRL* **4**, 1900335 (2020).
- <sup>13</sup>M. V. Khenkin, K. M. Anoop, E. A. Katz, and I. Visoly-Fisher, "Bias-dependent degradation of various solar cells: Lessons for stability of perovskite photovoltaics," *Energy Environ. Sci.* **12**, 550 (2019).
- <sup>14</sup>K. Brelc, M. Jošt, M. Bokalič, J. Ekar, J. Kovač, and M. Topič, "Are perovskite solar cell potential-induced degradation proof?," *Sol. RRL* **6**, 2100815 (2022).
- <sup>15</sup>M. I. El-Henawy, I. M. Hossain, L. Zhang, B. Bagheri, R. Kottokkaran, and V. L. Dalal, "Influence of grain size on the photo-stability of perovskite solar cells," *J. Mater. Sci.: Mater. Electron.* **32**, 4067 (2021).
- <sup>16</sup>A. Julien, J.-B. Puel, and J.-F. Guillemoles, "Distinction of mechanisms causing experimental degradation of perovskite solar cells by simulating associated pathways," *Energy Environ. Sci.* **16**, 190 (2023).
- <sup>17</sup>H. J. Jung, D. Kim, S. Kim, J. Park, V. P. Dravid, and B. Shin, "Stability of halide perovskite solar cell devices: *In situ* observation of oxygen diffusion under biasing," *Adv. Mater.* **30**, 1802769 (2018).
- <sup>18</sup>S. Lammar, R. Escalante, A. J. Riquelme, S. Jenatsch, B. Ruhstaller, G. Oskam, T. Aernouts, and J. A. Anta, "Impact of non-stoichiometry on ion migration and photovoltaic performance of formamidinium-based perovskite solar cells," *J. Mater. Chem. A* **10**, 18782 (2022).
- <sup>19</sup>Y. Huang, P. Lopez-Varo, B. Geffroy, H. Lee, J.-E. Bourée, A. Mishra, P. Baranek, A. Rolland, L. Pedesseau, J.-M. Jancu, J. Even, J.-B. Puel, and M. Gueunier-Farret, "Detrimental effects of ion migration in the perovskite and hole transport layers on the efficiency of inverted perovskite solar cells," *J. Photonics Energy* **10**, 024502 (2020).
- <sup>20</sup>X. Yan, W. Fan, F. Cheng, H. Sun, C. Xu, L. Wang, Z. Kang, and Y. Zhang, "Ion migration in hybrid perovskites: Classification, identification, and manipulation," *Nano Today* **44**, 101503 (2022).
- <sup>21</sup>C. Eames, J. M. Frost, P. R. F. Barnes, B. C. O'Regan, A. Walsh, and M. S. Islam, "Ionic transport in hybrid lead iodide perovskite solar cells," *Nat. Commun.* **6**, 7497 (2015).
- <sup>22</sup>K. Sakhatskyi, R. A. John, A. Guerrero, S. Tsarev, S. Sabisch, T. Das, G. J. Matt, S. Yakunin, I. Cherniukh, M. Kotyryba, Y. Berezovska, M. I. Bodnarchuk, S. Chakraborty, J. Bisquert, and M. V. Kovalenko, "Assessing the drawbacks and benefits of ion migration in lead halide perovskites," *ACS Energy Lett.* **7**, 3401 (2022).
- <sup>23</sup>J. Thiesbrummel, S. Shah, E. Gutierrez-Partida, F. Zu, F. Peña-Camargo, S. Zeiske, J. Diekmann, F. Ye, K. P. Peters, K. O. Brinkmann, P. Caprioglio, A. Dasgupta, S. Seo, F. A. Adeleye, J. Warby, Q. Jeangros, F. Lang, S. Zhang, S. Albrecht, T. Riedl, A. Armin, D. Neher, N. Koch, Y. Wu, V. M. Le Corre, H. Snaith, and M. Stolterfoht, "Ion-induced field screening as a dominant factor in perovskite solar cell operational stability," *Nat. Energy* **9**, 664 (2024).
- <sup>24</sup>Q. Jiang, J. Tong, Y. Xian, R. A. Kerner, S. P. Dunfield, C. Xiao, R. A. Scheidt, D. Kuciauskas, X. Wang, M. P. Hautzinger, R. Tirawat, M. C. Beard, D. P. Fenning, J. J. Berry, B. W. Larson, Y. Yan, and K. Zhu, "Surface reaction for efficient and stable inverted perovskite solar cells," *Nature* **611**, 278 (2022).
- <sup>25</sup>S. Liu, V. P. Biju, Y. Qi, W. Chen, and Z. Liu, "Recent progress in the development of high-efficiency inverted perovskite sola7r cells," *NPG Asia Mater.* **15**, 27 (2023).
- <sup>26</sup>X. Lin, D. Cui, X. Luo, C. Zhang, Q. Han, Y. Wang, and L. Han, "Efficiency progress of inverted perovskite solar cells," *Energy Environ. Sci.* **13**, 3823 (2020).
- <sup>27</sup>B. Li and W. Zhang, "Improving the stability of inverted perovskite solar cells towards commercialization," *Commun. Mater.* **3**, 65 (2022).
- <sup>28</sup>SETFOS: Simulation Software for Organic and Perovskite Solar Cells and LEDs (FLUXIM, 2023). See <https://www.fluxim.com/setfos-intro> (accessed 28 March 2024).
- <sup>29</sup>A. A. Said, J. Xie, and Q. Zhang, "Recent progress in organic electron transport materials in inverted perovskite solar cells," *Small* **15**, 1900854 (2019).
- <sup>30</sup>X. Pu, J. Zhao, Y. Li, Y. Zhang, H.-L. Loi, T. Wang, H. Chen, X. He, J. Yang, X. Ma, X. Li, and Q. Cao, "Stable NiO<sub>x</sub>-based inverted perovskite solar cells achieved by passivation of multifunctional star polymer," *Nano Energy* **112**, 108506 (2023).
- <sup>31</sup>H. Wang, W. Zhang, B. Wang, Z. Yan, C. Chen, Y. Hua, T. Wu, L. Wang, H. Xu, and M. Cheng, "Modulating buried interface with multi-fluorine containing organic molecule toward efficient NiO<sub>x</sub>-based inverted perovskite solar cell," *Nano Energy* **111**, 108363 (2023).
- <sup>32</sup>X. Cai, T. Hu, H. Hou, P. Zhu, R. Liu, J. Peng, W. Luo, and H. Yu, "A review for nickel oxide hole transport layer and its application in halide perovskite solar cells," *Mater. Today Sustainability* **23**, 100438 (2023).
- <sup>33</sup>H. Wang, Z. Qin, X. Li, C. Zhao, and C. Liang, "High-performance inverted perovskite solar cells with sol-gel-processed silver-doped NiO<sub>x</sub> hole transporting layer," *Energy Environ. Mater.* **7**, e12666 (2024).
- <sup>34</sup>X. Yin, L. Song, P. Du, B. Xu, and J. Xiong, "Cation exchange strategy to construct nanopatterned Zn:NiO<sub>x</sub> electrode with highly conductive interface for efficient inverted perovskite solar cells," *Chem. Eng. J.* **457**, 141358 (2023).
- <sup>35</sup>T. Hu, H. Hou, J. Peng, Q. Wu, J. He, H. Yu, R. Liu, T. Hou, X. Zhou, M. Zhang, X. Zhang, X. Yang, Y. Sun, X. Li, and Y. Bai, "4-tert-butylpyridine induced Ni<sup>3+</sup>/Ni<sup>2+</sup> ratio modulation in NiO<sub>x</sub> hole transport layer towards efficient and stable inverted perovskite solar cells," *Mater. Today Energy* **32**, 101245 (2023).
- <sup>36</sup>X. Kang, D. Wang, K. Sun, X. Dong, H. Wei, B. Wang, L. Gu, M. Li, Y. Bao, J. Zhang, R. Guo, Z. Li, X. Jiang, P. Müller-Buschbaum, and L. Song, "Unraveling the modification effect at NiO<sub>x</sub>/perovskite interfaces for efficient and stable inverted perovskite solar cells," *J. Mater. Chem. A* **11**, 22982 (2023).
- <sup>37</sup>G. Shen, H. Dong, F. Yang, X. Ren Ng, X. Li, F. Lin, and C. Mu, "Application of an amphiphatic molecule at the NiO<sub>x</sub>/perovskite interface for improving the efficiency and long-term stability of the inverted perovskite solar cells," *J. Energy Chem.* **78**, 454 (2023).
- <sup>38</sup>O. Almora, L. G. Gerling, C. Voz, R. Alcubilla, J. Puigdollers, and G. García-Belmonte, "Superior performance of V<sub>2</sub>O<sub>5</sub> as hole selective contact over other transition metal oxides in silicon heterojunction solar cells," *Sol. Energy Mater. Sol. Cells* **168**, 221 (2017).
- <sup>39</sup>N. Ahn and M. Choi, "Towards long-term stable perovskite solar cells: Degradation mechanisms and stabilization techniques," *Adv. Sci.* **11**, 2306110 (2024).
- <sup>40</sup>C. Baretzky, C. Maheu, M. Frericks, T. Mayer, and U. Würfel, "Unraveling the energetic landscape of perovskite solar cells: A synergy of 2D drift-diffusion simulations and tapered cross-section photoelectron spectroscopy," *Sol. RRL* **7**, 2300355 (2023).

- <sup>41</sup>O. Almora, D. Miravet, I. Gelmetti, and G. Garcia-Belmonte, "Long-term field screening by mobile ions in thick metal halide perovskites: Understanding saturation currents," *Phys. Status Solidi RRL* **16**, 202200336 (2022).
- <sup>42</sup>I. Zarazua, G. Han, P. P. Boix, S. Mhaisalkar, F. Fabregat-Santiago, I. Mora-Seró, J. Bisquert, and G. Garcia-Belmonte, "Surface recombination and collection efficiency in perovskite solar cells from impedance analysis," *J. Phys. Chem. Lett.* **7**, 5105 (2016).
- <sup>43</sup>O. Almora and G. Garcia-Belmonte, "Light capacitances in silicon and perovskite solar cells," *Sol. Energy* **189**, 103 (2019).
- <sup>44</sup>W. Clarke, M. V. Cowley, M. J. Wolf, P. Cameron, A. Walker, and G. Richardson, "Inverted hysteresis as a diagnostic tool for perovskite solar cells: Insights from the drift-diffusion model," *J. Appl. Phys.* **133**, 095001 (2023).
- <sup>45</sup>W. Clarke, G. Richardson, and P. Cameron, "Understanding the full zoo of perovskite solar cell impedance spectra with the standard drift-diffusion model," *Adv. Energy Mater.* **14**, 2400955 (2024).
- <sup>46</sup>O. Almora, Y. Zhao, X. Du, T. Heumueller, G. J. Matt, G. Garcia-Belmonte, and C. J. Brabec, "Light intensity modulated impedance spectroscopy (LIMIS) in all-solid-state solar cells at open-circuit," *Nano Energy* **75**, 104982 (2020).
- <sup>47</sup>E. Ghahremanirad, O. Almora, S. Suresh, A. A. Drew, T. H. Chowdhury, and A. R. Uhl, "Beyond protocols: Understanding the electrical behavior of perovskite solar cells by impedance spectroscopy," *Adv. Energy Mater.* **13**, 2204370 (2023).
- <sup>48</sup>J. Diekmann, F. Peña-Camargo, N. Tokmoldin, J. Thiesbrummel, J. Warby, E. Gutierrez-Partida, S. Shah, D. Neher, and M. Stolterfoht, "Determination of mobile ion densities in halide perovskites via low-frequency capacitance and charge extraction techniques," *J. Phys. Chem. Lett.* **14**, 4200 (2023).
- <sup>49</sup>M. A. Green, *Solar Cells. Operating Principles, Technology and System Applications* (Prentice-Hall, 1982).
- <sup>50</sup>P. Lopez-Varo, J. A. Jiménez-Tejada, M. García-Rosell, S. Ravishankar, G. Garcia-Belmonte, J. Bisquert, and O. Almora, "Device physics of hybrid perovskite solar cells: Theory and experiment," *Adv. Energy Mater.* **8**, 1702772 (2018).
- <sup>51</sup>J. Bisquert, "Interpretation of the recombination lifetime in halide perovskite devices by correlated techniques," *J. Phys. Chem. Lett.* **13**, 7320 (2022).
- <sup>52</sup>M. T. Neukom, A. Schiller, S. Zülfie, E. Knapp, J. Ávila, D. Pérez-del-Rey, C. Dreessen, K. P. S. Zanoni, M. Sessolo, H. J. Bolink, and B. Ruhstaller, "Consistent device simulation model describing perovskite solar cells in steady-state, transient, and frequency domain," *ACS Appl. Mater. Interfaces* **11**, 23320 (2019).
- <sup>53</sup>M. T. Neukom, S. Zülfie, E. Knapp, M. Makha, R. Hany, and B. Ruhstaller, "Why perovskite solar cells with high efficiency show small IV-curve hysteresis," *Sol. Energy Mater. Sol. Cells* **169**, 159 (2017).
- <sup>54</sup>J. Xiang, Y. Li, F. Huang, and D. Zhong, "Effect of interfacial recombination, bulk recombination and carrier mobility on the J-V hysteresis behaviors of perovskite solar cells: A drift-diffusion simulation study," *Phys. Chem. Chem. Phys.* **21**, 17836 (2019).
- <sup>55</sup>A. Singh, W. Kaiser, and A. Gagliardi, "Role of cation-mediated recombination in perovskite solar cells," *Sol. Energy Mater. Sol. Cells* **221**, 110912 (2021).
- <sup>56</sup>D. Pitarch-Tena, T. T. Ngo, M. Vallés-Pelarda, T. Pauporté, and I. Mora-Seró, "Impedance spectroscopy measurements in perovskite solar cells: Device stability and noise reduction," *ACS Energy Lett.* **3**, 1044 (2018).
- <sup>57</sup>D. Klotz, G. Tumen-Ulzii, C. Qin, T. Matsushima, and C. Adachi, "Detecting and identifying reversible changes in perovskite solar cells by electrochemical impedance spectroscopy," *RSC Adv.* **9**, 33436 (2019).
- <sup>58</sup>S. M. Abdulrahim, Z. Ahmad, J. Bhadra, and N. J. Al-Thani, "Long-term stability analysis of 3D and 2D/3D hybrid perovskite solar cells using electrochemical impedance spectroscopy," *Molecules* **25**, 5794 (2020).
- <sup>59</sup>B. Hailegnaw, N. S. Sariciftci, and M. C. Scharber, "Impedance spectroscopy of perovskite solar cells: Studying the dynamics of charge carriers before and after continuous operation," *Phys. Status Solidi A* **217**, 2000291 (2020).
- <sup>60</sup>J. Torres, I. Zarazua, D. Esparza, J. M. Rivas, M. Saliba, I. Mora-Seró, S.-H. Turren-Cruz, and A. Abate, "Degradation analysis of triple-cation perovskite solar cells by electrochemical impedance spectroscopy," *ACS Appl. Energy Mater.* **5**, 12545 (2022).
- <sup>61</sup>J. Valle-Pulido, O. E. Solis, D. Esparza, R. Arturo Rodríguez-Rojas, S.-H. Turren-Cruz, J. M. Rivas, and I. Zarazúa, "Degradation analysis of perovskite solar cells doped with  $\text{MABr}_3$  via electrochemical impedance," *Sol. Energy* **258**, 148 (2023).
- <sup>62</sup>I. Matacena, P. Guerrero, L. Lancellotti, B. Alfano, A. De Maria, V. La Ferrara, L. V. Mercaldo, M. L. Miglietta, T. Polichetti, G. Rametta, G. V. Sannino, P. Delli Veneri, and S. Daliento, "Impedance spectroscopy analysis of perovskite solar cell stability," *Energies* **16**, 4951 (2023).
- <sup>63</sup>O. Almora, P. Lopez-Varo, K. T. Cho, S. Aghazada, W. Meng, Y. Hou, C. Echeverría-Arrondo, I. Zimmermann, G. J. Matt, J. A. Jiménez-Tejada, C. J. Brabec, M. K. Nazeeruddin, and G. Garcia-Belmonte, "Ionic dipolar switching hinders charge collection in perovskite solar cells with normal and inverted hysteresis," *Sol. Energy Mater. Sol. Cells* **195**, 291 (2019).
- <sup>64</sup>M. Fischer, D. Kiermasch, L. Gil-Escríg, H. J. Bolink, V. Dyakonov, and K. Tvingstedt, "Assigning ionic properties in perovskite solar cells: A unifying transient simulation/experimental study," *Sustainable Energy Fuels* **5**, 3578 (2021).
- <sup>65</sup>O. Almora, K. T. Cho, S. Aghazada, I. Zimmermann, G. J. Matt, C. J. Brabec, M. K. Nazeeruddin, and G. Garcia-Belmonte, "Discerning recombination mechanisms and ideality factors through impedance analysis of high-efficiency perovskite solar cells," *Nano Energy* **48**, 63 (2018).
- <sup>66</sup>L. Krückemeier, Z. Liu, T. Kirchartz, and U. Rau, "Quantifying charge extraction and recombination using the rise and decay of the transient photovoltage of perovskite solar cells," *Adv. Mater.* **35**, 2300872 (2023).
- <sup>67</sup>L. Rakocevic, F. Ernst, N. T. Yimga, S. Vashishtha, T. Aernouts, T. Heumueller, C. J. Brabec, R. Gehlhaar, and J. Poortmans, "Reliable performance comparison of perovskite solar cells using optimized maximum power point tracking," *Sol. RRL* **3**, 1800287 (2019).
- <sup>68</sup>M. V. Khenkin, E. A. Katz, A. Abate, G. Bardizza, J. J. Berry, C. Brabec, F. Brunetti, V. Bulović, Q. Burlingame, A. Di Carlo, R. Cheachareon, Y.-B. Cheng, A. Colsmann, S. Cros, K. Domanski, M. Dusza, C. J. Fell, S. R. Forrest, Y. Galagan, D. Di Girolamo, M. Grätzel, A. Hagfeldt, E. von Hauff, H. Hoppe, J. Kettle, H. Köbler, M. S. Leite, S. Liu, Y.-L. Loo, J. M. Luther, C.-Q. Ma, M. Madsen, M. Manceau, M. Matheron, M. McGhee, R. Meitzner, M. K. Nazeeruddin, A. F. Nogueira, Ç Odabaşı, A. Osharov, N.-G. Park, M. O. Reese, F. De Rossi, M. Saliba, U. S. Schubert, H. J. Snaith, S. D. Stranks, W. Tress, P. A. Troshin, V. Turkovic, S. Veenstra, I. Visoly-Fisher, A. Walsh, T. Watson, H. Xie, R. Yıldırım, S. M. Zakeeruddin, K. Zhu, and M. Lira-Cantu, "Consensus statement for stability assessment and reporting for perovskite photovoltaics based on ISOS procedures," *Nat. Energy* **5**, 35 (2020).
- <sup>69</sup>C. Wang, L. Huang, Y. Zhou, Y. Guo, K. Liang, T. Wang, X. Liu, J. Zhang, Z. Hu, and Y. Zhu, "Perovskite solar cells in the shadow: Understanding the mechanism of reverse-bias behavior toward suppressed reverse-bias breakdown and reverse-bias induced degradation," *Adv. Energy Mater.* **13**, 2203596 (2023).
- <sup>70</sup>A. Farooq, M. R. Khan, T. Abzieher, A. Voigt, D. C. Lupascu, U. Lemmer, B. S. Richards, and U. W. Paetzold, "Photodegradation of triple-cation perovskite solar cells: The role of spectrum and bias conditions," *ACS Appl. Energy Mater.* **4**, 3083 (2021).
- <sup>71</sup>K. Domanski, E. A. Alharbi, A. Hagfeldt, M. Grätzel, and W. Tress, "Systematic investigation of the impact of operation conditions on the degradation behaviour of perovskite solar cells," *Nat. Energy* **3**, 61 (2018).
- <sup>72</sup>J. Mohanraj, B. Samanta, O. Almora, R. Escalante, L. Marsal, S. Jenatsch, A. Gadola, B. Ruhstaller, J. Anta, M. Caspary Toroker, and S. Olthof, " $\text{NiO}_x$  passivation in perovskite solar cells: From surface reactivity to device performance," *ACS Appl. Mater. Interfaces* **16**, 42835 (2024).
- <sup>73</sup>P. Calado, I. Gelmetti, B. Hilton, M. Azzouzi, J. Nelson, and P. R. F. Barnes, "Driftfusion: An open source code for simulating ordered semiconductor devices with mixed ionic-electronic conducting materials in one dimension," *J. Comput. Electron.* **21**, 960 (2022).
- <sup>74</sup>R. Garcia-Rodríguez, A. J. Riquelme, M. Cowley, K. Valadez-Villalobos, G. Oskam, L. J. Bennett, M. J. Wolf, L. Contreras-Bernal, P. J. Cameron, A. B. Walker, and J. A. Anta, "Inverted hysteresis in n-i-p and p-i-n perovskite solar cells," *Energy Technol.* **10**, 2200507 (2022).

- <sup>75</sup>C. C. Boyd, R. C. Shallcross, T. Moot, R. Kerner, L. Bertoluzzi, A. Onno, S. Kavadiya, C. Chosy, E. J. Wolf, J. Werner, J. A. Raiford, C. de Paula, A. F. Palmstrom, Z. J. Yu, J. J. Berry, S. F. Bent, Z. C. Holman, J. M. Luther, E. L. Ratcliff, N. R. Armstrong, and M. D. McGehee, "Overcoming redox reactions at perovskite-nickel oxide interfaces to boost voltages in perovskite solar cells," *Joule* **4**, 1759 (2020).
- <sup>76</sup>W. Song, X. Zhang, S. Lammar, W. Qiu, Y. Kuang, B. Ruttens, J. D'Haen, I. Vaesen, T. Conard, Y. Abdulraheem, T. Aernouts, Y. Zhan, and J. Poortmans, "Critical role of perovskite film stoichiometry in determining solar cell operational stability: A study on the effects of volatile A-cation additives," *ACS Appl. Mater. Interfaces* **14**, 27922 (2022).
- <sup>77</sup>S. Ravishankar, Z. Liu, U. Rau, and T. Kirchartz, "Multilayer capacitances: How selective contacts affect capacitance measurements of perovskite solar cells," *PRX Energy* **1**, 013003 (2022).
- <sup>78</sup>D. Abdel, P. Vágner, J. Fuhrmann, and P. Farrell, "Modelling charge transport in perovskite solar cells: Potential-based and limiting Ion depletion," *Electrochim. Acta* **390**, 138696 (2021).
- <sup>79</sup>P. Lopez-Varo, J. A. Jiménez-Tejada, M. García-Rosell, J. A. Anta, S. Ravishankar, A. Bou, and J. Bisquert, "Effects of ion distributions on charge collection in perovskite solar cells," *ACS Energy Lett.* **2**, 1450 (2017).
- <sup>80</sup>A. Riquelme, L. J. Bennett, N. E. Courtier, M. J. Wolf, L. Contreras-Bernal, A. B. Walker, G. Richardson, and J. A. Anta, "Identification of recombination losses and charge collection efficiency in a perovskite solar cell by comparing impedance response to a drift-diffusion model," *Nanoscale* **12**, 17385 (2020).
- <sup>81</sup>O. Almora, M. García-Batlle, and G. Garcia-Belmonte, "Utilization of temperature-sweeping capacitive techniques to evaluate band gap defect densities in photovoltaic perovskites," *J. Phys. Chem. Lett.* **10**, 3661 (2019).

*Supporting information:*

# Stability Analysis of Perovskite Solar Cells via Short-Circuit Impedance Spectroscopy: A case study on NiO<sub>x</sub> passivation

Osbel Almora,<sup>1,\*</sup> Pilar López-Varo,<sup>2,\*</sup> Renán Escalante,<sup>3</sup> John Mohanraj,<sup>4</sup> Lluis F. Marsal,<sup>1</sup> Selina Olthof,<sup>4</sup> Juan A. Anta<sup>3,\*</sup>

<sup>1</sup> Departament d'Enginyeria Electrònica Elèctrica i Automàtica, Universitat Rovira i Virgili, 43007 Tarragona, Spain

<sup>2</sup> Institut Photovoltaïque d'Ile-de-France (IPVF), 91120 Palaiseau, France

<sup>3</sup> Department of Physical, Chemical and Natural Systems, Universidad Pablo de Olavide, Sevilla 41013, Spain

<sup>4</sup> Department of Chemistry, University of Cologne, Greinstrasse 4–6, Cologne 50939, Germany

\* [osbel.almora@urv.cat](mailto:osbel.almora@urv.cat), [pilar.lopez-varo@ipvf.fr](mailto:pilar.lopez-varo@ipvf.fr), [jaantmon@upo.es](mailto:jaantmon@upo.es)

## S1. Introduction

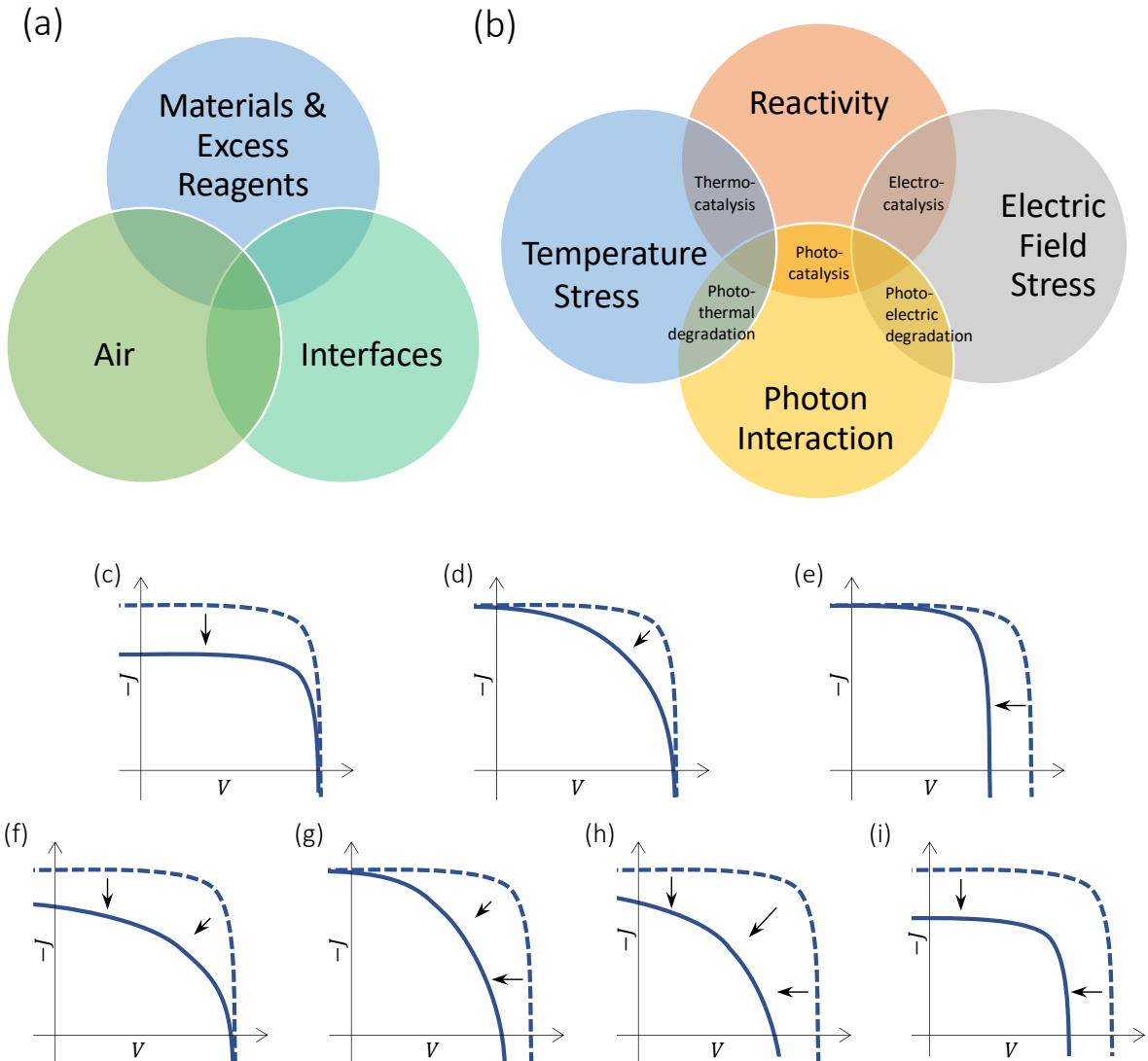


**Figure S1.** Schemed interconnection of different degradation (a) elements and (b) mechanisms. Schemed different types of degradation effects on the current-voltage curve: sole or significantly dominant decrease of the (c) short-circuit current density ( $J_{sc}$ ), (d) fill factor (FF) and, (e) open-circuit voltage ( $V_{oc}$ ); and combined reduction of (f)  $J_{sc} + FF$ , (g)  $V_{oc} + FF$ , (h)  $V_{oc} + J_{sc} + FF$ , and (i)  $V_{oc} + J_{sc}$ .

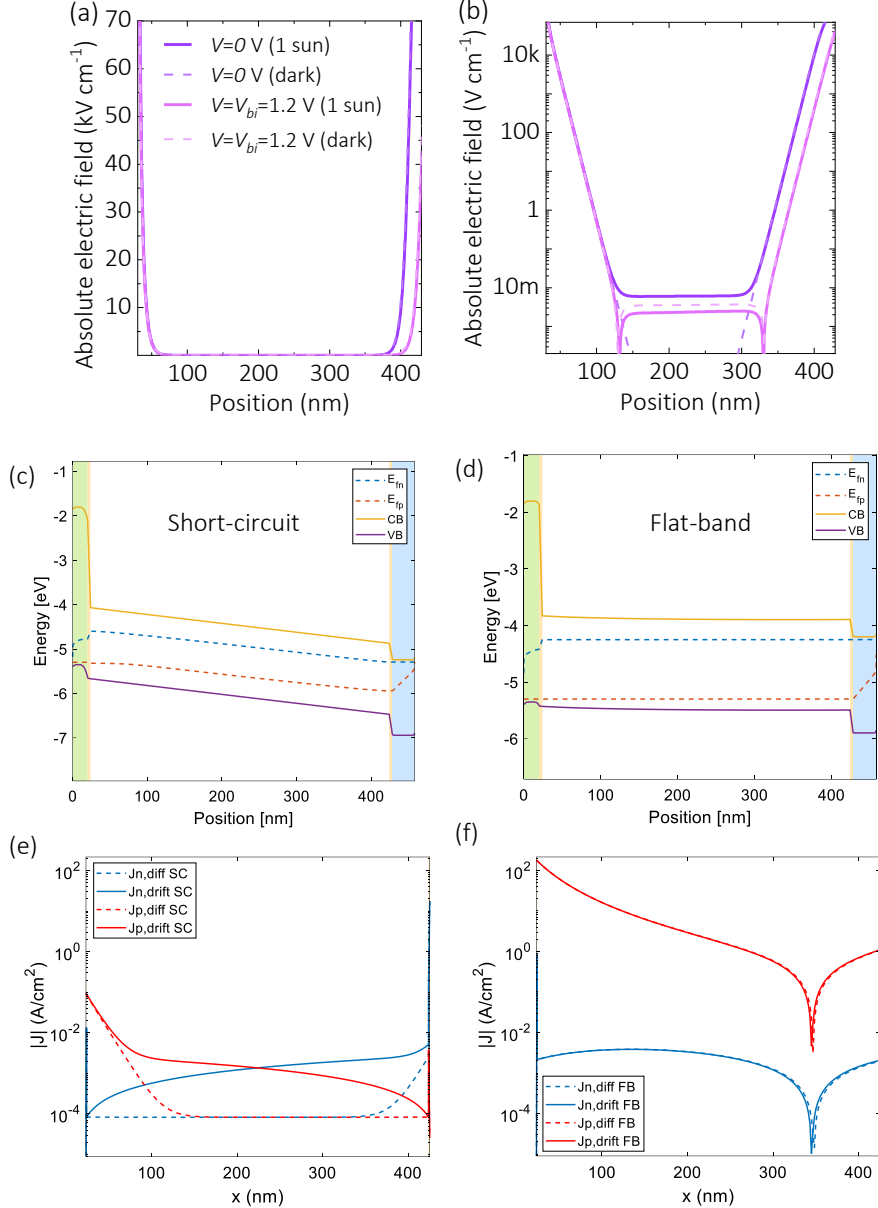


**Figure S2.** Simulated steady-state electric field of the reference PSCs assuming a concentration of mobile cations of  $10^{18} \text{ cm}^{-3}$  in linear (a) and semilogarithmic (b) scales with the structure in Figure 1a (main manuscript). Setfos-Fluxim<sup>[1]</sup> was used for these simulations. The energy band diagrams in (c) short-circuit and (d) flat-band and their respective drift and diffusion currents (e, f) where simulated with Driftfusion<sup>[2]</sup> for a mobile ion density of  $10^{15} \text{ cm}^{-3}$ .

**Table S1.** Dependency of shunt resistance ( $R_{sh}$ ) and/or short-circuit resistance as a function of illumination intensity ( $P_{in}$ ).

Absorber material	Dependency	Ref.	Comment
c-Si	$R_{sc} \propto P_{in}^{-1.13}$	[3]	
a-Si:H	$R_{sc} \propto J_{sc}^{-1}$	[4]	AM1.5G spectrum
Si	$R_{sh} = R_0 - R_1 \left( \frac{P_{in}}{P_0} \right)^{1.08}$	[5]	Polycrystalline silicon; $R_0$ , $R_1$ and $P_0$ are independent of $P_{in}$
c-Si	$R_{sh} = \frac{R_0}{1 + \frac{P_0}{P_{in}}}$	[6]	$R_0$ and $P_0$ are independent of $P_{in}$
CdTe	$R_{sh} \propto P_{in}^{-0.86}$	[7]	
PBDB-T:F-M	$R_p \propto P_{in}^{-1}$	[8]	

## **S2. Device fabrication and initial performance characterization.**

The description below is adapted from our simultaneous work.<sup>[9]</sup>

### **S2.1. Material acquisition**

For MAPbI<sub>3</sub> layer deposition, PbI<sub>2</sub> and MAI were purchased from TCI Deutschland GmbH. The dry solvents dimethylformamide ( $\geq$  99.9%), chlorobenzene, ethanol (99.9%), isopropanol (Honeywell 99.9%), and ethanolamine were purchased from Sigma-Aldrich and used as received. Nickel(II) acetate tetrahydrate, HI (57 wt%), Li-TFSI, 1-phenylethylamine, 1,2-ethanedithiol, 1-iodobutane, C<sub>60</sub> and bathocuproine were also purchased from Sigma-Aldrich or Merck KGaA. The FTO-coated glass substrates (TEC 10, S2002S1) used for NiO<sub>x</sub> deposition as well as solar cells preparation were procured from Ossila BV, The Netherlands.

### **S2.2. Preparation of NiO<sub>x</sub> thin films**

First, 400 mg of nickel (II) acetate tetrahydrate and 97  $\mu$ L of ethanolamine were mixed in 3.2 mL of ethanol, resulting in 0.5 M solution. This solution was stirred for at 2 hours (minimum) at room temperature to obtain a transparent dark blue-greenish colored solution. Subsequently, the solution was filtered with a 0.2  $\mu$ m PTFE filter, and then 100  $\mu$ L of it was spin-coated on clean FTO (TEC 10) substrates at 3000 rpm for 30 s. Immediately after, the substrates were annealed at 100 °C for 5 minutes inside a N<sub>2</sub> glovebox and then at 450 °C for 30 min in a furnace. Once the substrates were cooled to room temperature, they were transferred into a N<sub>2</sub> filled glovebox. Prior depositing any further layer on, the substrates were heated to 100 °C for 10 min.

### **S2.3. Preparation of MAPbI<sub>3</sub> thin films**

MAPbI<sub>3</sub> films for degradation studies and solar cells were prepared by following the conventional antisolvent method.<sup>[9]</sup> For degradation studies, 1 M of MAI and PbI<sub>2</sub> were dissolved in dimethylformamide by stirring the solution for at least 2 h at 50 °C inside a N<sub>2</sub> filled glovebox, and the solution was filtered with a 0.2  $\mu$ m PTFE filter. This was used as a stock solution to prepare 0.5 M, 0.375 M, 0.25 and 0.1 M MAPbI<sub>3</sub> solutions by diluting with appropriate amount of dimethylformamide. For film preparation, 80  $\mu$ L of MAPbI<sub>3</sub> solution of desired concentration was spin coated on substrates at 3000 rpm for 50 s. During this process, after 8 s, 200  $\mu$ L of chlorobenzene was dripped continuously onto the substrates. The substrates were then annealed at 80 °C for 1 h on a hot plate inside a glovebox.

### **S2.4. Deposition of surface passivation materials on NiO<sub>x</sub>**

In separate vials, 0.1 M solutions of Li-TFSI, 1-phenylethanol amine, 1-iodobutane, HI, MAI and 1,2-ethanedithiol were prepared in isopropanol and dimethylformamide was used as a solvent for 0.1 M solution of PbI<sub>2</sub>. These solutions were stirred at room temperature and filtered with 0.2  $\mu$ m PTFE filter. At that time, 80  $\mu$ L of the filtered solution of desired passivating material was spin coated on FTO/NiO<sub>x</sub> substrates at 3000 rpm for 50 s and then annealed at 100 °C for 15 min on a hotplate inside a N<sub>2</sub> filled glove box. Importantly, the substrates were then washed with a copious amount of the respective solvent (isopropanol or dimethylformamide) and dried with a N<sub>2</sub> gun to remove any unbound material from the NiO<sub>x</sub> surface. These substrates were used as such for further analysis or to prepare further samples by depositing MAPbI<sub>3</sub> films.

### **S2.5. Fabrication of perovskite solar cells**

All solar cells were prepared by using etched FTO substrates with a 20-30 nm thick NiO<sub>x</sub> hole transport layer prepared from 0.2 M nickel (II) acetate tetrahydrate and ethanolamine mixture in ethanol. On NiO<sub>x</sub> layer, passivating materials (0.1 M solution) and MAPbI<sub>3</sub> (from 1 M solution, 350-400 nm thick) were deposited by following the procedures described above. The substrates were then moved to an evaporation chamber, where C<sub>60</sub> electron transport layer (30 nm) and bathocuproine (8 nm) were evaporated. Finally, the devices were completed with Ag cathode (100 nm) deposition. Each substrate contains 7 devices with an active area of 0.0785 cm<sup>2</sup>, defined by the deposited Ag cathode (see **Figure S3**).

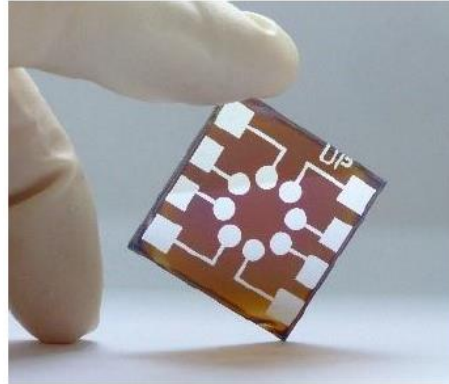


**Figure S3.** Photography of the studied samples with an active area of  $0.0785 \text{ cm}^2$ .

## S2.6. Device performance

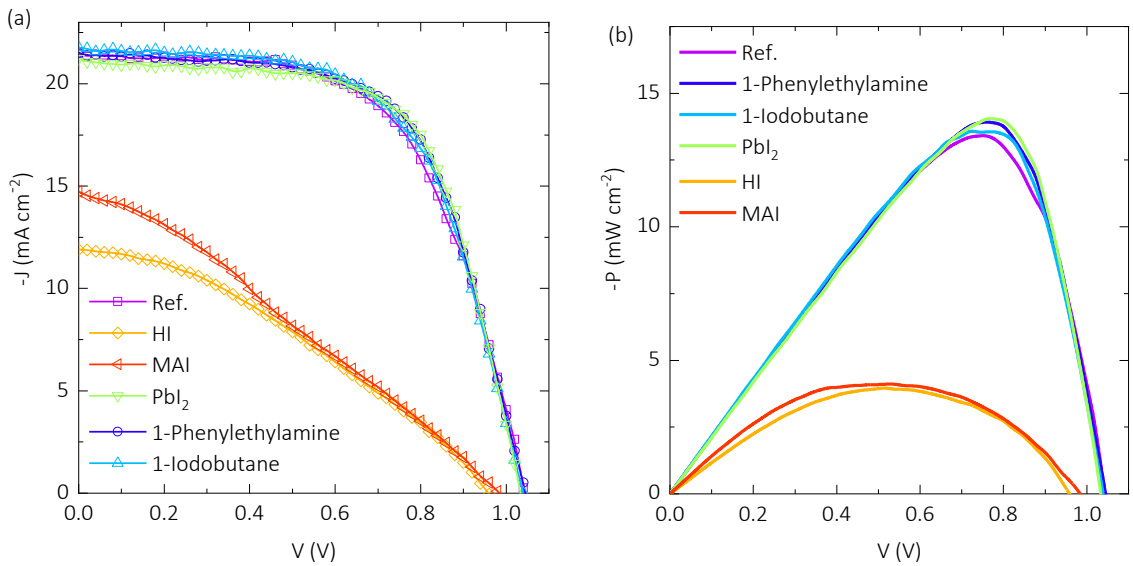


**Figure S4.** Representative as-fabricated current density-voltage ( $J - V$ ) curves under standard 1 sun illumination. In each case, the best two pixels per substrate are shown for two bias scan directions at a scan rate of 70 mV/s.

**Table S2.** Summary of best performance samples in terms of power conversion efficiency from  $J - V$  curves under standard 1 sun illumination.

Sample	Reverse scan				Forward scan			
	$V_{oc}$ (V)	$J_{sc}$ ( $\text{mA}\cdot\text{cm}^{-2}$ )	FF (%)	PCE (%)	$V_{oc}$ (V)	$J_{sc}$ ( $\text{mA}\cdot\text{cm}^{-2}$ )	FF (%)	PCE (%)
Ref.	1.04	20.0	64	13.4	1.01	19.6	68	13.4
Phenylethylamine	1.04	21.5	62	13.8	1.02	20.7	68	14.4
Iodobutane	1.04	21.8	60	13.6	1.02	20.8	67	14.1
PbI <sub>2</sub>	1.03	21.2	64	14.1	1.01	20.0	73	14.7
HI	0.96	11.9	35	4.0	0.96	11.8	38	4.3
MAI	0.98	14.7	29	4.2	0.99	15.3	34	5.2

## S3. Impedance spectra in short-circuit at different illumination intensities

### S3.1. Experimental Procedure and Equivalent Circuit Modelling

For AC measurements, it is the capacitance coupling that reveals the presence of more than one characteristic resistances. However, the numerical approach of ECs cannot discern whether these resistances are series or parallel connected, which requires further physical considerations. In all cases, for each resistance contribution in a one-

dimensional (1D) stack (e.g., the PSC), there always are experimental deviations from the 1D symmetry (e.g., borders, grain boundaries, pin holes) which lead to leakage current.<sup>[10]</sup> This is well-known in the DC measurements where  $R_{sh}$  is extracted as the diode resistance deviate from the exponential increase of  $R_d$  towards reverse bias. The parallel configuration of  $R_d$  and  $R_{sh}$  is not only true for the effective total resistances, but also for each layer or section within the 1D stack (see **Figure S5b**). Therefore, the  $R_{sh}$  contribution to the IS spectra is typically neglected in near flat band conditions (e.g., open circuit with  $\sim 1$  sun illumination) because  $R_d \ll R_{sh}$ , as schemed in **Figure S5c**. In contrast, since at short-circuit the  $R_d \gg R_{sh}$ , one can assume that  $R_{Hf}$  and  $R_{Lf}$  in the IS spectra approach to the corresponding  $R_{sh,Hf}$  and  $R_{sh,Lf}$ , neglecting the contribution of the parallel  $R_{d,Hf}$  and  $R_{d,Lf}$ , respectively, as depicted in **Figure S5d**. In all cases, the Hf and Lf resistances indicate their physical origin from consecutive sections in the 1D stack. Importantly, a third inconvenient scenario cannot be discarded for which  $R_d \approx R_{sh}$  hinder the separation of contributions from the leakage current and that of the 1D stack, as presented in **Figure S5e**. This is a challenging aspect for understanding the resistance at short-circuit.

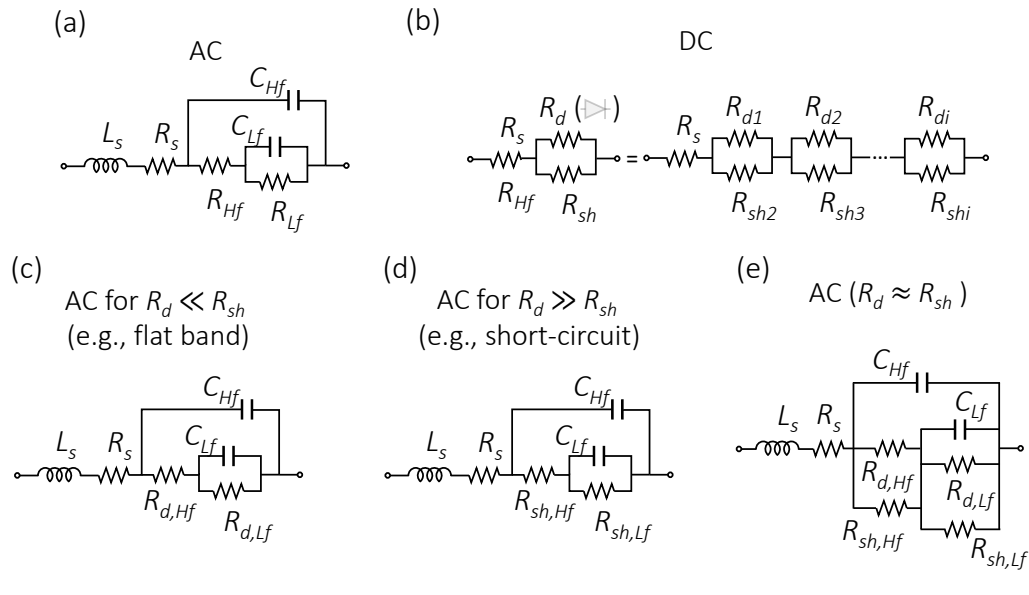


**Figure S5.** Equivalent circuit models for AC (a, c, d, e) and DC (b) measurements. The effective total diode and shunt resistance in (b) is illustratively decomposed in the series connection of “i” layers forming the device. Neglecting the physical meaning of capacitance, the resistance for different cases of shunt resistance is schemed in (c-e), as indicated.

The impedance spectroscopy was measured with an Autolab PGSTAT302N potentiostat including a FRA32M unit and a kit Autolab Optical Bench from MetroOhm. The samples were illuminated with a white LED at different steady-state illumination intensities, then the short-circuit (SC) condition was applied ( $V=0V$ ), allowing a direct current (DC) density  $J_{sc}$ . Upon these DC condition the 15 mV perturbation was applied for measuring the impedance spectroscopy (IS) as a function of the  $J_{sc}$  for each illumination intensity. Subsequently, the IS spectra were fitted to the equivalent circuit (EC) models of Figure 2a and **Figure S5**.

The resistance parameters at SC extracted from the EC models were subsequently parameterized as a function of  $J_{sc}$ , following the empirical equation

$$R_{sc} = R_s + \frac{R_{sh0}}{\left(1 + \frac{J_{sc}}{J_\sigma}\right)} \quad (S1)$$

where  $R_s$  is the series resistance;  $R_{sh0}$ , the equilibrium (dark) shunt resistance; and  $J_\sigma$  is the short-circuit current density corresponding to the threshold illumination intensity whose charge carrier concentration at SC increases photoconductivity, thus decreasing the resistance. Notably,  $R_{sc} \cong R_{sh}/2$  for  $J_{sc} = J_\sigma$ .

The capacitance parameters at SC extracted from the EC model were subsequently parameterized as a function of  $J_{sc}$ , following the empirical equation

$$C_{sc} = C_0 \left(1 + \left(\frac{J_{sc}}{J_\varepsilon}\right)^p\right) \quad (S2)$$

where  $C_0$  is the equilibrium (dark) SC capacitance;  $p$  is a dimensionless power parameter, and  $J_\varepsilon$  is the short-circuit current density corresponding to the threshold illumination intensity whose charge carrier concentration at SC enables a capacitive regime transition from a purely dielectric response (geometric or space-charge capacitance) to a presumably mobile ions-related behaviour. Notably,  $C_{sc} \cong 2R_{sh}$  for  $J_{sc} = J_\varepsilon$  and dielectric contributions which are independent of the light intensity would require significantly large threshold currents ( $J_\varepsilon \rightarrow \infty \Rightarrow C_{sc} = C_0$ )

The characteristic response times for each mechanism can be extracted via the estimation of the corresponding peak maxima across the Bode plots of the imaginary part of the impedance, and/or by considering the resistor-capacitor coupling ( $R \cdot C$  product) assumed in the EC model. Either way, the behaviour of the response times follows the empirical equation

$$\tau_{sc} = \frac{\tau_0}{\left(1 + \frac{J_{sc}}{J_\sigma}\right)} \left(1 + \left(\frac{J_{sc}}{J_\varepsilon}\right)^p\right) \quad (\text{S3})$$

where  $\tau_0 \approx R_{sh0}C_0$  is the characteristic equilibrium (dark) response time constant. Importantly, Equation (S3) behaves constant for  $p=1$  in the high illumination intensity limit ( $J_{sc} \rightarrow \infty \Rightarrow \tau_{sc} = \tau_0 J_\sigma / J_\varepsilon$ ); provided equal threshold currents and/or in the low illumination intensity limit ( $J_\sigma = J_\varepsilon \vee J_{sc} \rightarrow 0 \Rightarrow \tau_{sc} = \tau_0$ ).

### S3.2. Experimental impedance spectroscopy data and equivalent circuit fittings for different illumination intensities

#### S3.3. NiO<sub>x</sub>Ref

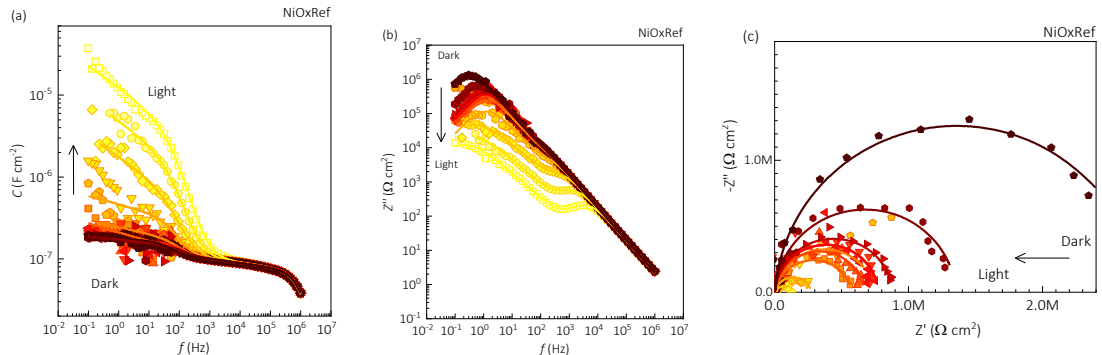


**Figure S6.** Impedance spectra for the **NiO<sub>x</sub>Ref** Sample in SC under different DC illumination intensities in (a) capacitance and (b) imaginary Bode, and (c) impedance Nyquist representations. In each case, the dots indicate experimental data, the lines are the numerical simulations via EC model, and darker and lighter colours indicate low and high illumination intensities (and  $J_{sc}$  values), respectively.

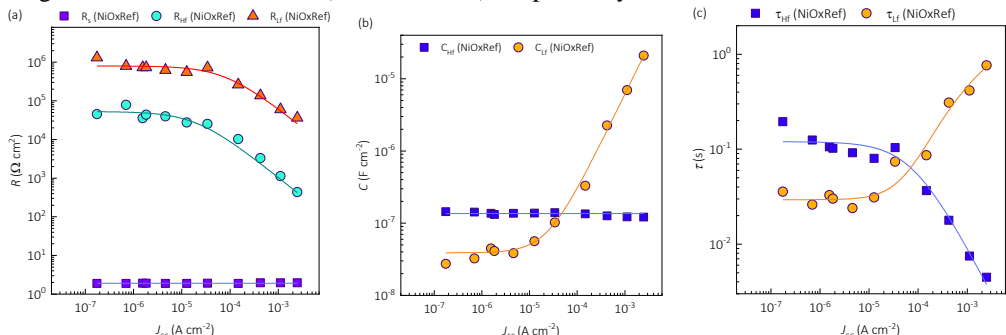


**Figure S7.** Resistance (a), capacitance (b), and characteristic times (c) from the EC models for IS spectra in SC of the **NiO<sub>x</sub> Ref.** sample under different DC illumination intensities. In each case, the dots indicate fitted parameters from the EC model, and the lines are the numerical simulations to the analytical trends of equations (S1), (S2), and (S3) for (a), (b), and (c), respectively.

**Table S3.** Parameterization of photovoltage trend from the EC modelling following Equations (S1), (S2), (S3) and from the IS spectra of the sample **NiO<sub>x</sub> Ref.** in SC.

Parameters	$R_s$	$R_{HF}$	$R_{LF}$	$C_{HF}$	$C_{LF}$	$\tau_{HF}$	$\tau_{LF}$
$R_s$ ( $\Omega \cdot \text{cm}^2$ )	1.90	—	—	—	—	—	—
$R_{sh}$ ( $\Omega \cdot \text{cm}^2$ )	—	58053	8E5	—	—	—	—
$J_\sigma$ ( $\text{A} \cdot \text{cm}^{-2}$ )	—	2E-5	8.2E-5	—	—	8e-5	3.6E-4
$C_0$ ( $\text{F} \cdot \text{cm}^{-2}$ )	—	—	—	1.38E-7	3.93E-8	—	—
$J_\varepsilon$ ( $\text{A} \cdot \text{cm}^{-2}$ )	—	—	—	—	2.42E-5	—	5E-5
$p$ (a.u.)	—	—	—	—	1.35	—	1.35
$\tau_0$ (s)	—	—	—	—	—	0.0472	0.03
$V_{ph}$ (V)	—	—	—	—	—	—	—
$J_V$ ( $\text{A} \cdot \text{cm}^{-2}$ )	—	—	—	—	—	—	—

### S3.4. Amine

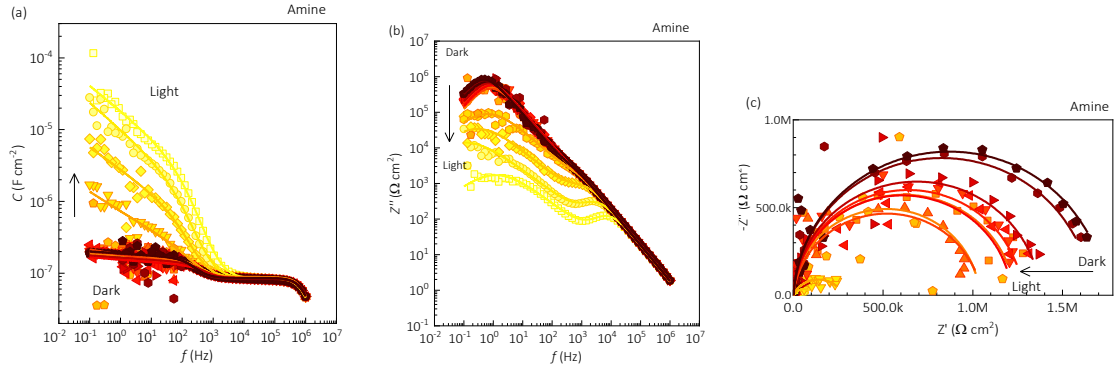


**Figure S8.** Impedance spectra for the **Amine** Sample in SC under different DC illumination intensities in (a) capacitance and (b) imaginary Bode, and (c) impedance Nyquist representations. In each case, the dots indicate experimental data, the lines are the numerical simulations via EC model, and darker and lighter colors indicate low and high illumination intensities (and  $J_{sc}$  values), respectively.

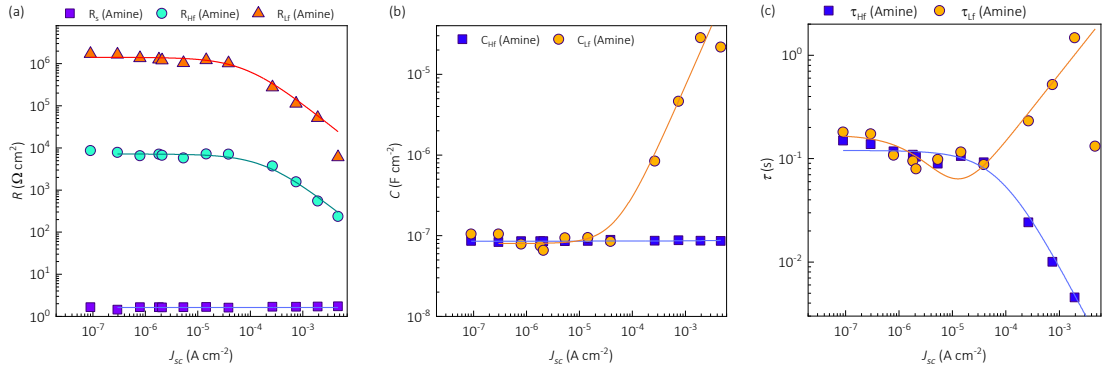


**Figure S9.** Results for (a) resistance, (b) capacitance, and (c) characteristic times extracted from the EC numerical modelling of the impedance spectra of the **Amine** sample in SC under different DC illumination intensities. In each case, the dots indicate fitted parameters from the EC model, and the lines are the numerical simulations to the analytical trends of equations (S1), (S2), and (S3) for (a), (b), and (c), respectively.

**Table S4.** Parameterization of photovoltage trend from the EC modeling following Equations (S1), (S2), (S3) and from the IS spectra of the sample Amine in SC.

Parameters	$R_s$	$R_{hf}$	$R_{lf}$	$C_{hf}$	$C_{lf}$	$\tau_{hf}$	$\tau_{lf}$
$R_s$ ( $\Omega \cdot \text{cm}^2$ )	1.61	—	—	—	—	—	—
$R_{sh}$ ( $\Omega \cdot \text{cm}^2$ )	—	6959	1.28E6	—	—	—	—
$J_\sigma$ ( $\text{A cm}^{-2}$ )	—	2E-4	8.2E-5	—	—	8.2e-5	3E-6
$C_0$ ( $\text{F cm}^{-2}$ )	—	—	—	8.7e-8	8E-8	—	—
$J_\epsilon$ ( $\text{A cm}^{-2}$ )	—	—	—	—	5E-5	—	1.3E-5
$p$ (a.u.)	—	—	—	—	1.5	—	1.65
$\tau_0$ (s)	—	—	—	—	—	0.12	0.17
$V_{ph}$ (V)	—	—	—	—	—	—	—
$J_V$ ( $\text{A cm}^{-2}$ )	—	—	—	—	—	—	—

### S3.5. Iodobutane

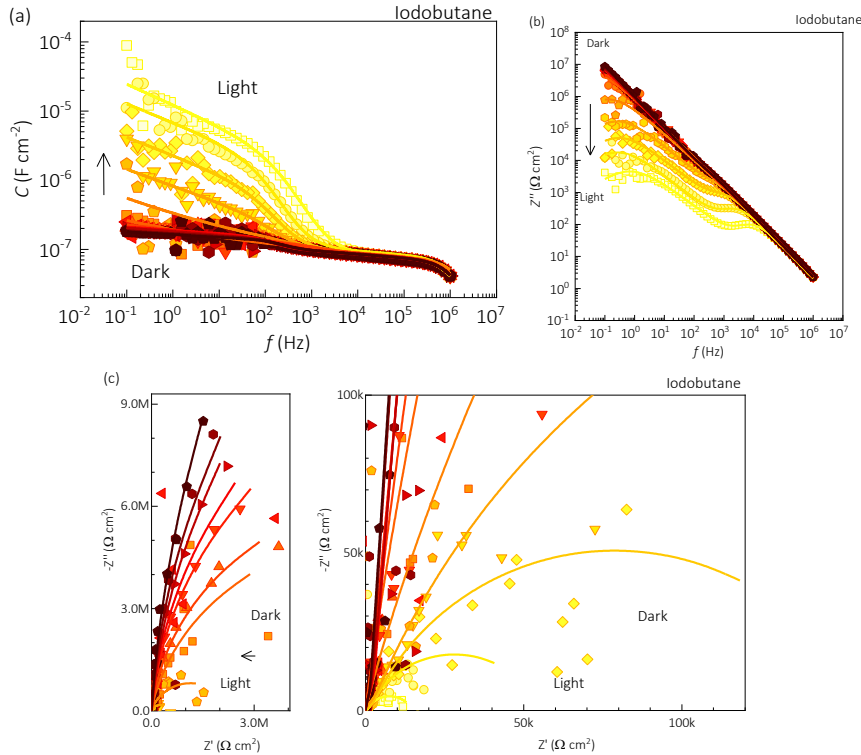


**Figure S10.** Impedance spectra for the **Iodobutane** Sample in SC under different DC illumination intensities in (a) capacitance and (b) imaginary Bode, and (c) impedance Nyquist representations. In each case, the dots indicate experimental data, the lines are the numerical simulations via EC model, and darker and lighter colours indicate low and high illumination intensities (and  $J_{sc}$  values), respectively.

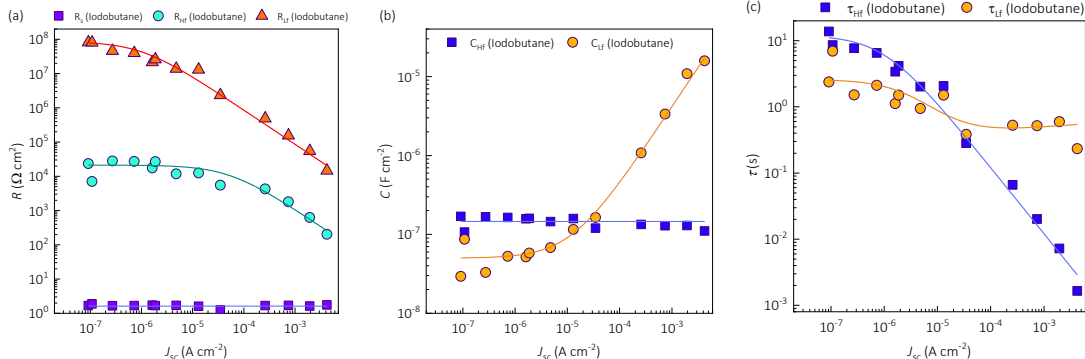


**Figure S11.** Results for (a) resistance, (b) capacitance, and (c) characteristic times extracted from the EC numerical modelling of the impedance spectra of the **Iodobutane** sample in SC under different DC illumination intensities. In each case, the dots indicate fitted parameters from the EC model, and the lines are the numerical simulations to the analytical trends of equations (S1), (S2), and (S3) for (a), (b), and (c), respectively.

**Table S5.** Parameterization of photovoltage trend from the EC modelling following Equations (S1), (S2), (S3) and from the IS spectra of the sample **Iodobutane** in SC.

Parameters	$R_s$	$R_{HF}$	$R_{LF}$	$C_{HF}$	$C_{LF}$	$\tau_{HF}$	$\tau_{LF}$
$R_s (\Omega \cdot \text{cm}^2)$	1.62	—	—	—	—	—	—
$R_{sh} (\Omega \cdot \text{cm}^2)$	—	21227	8.62E7	—	—	—	—
$J_\sigma (\text{A cm}^2)$	—	5.2E-5	1E-6	—	—	1E-6	3E-6
$C_0 (\text{F} \cdot \text{cm}^2)$	—	—	—	1.46E-7	5E-8	—	—
$J_e (\text{A cm}^2)$	—	—	—	—	1.22E-5	—	2E-5
$p$ (a.u.)	—	—	—	—	1.02	—	1.06
$\tau_0 (\text{s})$	—	—	—	—	—	12.1	2.6
$V_{ph} (\text{V})$	—	—	—	—	—	—	—
$J_V (\text{A cm}^2)$	—	—	—	—	—	—	—

### S3.6. HI

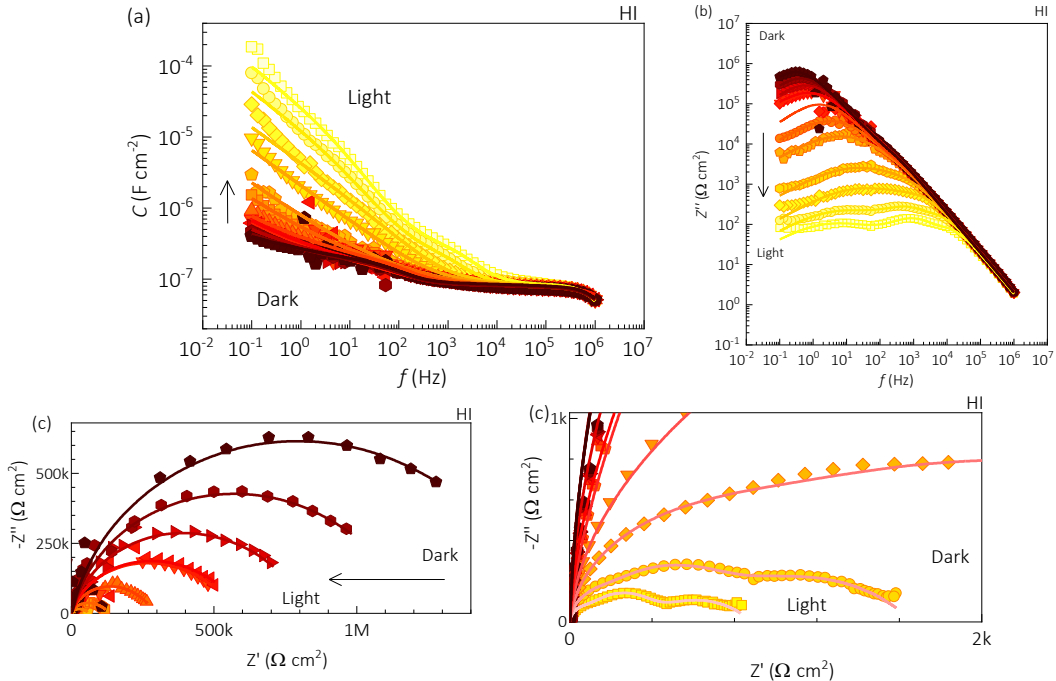


**Figure S12.** Impedance spectra for the **HI** Sample in SC under different DC illumination intensities in (a) capacitance and (b) imaginary Bode, and (c) impedance Nyquist representations. In each case, the dots indicate experimental data, the lines are the numerical simulations via EC model, and darker and lighter colors indicate low and high illumination intensities (and  $J_{sc}$  values), respectively.

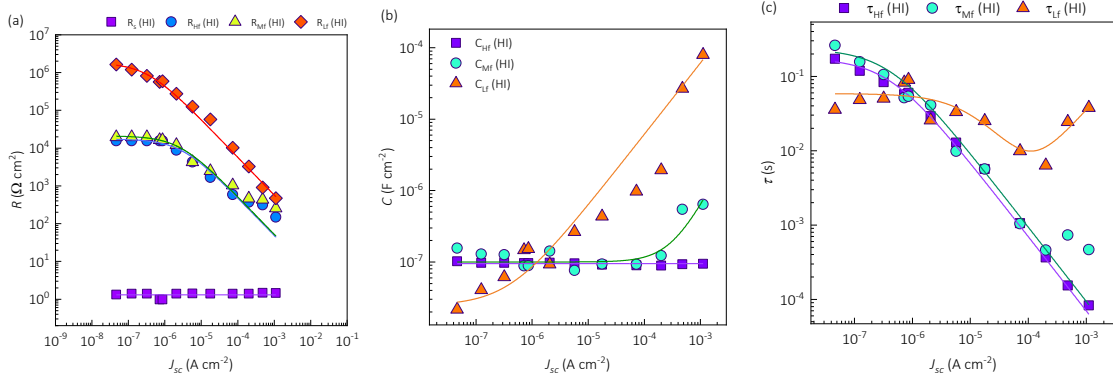


**Figure S13.** Results for (a) resistance, (b) capacitance, and (c) characteristic times extracted from the EC numerical modelling of the impedance spectra of the **HI** sample in SC under different DC illumination intensities. In each case, the dots indicate fitted parameters from the EC model, and the lines are the numerical simulations to the analytical trends of equations (S1), (S2), and (S3) for (a), (b), and (c), respectively.

**Table S6.** Parameterization of photovoltage trend from the EC modelling following Equations (S1), (S2), (S3) and from the IS spectra of the sample **HI** in SC.

Parameters	$R_s$	$R_{hf}$	$R_{mf}$	$R_{lf}$	$C_{hf}$	$C_{mf}$	$C_{lf}$	$\tau_{hf}$	$\tau_{mf}$	$\tau_{lf}$
$R_s$ ( $\Omega \cdot \text{cm}^2$ )	1.31	—	—	—	—	—	—	—	—	—
$R_{sh}$ ( $\Omega \cdot \text{cm}^2$ )	—	17342	21043	1.79E6	—	—	—	—	—	—
$J_s$ ( $\text{A cm}^{-2}$ )	—	2.82E-6	2.48E-6	3.19E-7	—	—	—	4E-7	4E-7	1.04E-5
$C_0$ ( $\text{F cm}^{-2}$ )	—	—	—	—	9.49E-8	1E-7	2.45E-8	—	—	—
$J_e$ ( $\text{A cm}^{-2}$ )	—	—	—	—	—	3.23E-4	4E-7	—	—	1.13E-4
p (a.u.)	—	—	—	—	—	1.5	1.00	—	—	1.86
$\tau_0$ (s)	—	—	—	—	—	—	—	0.175	0.234	0.0586
$V_{ph}$ (V)	—	—	—	—	—	—	—	—	—	—
$J_V$ ( $\text{A cm}^{-2}$ )	—	—	—	—	—	—	—	—	—	—

### S3.7. PbI<sub>2</sub>

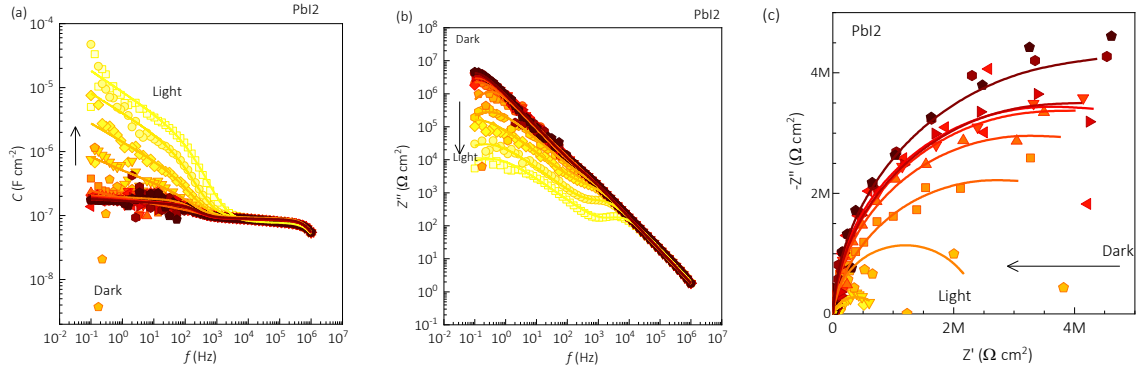


**Figure S14.** Impedance spectra for the **PbI<sub>2</sub>** Sample in SC under different DC illumination intensities in (a) capacitance and (b) imaginary Bode, and (c) impedance Nyquist representations. In each case, the dots indicate experimental data, the lines are the numerical simulations via EC model, and darker and lighter colors indicate low and high illumination intensities (and  $J_{sc}$  values), respectively.

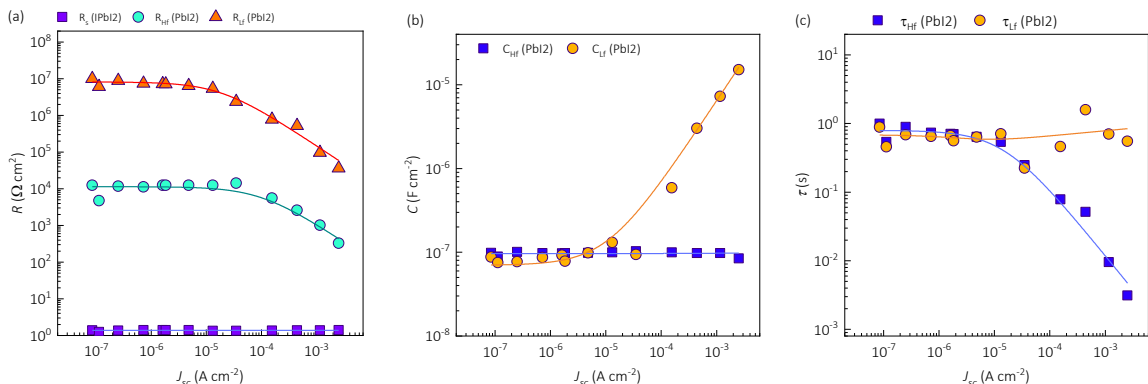


**Figure S15.** Results for (a) resistance, (b) capacitance, (c) characteristic times and (d) internal photovoltages extracted from the EC numerical modelling of the impedance spectra of the **HI** sample in SC under different DC illumination intensities. In each case, the dots indicate fitted parameters from the EC model, and the lines are the numerical simulations to the analytical trends of equations (S1), (S2), and (S3) for (a), (b), and (c), respectively.

**Table S7.** Parameterization of photovoltage trend from the EC modelling following Equations (S1), (S2), (S3) and from the IS spectra of the sample **HI** in SC.

Parameters	$R_s$	$R_{hf}$	$R_{mf}$	$R_{lf}$	$C_{hf}$	$C_{lf}$	$\tau_{hf}$	$\tau_{lf}$
$R_s$ ( $\Omega \text{ cm}^2$ )	1.38	—	—	—	—	—	—	—
$R_{sh}$ ( $\Omega \text{ cm}^2$ )	—	17342	11412	8.19E6	—	—	—	—
$J_\sigma$ ( $\text{A cm}^{-2}$ )	—	2.82E-6	1E-4	1.84E-5	—	—	1.5E-5	1.04E-5
$C_0$ ( $\text{F cm}^{-2}$ )	—	—	—	—	9.64E-8	7E-8	—	—
$f_e$ ( $\text{A cm}^{-2}$ )	—	—	—	—	—	1.09E-5	—	1.13E-4
p (a.u.)	—	—	—	—	—	1.00	—	1.86
$\tau_0$ (s)	—	—	—	—	—	1.00	—	0.0586
$V_{ph}$ (V)	—	—	—	—	—	—	—	—
$J_V$ ( $\text{A cm}^{-2}$ )	—	—	—	—	—	—	—	—

## S4. Stability test in short-circuit under 0.2 sun white LED equivalent illumination intensity

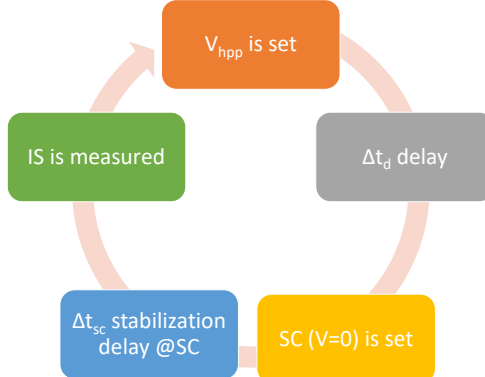


**Figure S16.** Scheme of the degradation test loop. The devices were initially set under illumination to a high-power point ( $V_{hpp}$ ), close to that of the starting maximum-power point (MPP) without correcting hysteresis effect. Next, a delay time ( $\Delta t_d$ ) for degradation was waited while the illumination and the bias  $V_{hpp}$  were constant. Subsequently a biasing change from near-to-MPP to short-circuit ( $V=0V$ ) is set. Another delay time ( $\Delta t_{sc}$ ) is considered allowing the short circuit current to stabilize. Afterwards, the impedance spectrum (IS) is measured at short-circuit (SC). The loop is repeated when a new  $V_{hpp}$  is set. For the correction of the  $V_{hpp}$  value, an empirical rule was implemented. Provided the initial difference  $\Delta V = V_{oc,0} - V_{mpp}$  between the open circuit voltage and the MPP voltage, the open circuit voltage of the  $n^{\text{th}}$  cycle is measure after the IS and then the  $n^{\text{th}}$  high-power voltage value is set as:  $V_{hpp,n} = V_{oc,n-1} - \Delta V$

### S4.1. High power condition over time

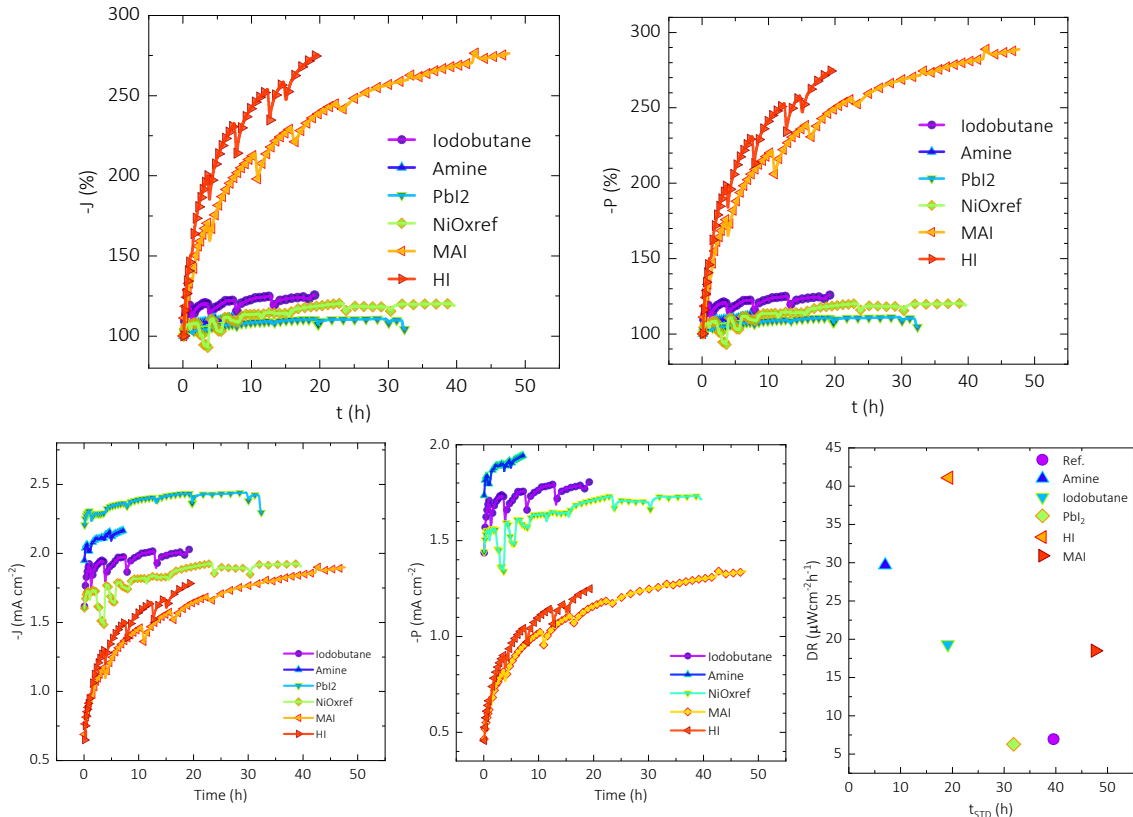


**Figure S17.** Stability test at high power point under 0.2 sun white LED equivalent illumination.

## S4.2. Impedance spectroscopy in short-circuit over time

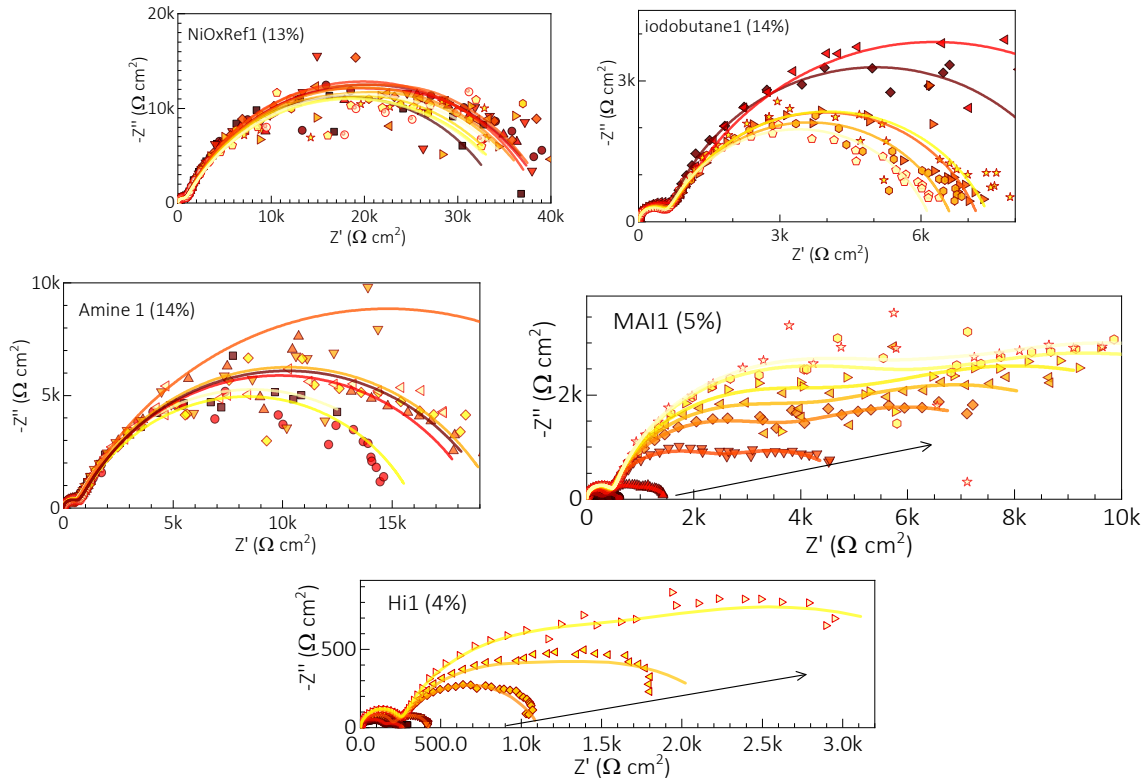


**Figure S18.** Impedance spectra in Nyquist plot representation in short-circuit under 0.2 sun white LED equivalent over time for different sample surface treatment, as indicated. Dots and lines are the experimental data and equivalent circuit model fittings, respectively. The lighter (yellower) the colours the longer the time. The same spectra are shown in **Figure S20** and **Figure S19**

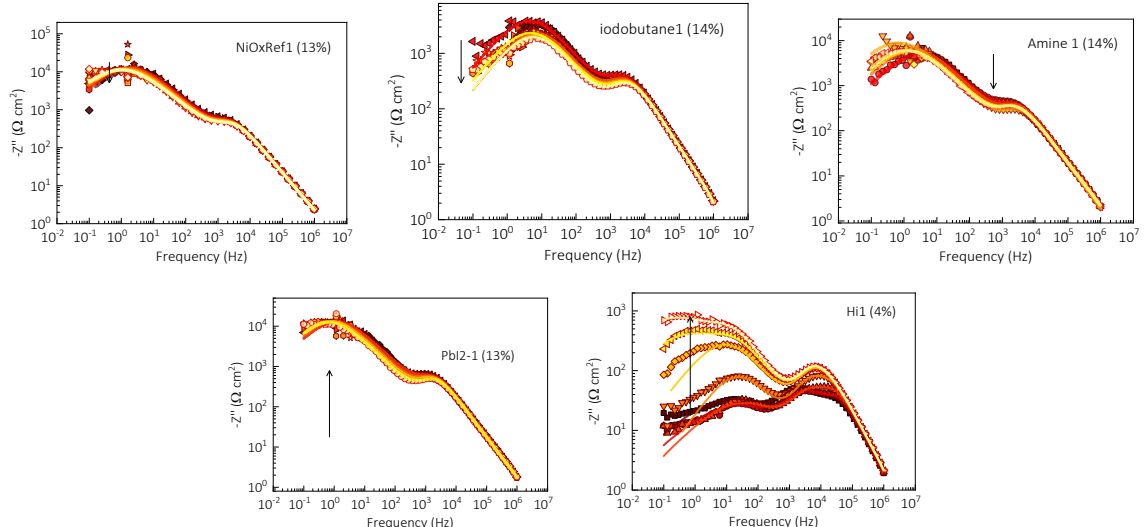


**Figure S19.** Bode plots of imaginary part of impedance spectra over time in short-circuit condition under 0.2 sun white LED equivalent illumination. The dots are the experimental data and lines are the fittings to equivalent circuit models. The same spectra are shown in **Figure S18** and **Figure S20**.

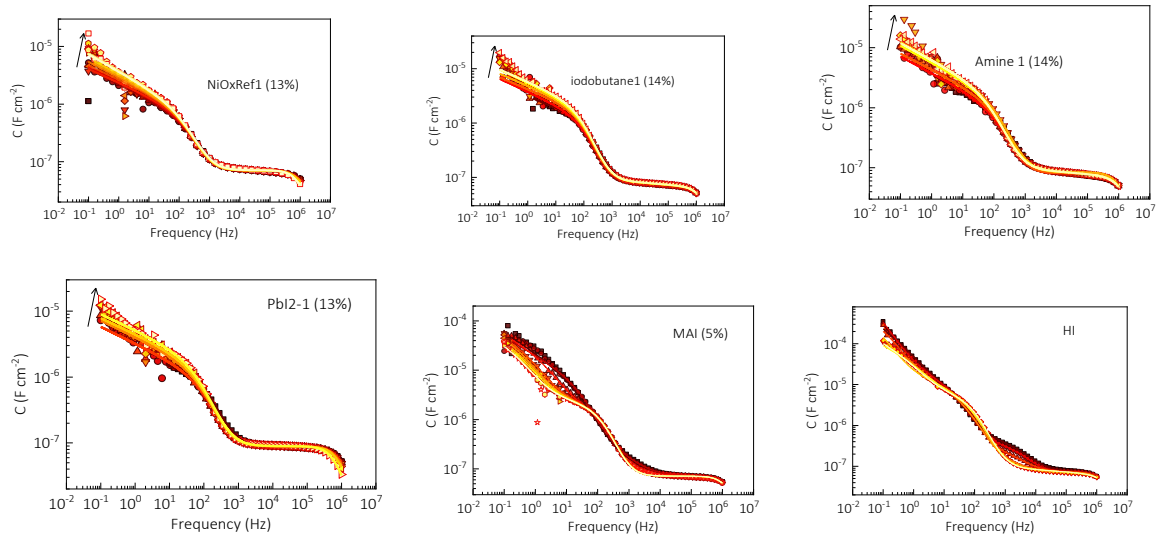


**Figure S20.** Bode plots of capacitance spectra over time in short-circuit condition under 0.2 sun white LED equivalent illumination for different sample surface treatment, as indicated. The dots are the experimental data and lines are the fittings to equivalent circuit models. The same spectra are shown in **Figure S18** and **Figure S19**

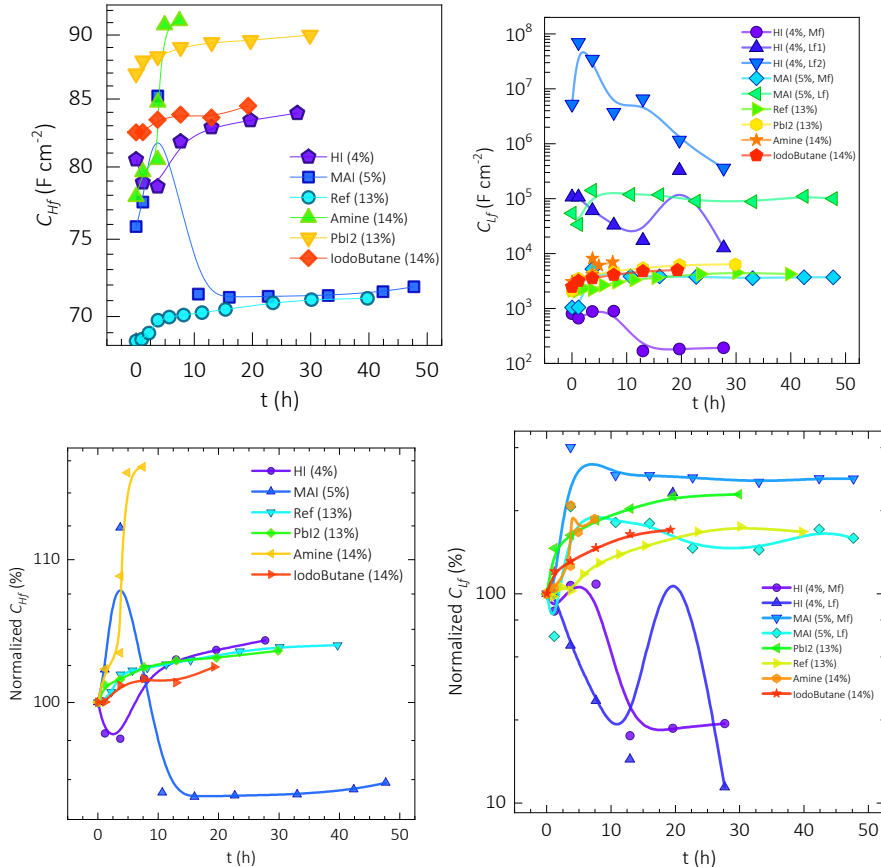


**Figure S21.** Capacitance evolution over time during the stability test in short-circuit condition under 0.2 sun white LED equivalent illumination. The values are the result of numerical fittings of the spectra in **Figure S20** to equivalent circuit models.

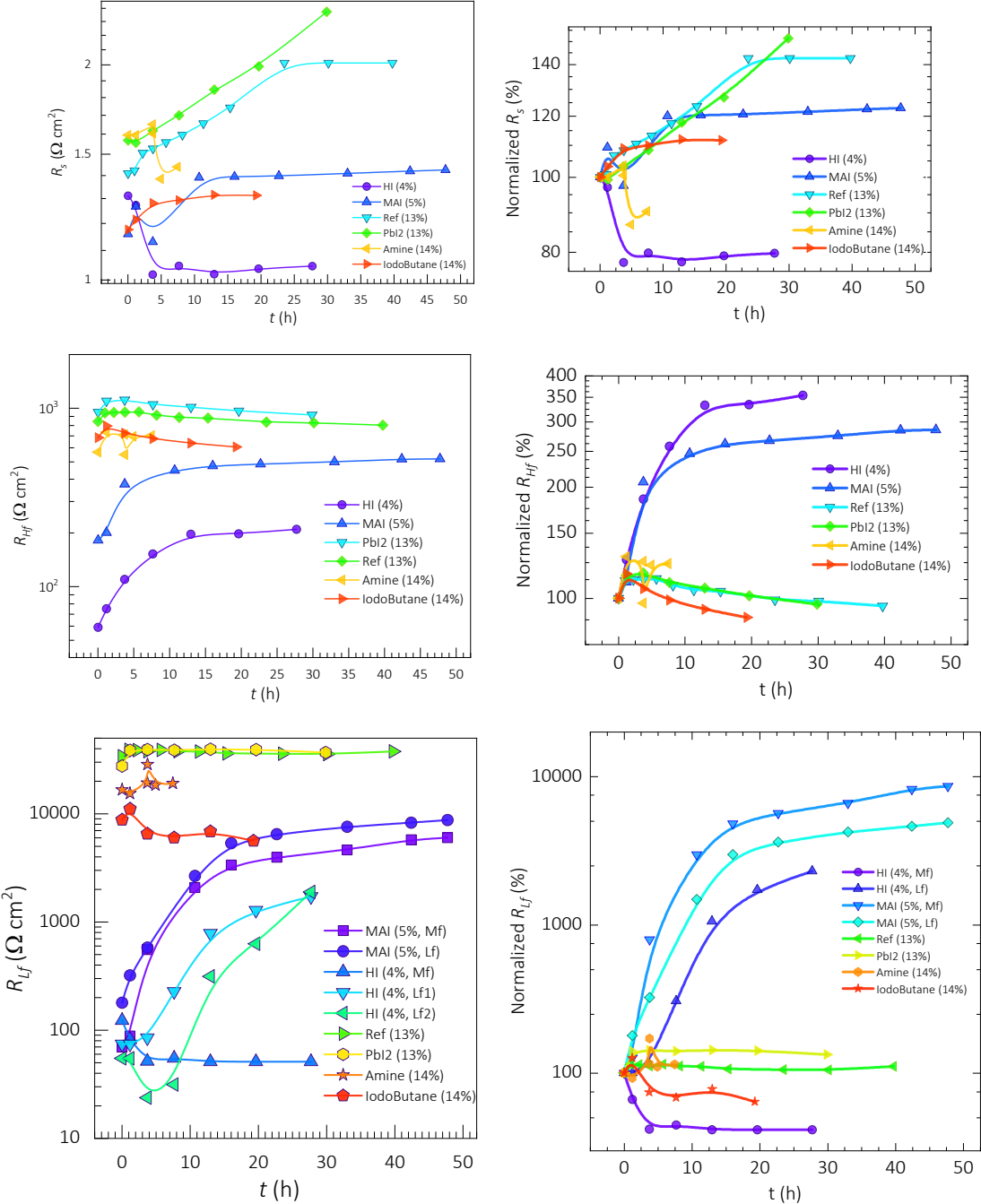


**Figure S22.** Resistance evolution over time during the stability test in short-circuit condition under 0.2 sun white LED equivalent illumination for different samples, as indicated. The values are the result of numerical fittings of the spectra in **Figure S18** to equivalent circuit models.

## S5. SEFTOS-FLUXIM<sup>[1]</sup> simulations

**Table S8.** Simulation parameters for Setfos-Fluxim

Parameter	Value			Unit
	Active layer (perovskite)	Hole conductor (NiOx)	Electron conductor (C <sub>60</sub> )	
Dielectric constant	24.1	3	3.9	
Thickness	400	30	30	nm
Bimolecular recombination pre-factor	9.40E-10	-	-	cm <sup>3</sup> /s
Langevin efficiency	3.25E-04	-	-	
Trap density	1.00E+16	-	-	cm <sup>3</sup>
Electron/hole pseudo-lifetime	5.00E-09	-	-	s
Electron/ hole capture rates	2.00E-08	-	-	cm <sup>3</sup> /s
Electron/hole Diffusion coefficient	5.00E-05	-	-	m <sup>2</sup> /s
Electron mobility	1.92E+01	-	8.90E-04	cm <sup>2</sup> /sV
Hole mobility	1.92E+01	1.00E-03	-	cm <sup>2</sup> /sV
Hole Diffusion coefficient	-	2.60E-05	-	cm <sup>2</sup> /s
Electron Diffusion coefficient	-	2.31E-05	-	cm <sup>2</sup> /s
Acceptor doping density	-	1.40E+20	-	cm <sup>-3</sup>
Donor doping density	-	-	1.50E+18	cm <sup>-3</sup>
External parameters				
Shunt resistance	1E6			Ω cm <sup>2</sup>

### S5.1. Qualitative initial simulation of current-voltage and impedance spectroscopy spectra

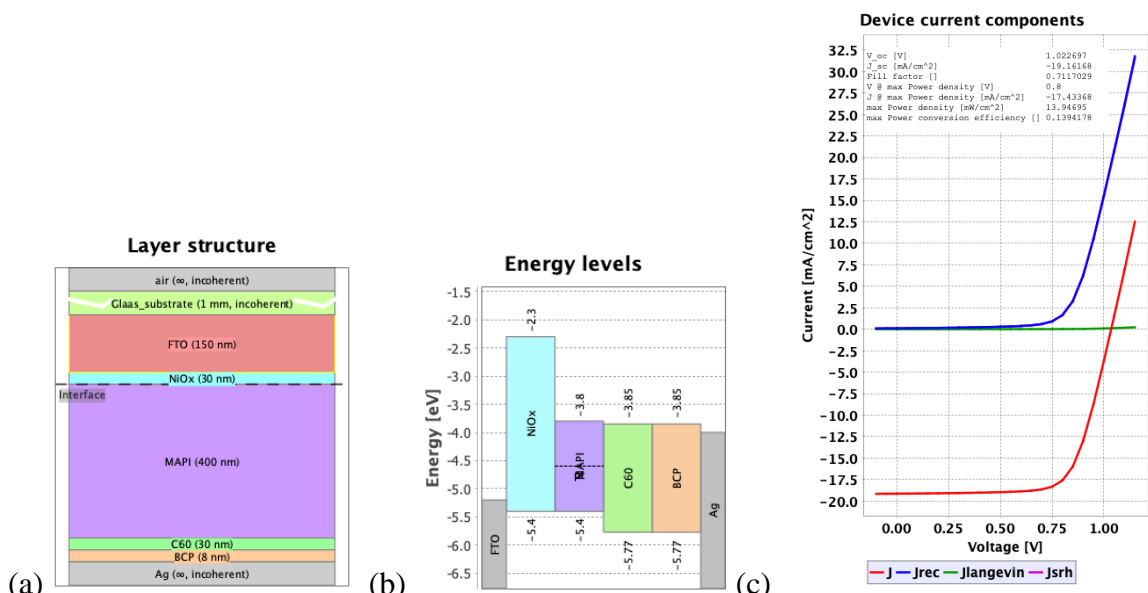


**Figure S23.** Initial settings for Setfos simulator: (a) layer structure, (b) energy diagrams and (c) base simulated current density-voltage curves in dark and under illumination.

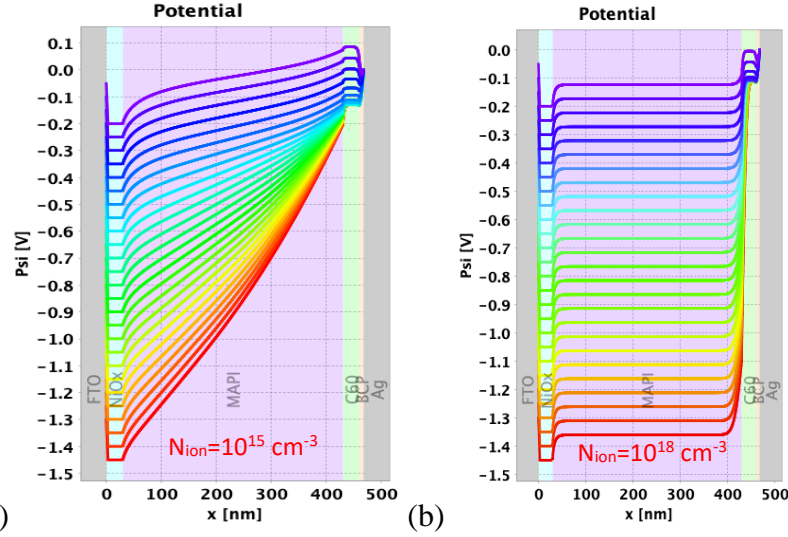


**Figure S24.** Simulated electrical potential ( $\Psi$ ) as a function of the distance ( $x$ ) between electrodes over the external voltage for mobile ion concentrations of (a)  $10^{15} \text{ cm}^{-3}$  and (b)  $10^{18} \text{ cm}^{-3}$ . The simulation parameters are in **Table S8**.

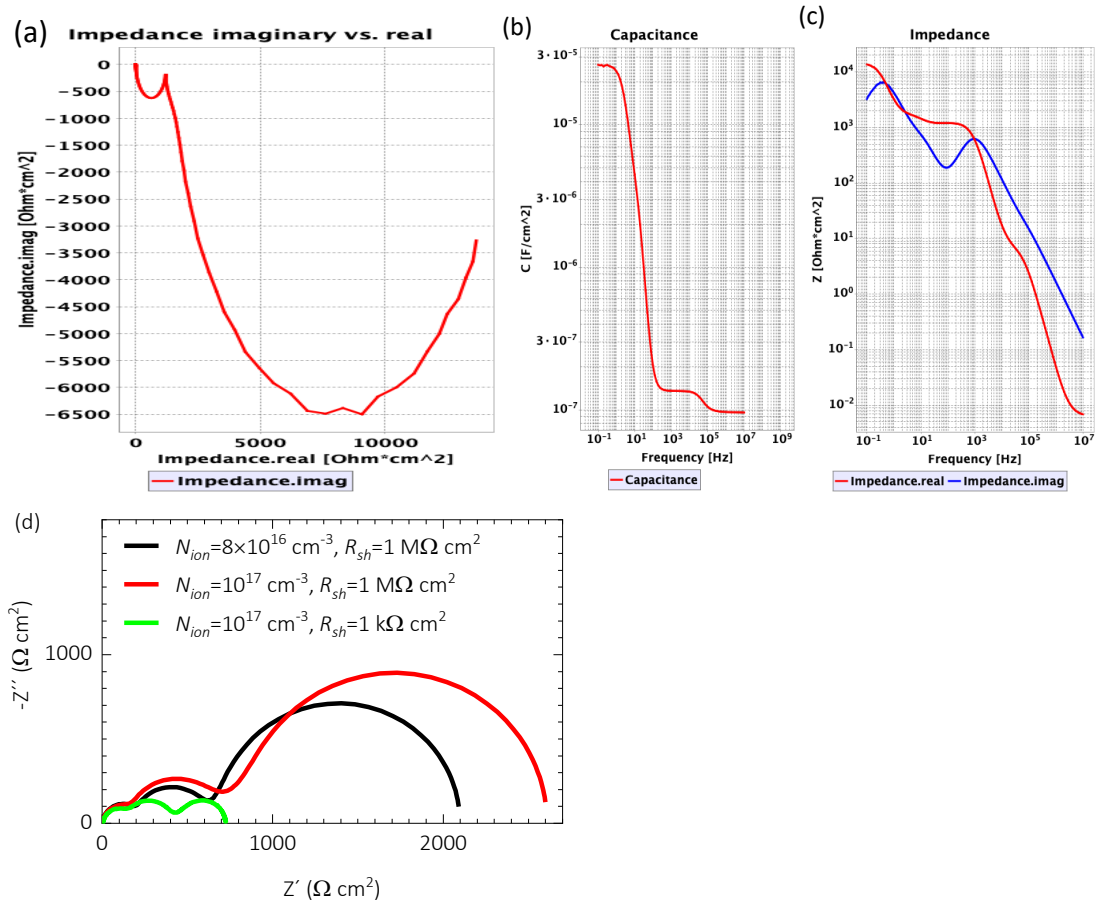


**Figure S25.** Simulated impedance spectra in short-circuit under 0.2 sun illumination intensity with  $N_{ion}=10^{18} \text{ cm}^{-3}$  in (a) impedance Nyquist plot, (b) capacitance Bode plot and (c) impedance Bode plots. In (d),  $\mu_a=10^{-5} \text{ cm}^2/\text{Vs}$  and  $\mu_c=10^{-7} \text{ cm}^2/\text{Vs}$ , and interface recombination velocities were  $10^6 \text{ cm} \cdot \text{s}^{-1}$  for electrons and  $10^7 \text{ cm} \cdot \text{s}^{-1}$  for holes. Further simulation parameters are in **Table S8**.

## S5.2. Incident illumination intensity effects

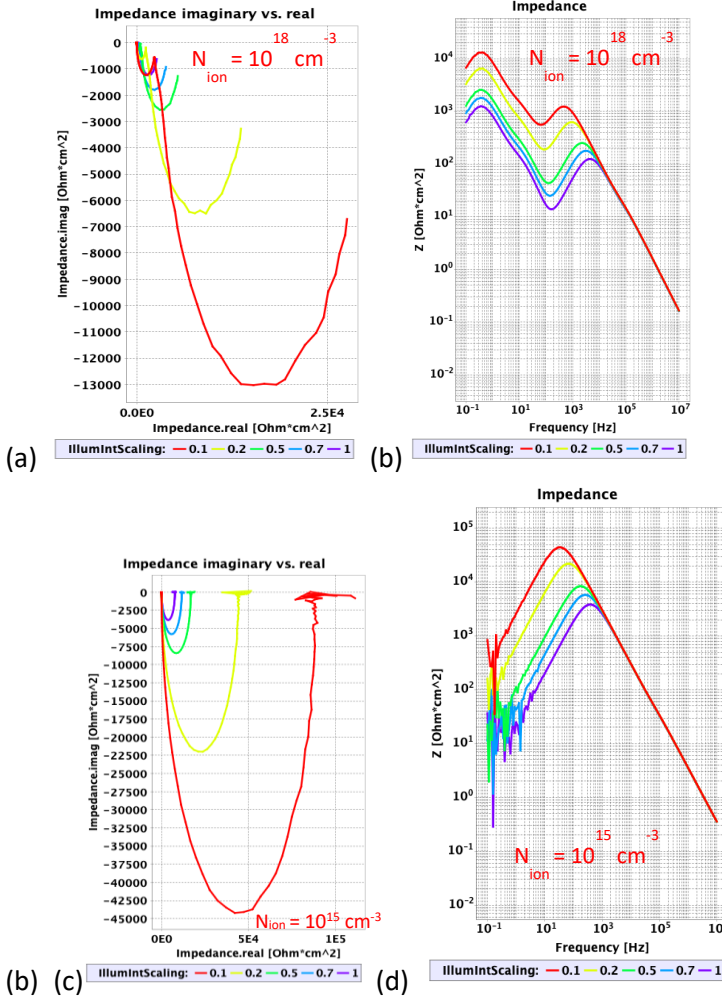


**Figure S26.** Simulated impedance spectra in short-circuit under different illumination intensities (in units of sun) with mobile ion concentrations of (a, b)  $10^{18} \text{ cm}^{-3}$  and (c, d)  $10^{15} \text{ cm}^{-3}$  in (a, c) impedance Nyquist plot, and (b, d) imaginary part of impedance Bode plot. Further simulation parameters are in **Table S8**.

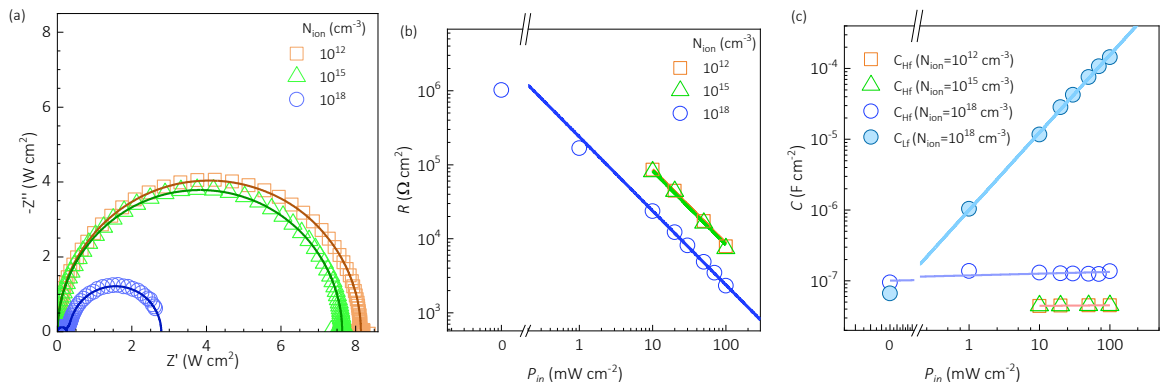


**Figure S27.** Numerical simulation of impedance spectra from the reference sample in short-circuit under different illumination intensities and for different mobile ion concentrations. In (a) there are the Nyquist plots for 1 sun illumination intensity and (b) and (c) show the resultant low frequency resistances and capacitances, respectively, from equivalent circuit modeling. The dots in (a) are Setfos-Fluxim simulations and the lines are Zview equivalent circuit fittings. The solid lines in (b) and (c) are allometric fittings with power -1 and +1, respectively.

### S5.3. Shunt resistance effects

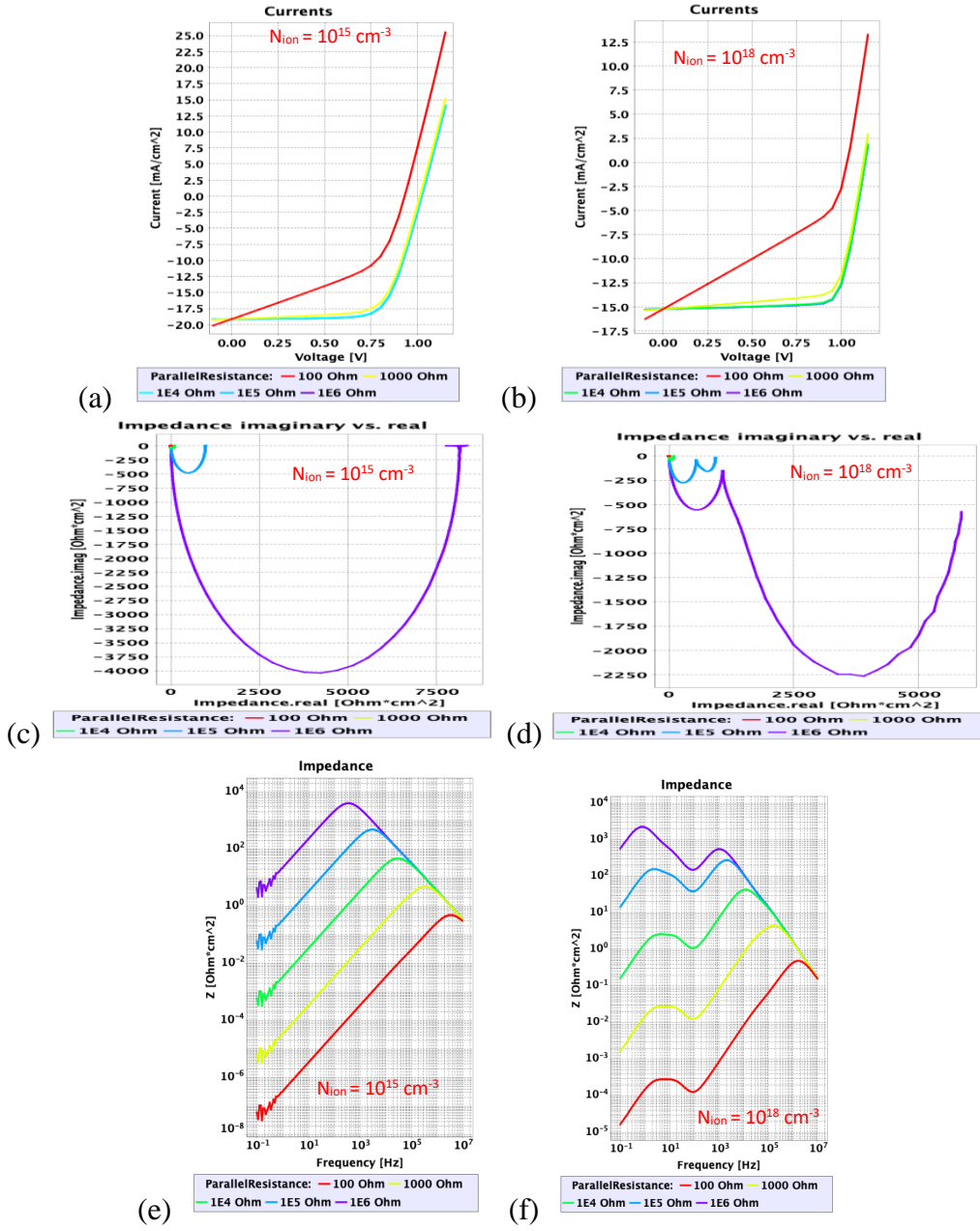


**Figure S28.** Simulated (a, b) current-voltage curves and (c-f) impedance spectra in short-circuit condition under 0.2 sun illumination intensity for different values of shunt resistance, as indicated with mobile ion concentrations of (a, c, e)  $10^{15} \text{ cm}^{-3}$  and (b, d, f)  $10^{18} \text{ cm}^{-3}$  in (c, d) impedance Nyquist plot, and (e, f) impedance imaginary part Bode plots. Further simulation parameters are in **Table S8**.

## S5.4. Interfacial recombination effect

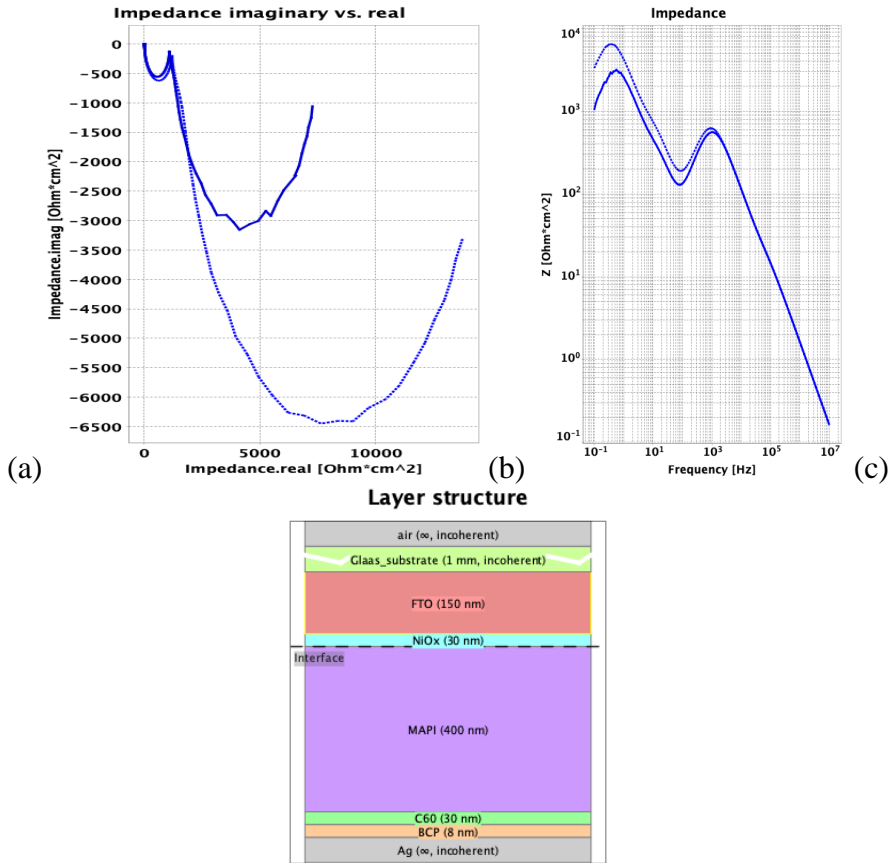


**Figure S29.** Simulated impedance spectra in short-circuit under 0.2 sun illumination for a mobile ion concentration of  $10^{18} \text{ cm}^{-3}$  with an interface (c) recombination velocity of  $10^5 \text{ cm/s}$  (solid line) and without interface recombination (dashed line). The results are shown in (a) impedance Nyquist plot, and (b) impedance imaginary part Bode plots. The simulation parameters are in **Table S8**.

## S5.5. Ion mobility effects

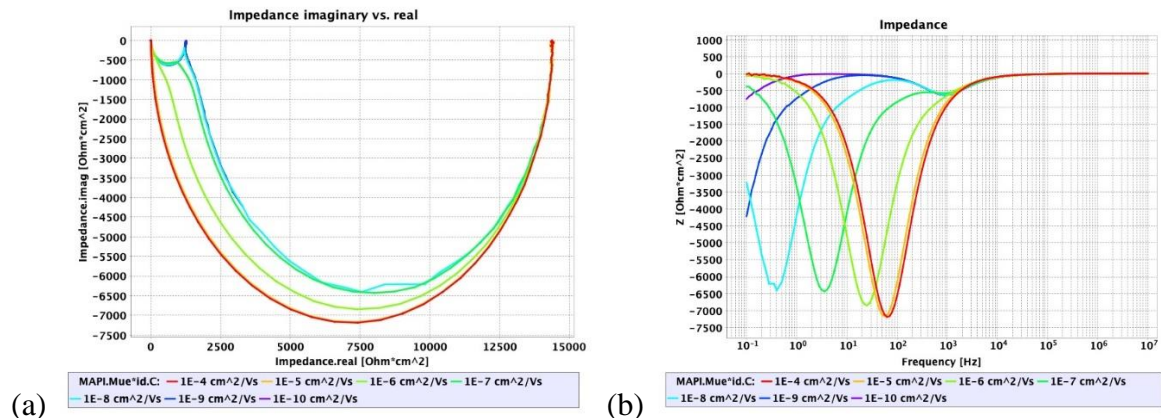


**Figure S30.** Simulated impedance spectra in short-circuit under 0.2 sun illumination for a mobile ion concentration of  $10^{18} \text{ cm}^{-3}$  with mobile ion mobility of  $10^{-8} \text{ cm/s}$  (solid line) and  $10^{-10} \text{ cm/s}$  (dashed line). The results are shown in (a) impedance Nyquist plot, and (b) impedance imaginary part Bode plots. The simulation parameters are in **Table S8**.

### S5.7. HTL ( $\text{NiO}_x$ ) doping effect

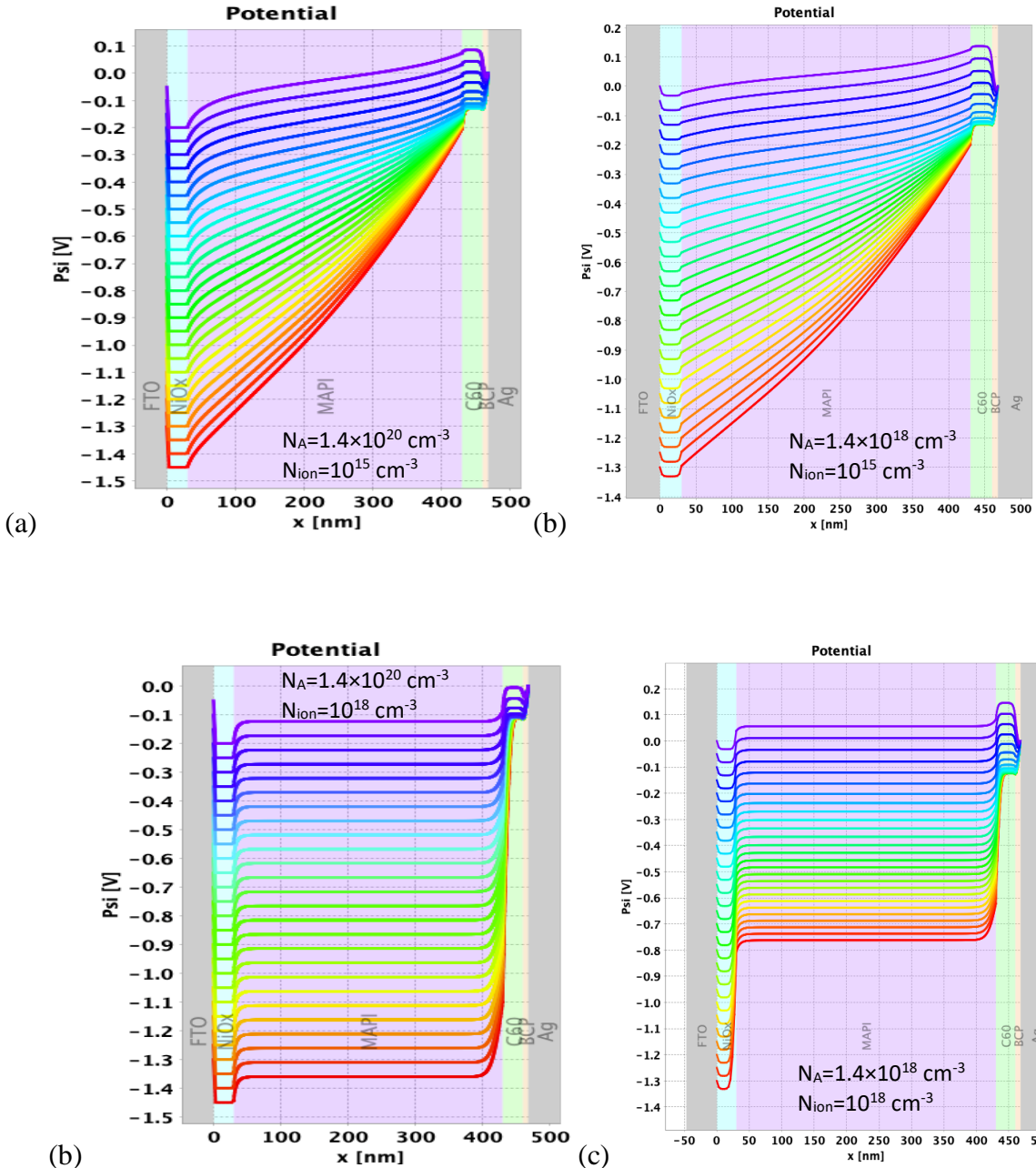


**Figure S31.** Simulated electrostatic potential as a function of external voltage for different acceptor concentrations at the hole transport layer (HTL), i.e. the  $\text{NiO}_x$ , with (a)  $N_A = 1.4 \times 10^{20} \text{ cm}^{-3}$  and  $N_{\text{ion}} = 10^{15} \text{ cm}^{-3}$ , (b)  $N_A = 1.4 \times 10^{18} \text{ cm}^{-3}$  and  $N_{\text{ion}} = 10^{15} \text{ cm}^{-3}$ , (c)  $N_A = 1.4 \times 10^{20} \text{ cm}^{-3}$  and  $N_{\text{ion}} = 10^{18} \text{ cm}^{-3}$  and (d)  $N_A = 1.4 \times 10^{18} \text{ cm}^{-3}$  and  $N_{\text{ion}} = 10^{18} \text{ cm}^{-3}$ . Further simulation parameters are in **Table S8**.

## S6. Matlabs's Driftfusion<sup>[2]</sup> simulations

**Table S9:** Simulation parameters used in this work for the input sheet of Driftfusion.<sup>[2]</sup>

Layer type	Contact	Layer	Interface	Active	Interface	Layer	Contact
Sack	Anode	NiOx	Interface 1	Perovskite	Interface 2	C <sub>60</sub>	Cathode
Thickness (cm)	--	2E-6	1E-6	4E-5	1E-6	3E-6	--
Electron affinity (eV)	--	-1.85		-3.8		-4.1	--
Ionization potential (eV)	--	-5.4		-5.4		-5.8	--
Work function (eV)	-5.2	-5.2		-4.6		-4.25	-4.2
Trap energy level (eV)	--	-3.65		-4.6		-4.95	--
Effective density of states at the conduction band (cm <sup>-3</sup> )	--	1E19		1E19		1E20	--
Effective density of states at the valence band (cm <sup>-3</sup> )	--	1E19		1E19		1E20	--
Equilibrium concentration of cations (cm <sup>-3</sup> )	--	0	0	1E16	0	0	--
Equilibrium concentration of anions (cm <sup>-3</sup> )	--	0	0	1E16	0	0	--
Maximum concentration of cations (cm <sup>-3</sup> )	--	0	0	1.21E22	0	0	--
Maximum concentration of anions (cm <sup>-3</sup> )	--	0	0	1.21E22	0	0	--
Charge carrier mobility of electrons (cm <sup>2</sup> V <sup>-1</sup> s <sup>-1</sup> )	--	0.001		2		0.001	--
Charge carrier mobility of holes (cm <sup>2</sup> V <sup>-1</sup> s <sup>-1</sup> )	--	0.001		2		0.001	--
Charge carrier mobility of cations (cm <sup>2</sup> V <sup>-1</sup> s <sup>-1</sup> )	--	0	0	1E-8	0	0	--
Charge carrier mobility of anions (cm <sup>2</sup> V <sup>-1</sup> s <sup>-1</sup> )	--	0	0	1E-10	0	0	--
Dielectric constant	--	3		64		3	--
Generation rate (s <sup>-1</sup> cm <sup>-3</sup> )	--	0	0	2e21 (1 sun)	0	0	--
Band-to-band radiative recombination rate (s <sup>-1</sup> cm <sup>3</sup> )	--	6.3E-11	0	4.8E-11	0	6.8E-11	--
Shockley-Read-Hall non-radiative recombination lifetime for electrons (s)	--	1E-6	1E-10	0.8E-7	1E-10	1E-6	--
Shockley-Read-Hall non-radiative recombination lifetime for holes (s)	--	1E-6	1E-10	0.8E-7	1E-10	1E-6	--
Recombination velocity for electrons (cm·s <sup>-1</sup> )	1E7	--		--		--	1E7
Recombination velocity for holes (cm·s <sup>-1</sup> )	1E7	--		--		--	1E7
Shunt Resistance (Ωcm <sup>2</sup> )					1E6		

### S6.1. Qualitative initial simulation of J-V curve and IS spectra

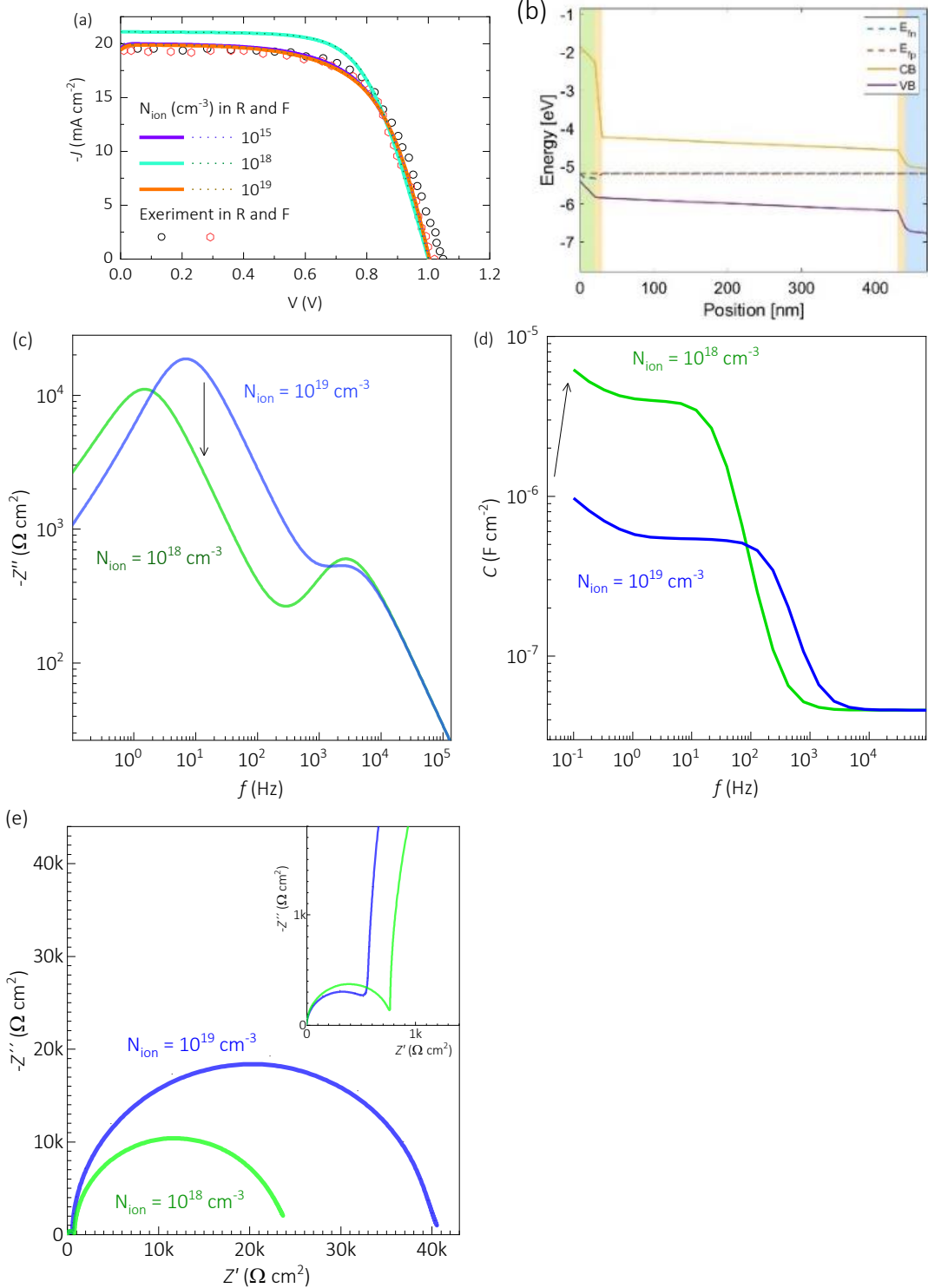


**Figure S32.** (a) Experimental J-V curve of the ref. structure (dots) and the numerical simulations (lines) considering different  $N_{ion}$  and voltage sweep directions. (b) Energy band diagram of the simulated structure:  $\text{NiO}_x/\text{perovskite}/\text{C}_{60}$  considering  $N_{ion}=10^{15}$  cm<sup>-3</sup>, 0.2 sun illumination, and short-circuit condition. The simulated IS spectra are shown the Bode plots of (c) imaginary part of impedance and (d) capacitance and the (e) impedance Nyquist plot. The simulation parameters for the J-V curve include  $V_{bi}=1\text{V}$ ,  $G=33\times 10^{20}\text{ cm}^{-3}\text{s}^{-1}$ ,  $R_{sh}=1\text{ M}\Omega\cdot\text{cm}^2$ , in addition to those parameters in **Table S9**.

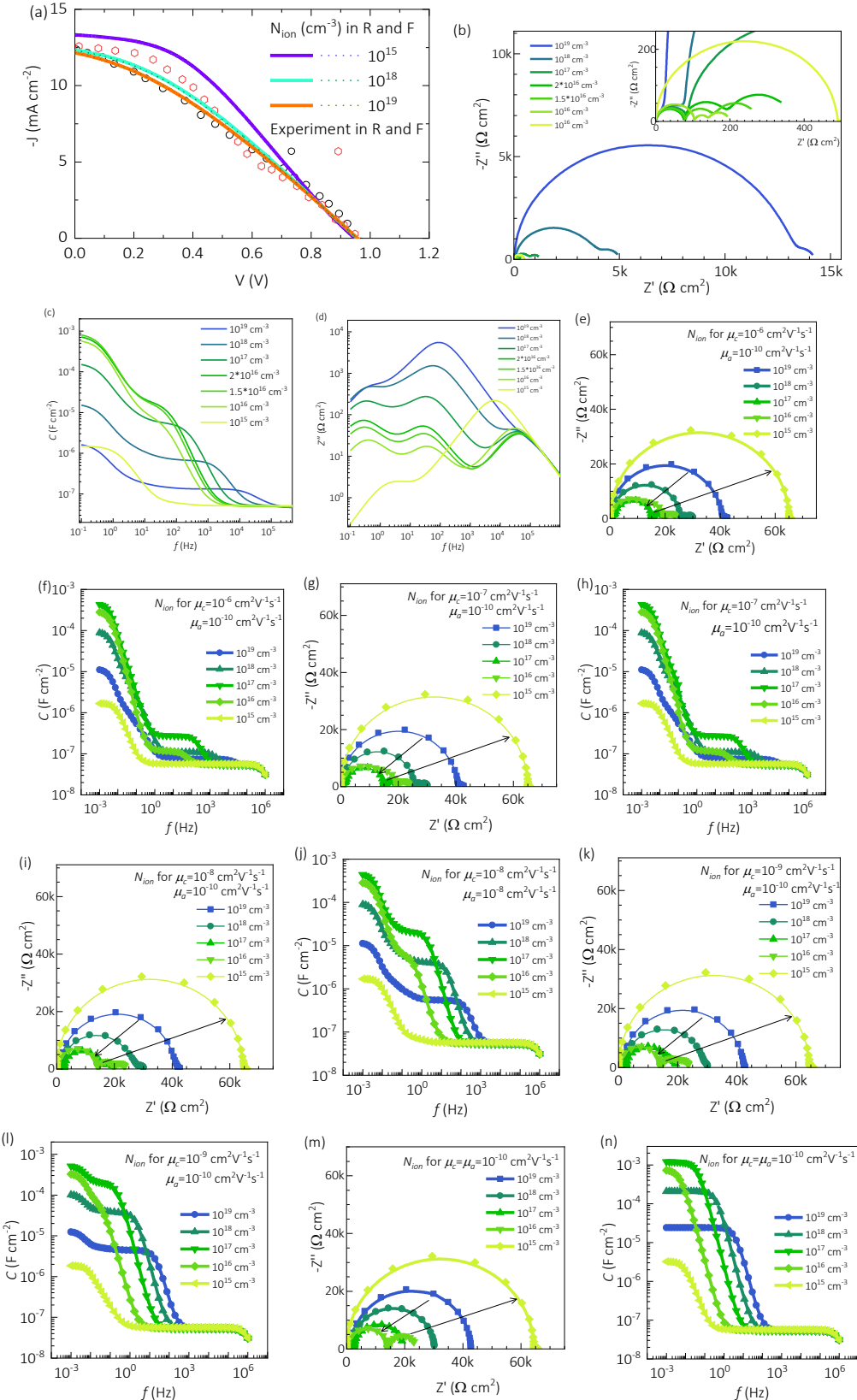


**Figure S33.** Simulations for the MAI and HI samples. The J-V curves in (a) compare the experimental data of (dots) and the numerical simulations (lines) for different ion concentrations and voltage sweep directions (solid and dashed lines for forward and backward directions). The simulated IS spectra with three arcs are shown in impedance Nyquist plot and the Bode plots of capacitance in (b-n). The simulation parameters for the current-voltage curve include scan rate of 70 mV·s<sup>-1</sup>,  $V_{bi}=1\text{V}$ ,  $\mu=10^{-4} \text{ cm}^2 \text{V}^{-1} \text{s}^{-1}$ ,  $G=4\times10^{20} \text{ cm}^{-3} \text{s}^{-1}$ ,  $R_{sh}=1 \text{ M}\Omega \cdot \text{cm}^2$ , in addition to those parameters in **Table S9**.

## S6.2. Incident illumination intensity effects

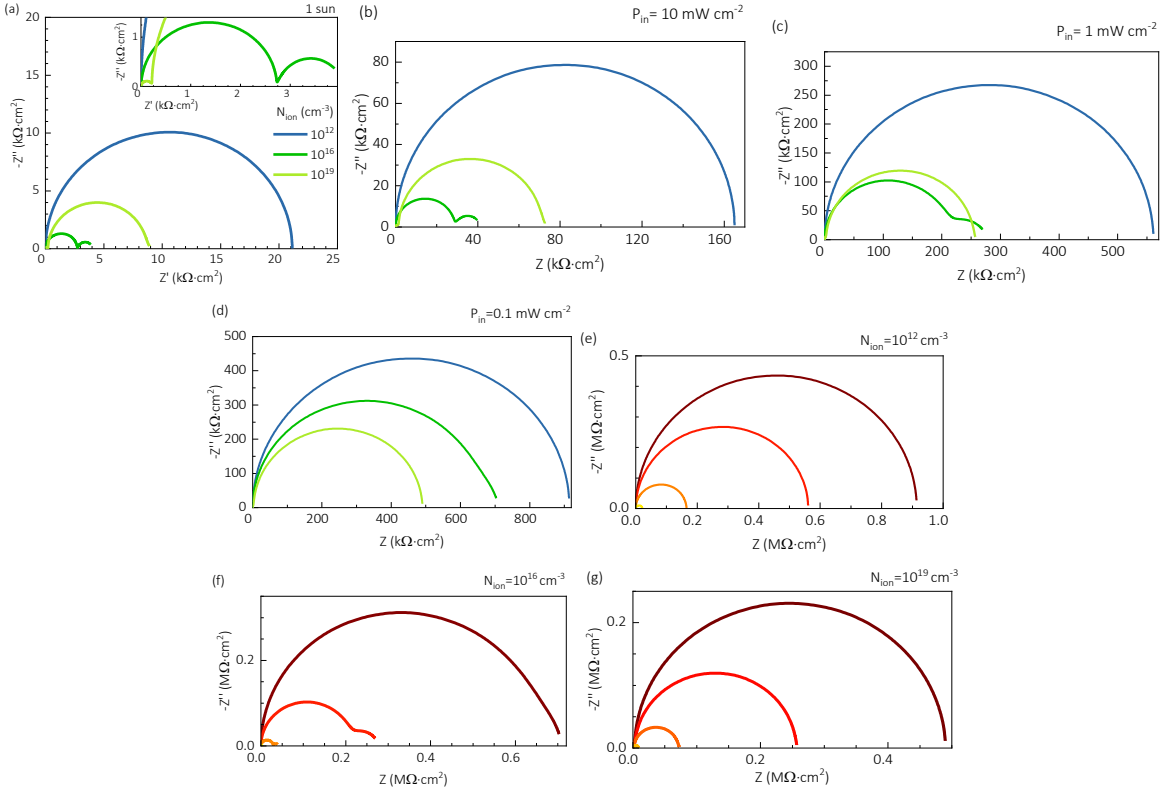


**Figure S34.** Simulated effect of the light intensity on the IS Nyquist plot. The initial generation rate  $G = 2 \cdot 10^{21} \text{ cm}^{-3}$  is reduced by a factor of 1, 0.1, 0.01, 0.001 in (a-d), respectively, for  $N_{\text{ion}} = 10^{12}$  (blue),  $10^{16}$  (green),  $10^{19}$  (lime)  $\text{cm}^{-3}$ . The same data is reordered for each ion concentration in (e-g), where darker (brown) line colours indicate lower illumination intensities. The simulated shunt resistance was  $1 \text{ M}\Omega$ .

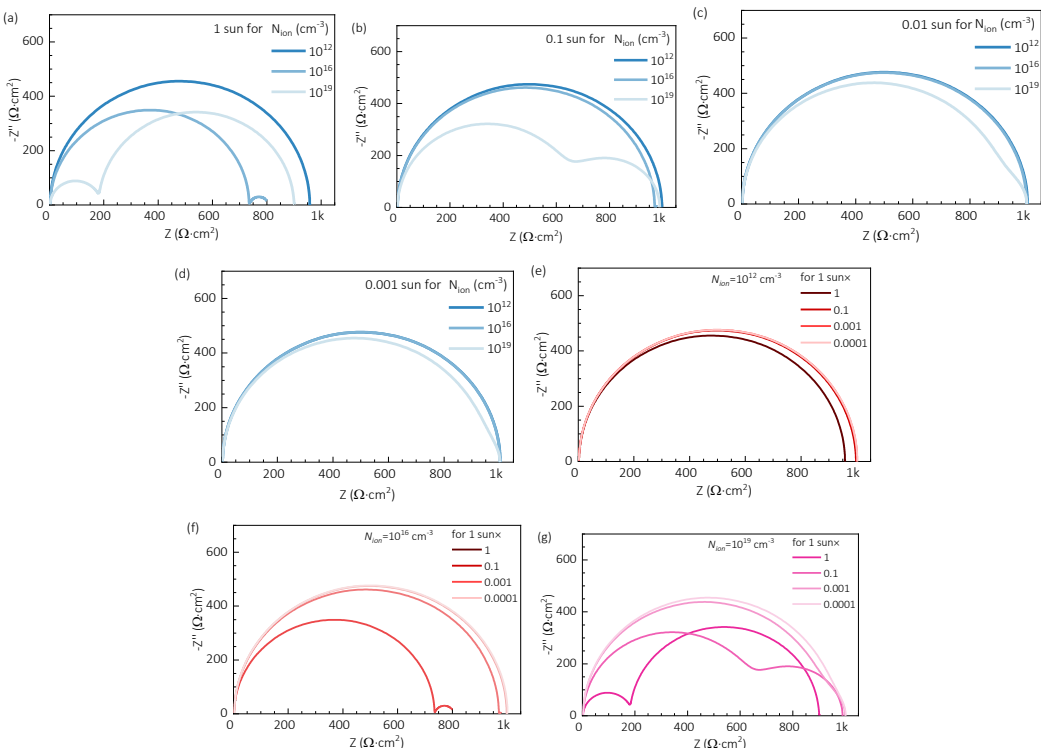


**Figure S35.** Effect of the light intensity (the initial generation rate is reduced by a factor of 1, 0.1, 0.01, 0.001) on the Nyquist plot. At lower light intensity higher is the impact of mobile ions on the total impedance of the system. The simulation parameters include shunt resistance  $R_{sh} = 1 \text{ k}\Omega$ , besides those in the Table S9.

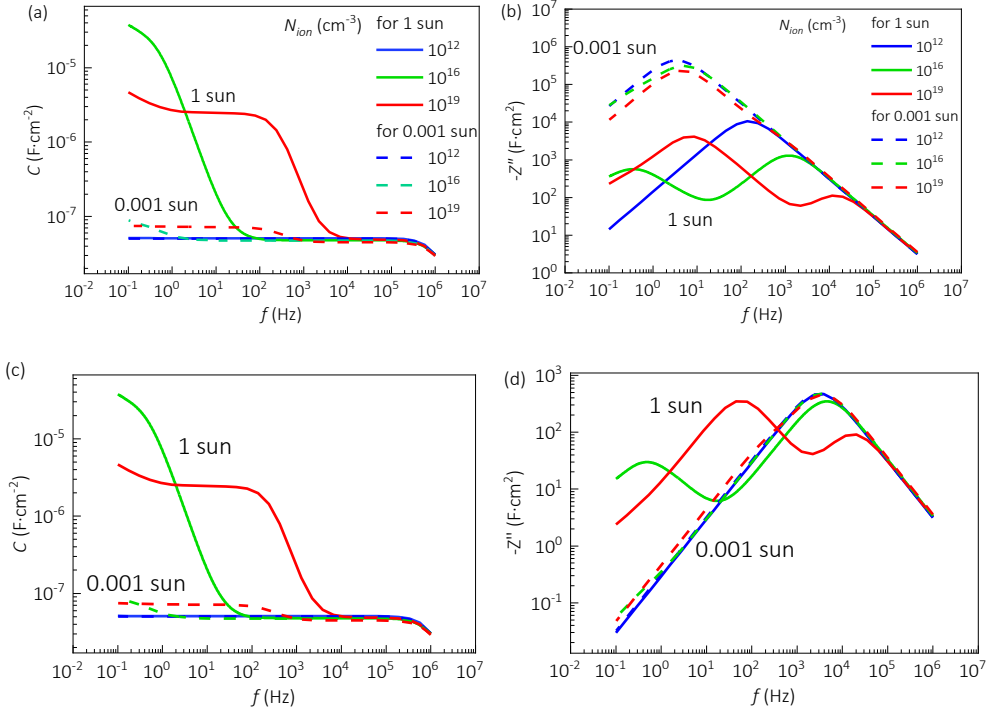


**Figure S36.** Simulated IS spectra with the effect of the light intensity (the initial generation rate is reduced by a factor of 1, 0.001) on the capacitance and imaginary-frequency plot for different values of mobile ion concentration ( $N_{ion} = 10^{12}$ (blue),  $10^{16}$ (green),  $10^{19}$ (red)  $\text{cm}^{-3}$ ) and shunt resistance (1  $\text{M}\Omega$  and 1  $\text{k}\Omega$  in top and bottom, respectively). Further simulation parameters are in Table S9.

### S6.3. Shunt resistance effect

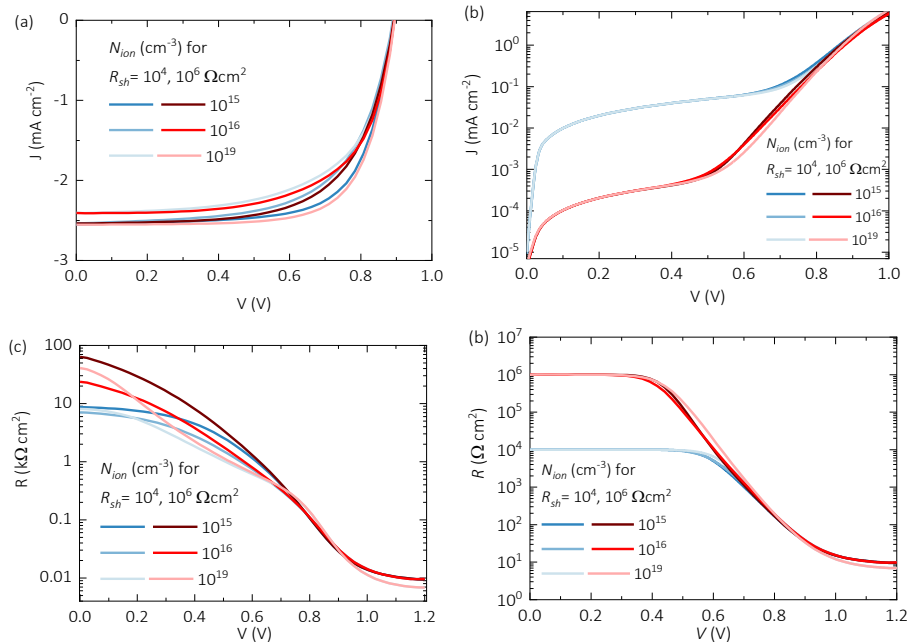


**Figure S37.** Simulated current-voltage curves (a) under 0.2 sun illumination intensity and (b) in dark, with DC resistances (in c, d, respectively) for the reference sample considering different shunt resistance and mobile ion concentrations, as indicated. The physical simulation parameters are in the **Table S9**.

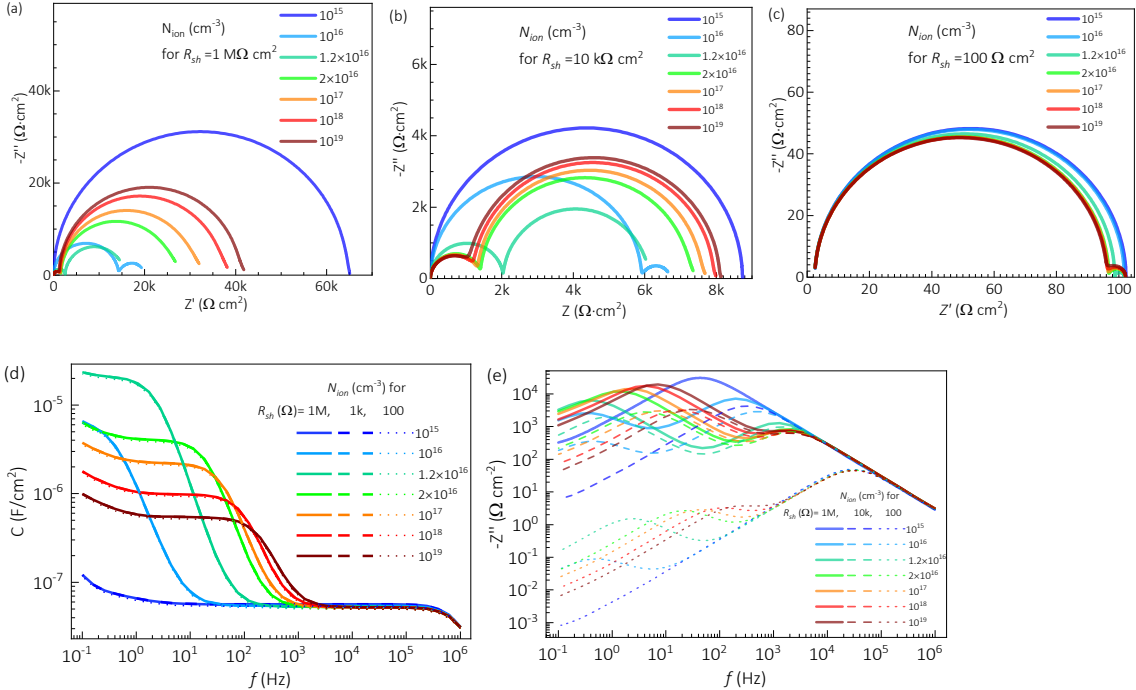


**Figure S38.** Simulated impedance spectra for the reference sample considering different shunt resistance and ion concentrations, as indicated. The physical simulation parameters are in the **Table S9**.

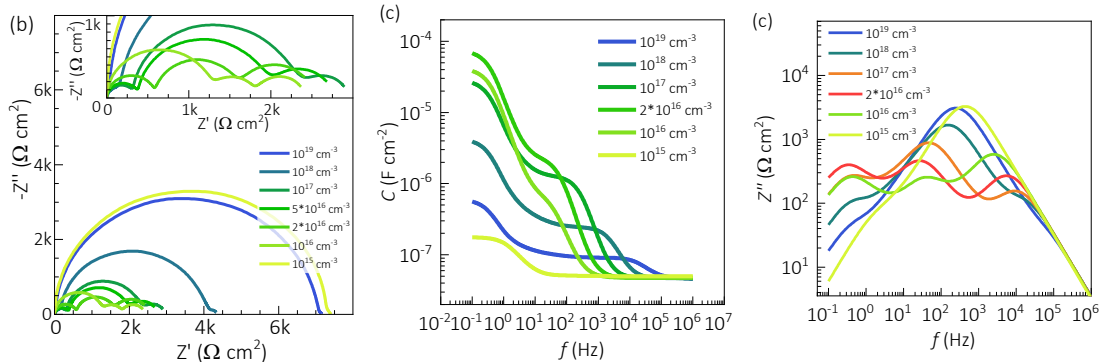


**Figure S39.** Simulated impedance spectra considering different **high shunt resistance** ( $1 \text{ M}\Omega$ ) ion concentrations in (a) impedance Nyquist representation, (b) capacitance Bode Plot and (c) imaginary part of impedance versus frequency. The physical parameters are in the **Table S9**.

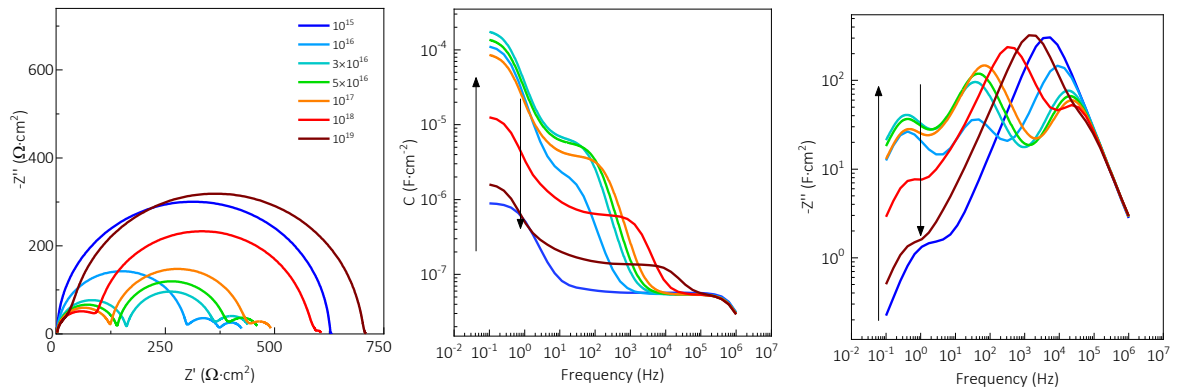


**Figure S40.** Simulated impedance spectra for the HI or MAI samples with combined effect of **low shunt resistance** ( $1 \text{ k}\Omega \text{ cm}^2$ ), positive/negative ion mobility ( $10^{-6}/10^{-8} \text{ cm}^2\text{V}^{-1}\text{s}^{-1}$ ), low electron/hole mobility ( $0.2 \text{ cm}^2\text{V}^{-1}\text{s}^{-1}$ ) and high light intensity  $G_0 = 2 \cdot 10^{21} \text{ cm}^{-3}\text{s}^{-1}$ . Simulated ion concentrations are:  $N_{ion} = 10^{15}, 10^{16}, 3 \times 10^{16}, 5 \times 10^{16}, 10^{18}, 10^{19} \text{ cm}^{-3}$ .

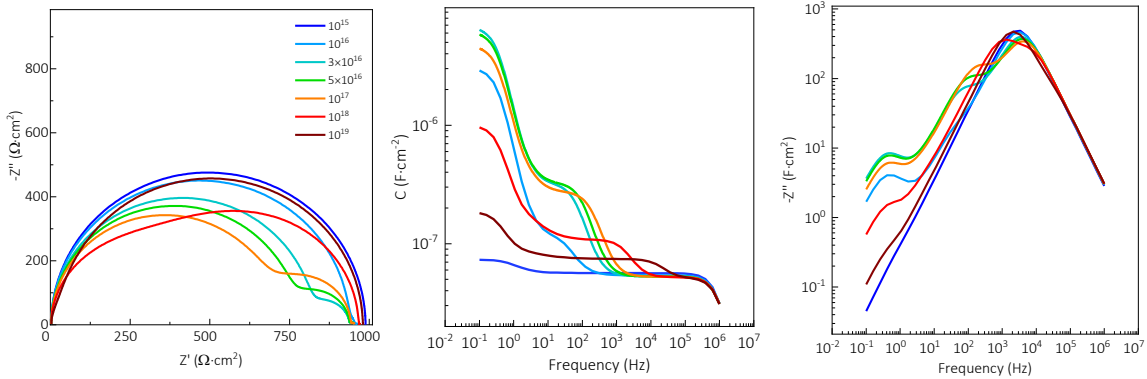


**Figure S41.** Simulated impedance spectra for the HI or MAI samples with lower generation rate than those of **Figure S40**. At low light intensity, or upon reduction of optical absorption, the lower the shunt resistance the more negligible the three-arcs effects within the explored perturbation frequency for high concentration of mobile ions and electron mobility. Low shunt resistance:  $1 \text{ k}\Omega \text{ cm}^2$ , positive/negative ion mobility:  $10^{-6}/10^{-8} \text{ cm}^2\text{V}^{-1}\text{s}^{-1}$ , electron/hole mobility  $2 \text{ cm}^2\text{V}^{-1}\text{s}^{-1}$  and low light intensity  $G_0 = 4 \cdot 10^{20} \text{ cm}^{-3}\text{s}^{-1}$ . Simulated ion concentrations are:  $N_{ion} = 10^{15}, 10^{16}, 3 \times 10^{16}, 5 \times 10^{16}, 10^{18}, 10^{19} \text{ cm}^{-3}$ .

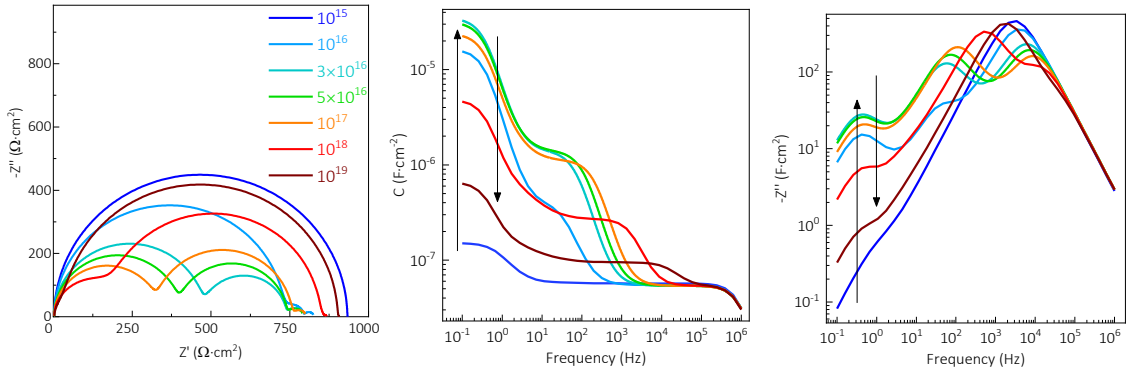


**Figure S42.** Simulated impedance spectra for the HI of MAI sample with combined effect of low shunt resistance ( $1 \text{ k}\Omega\text{cm}^2$ ), ion mobility (positive/negative ion mobility:  $10^{-6}/10^{-8} \text{ cm}^2\text{V}^{-1}\text{s}^{-1}$ ), electron/hole mobility ( $2 \text{ cm}^2\text{V}^{-1}\text{s}^{-1}$ ) and low light intensity  $G_0 = 2 \cdot 10^{21} \text{ cm}^{-3}\text{s}^{-1}$ . Simulated ion concentrations are:  $N_{ion} = 10^{15}, 10^{16}, 3 \times 10^{16}, 5 \times 10^{16}, 10^{18}, 10^{19} \text{ cm}^{-3}$ .

#### S6.4. Concentration of mobile ions ( $N_{ion}$ in the perovskite) effects

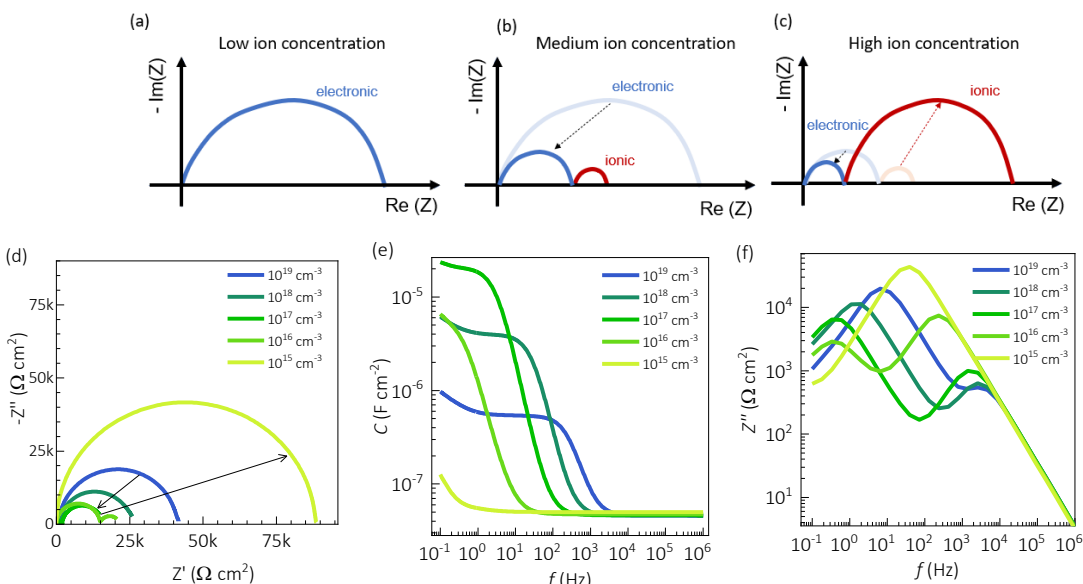


**Figure S43.** Schemed impedance spectra with effects due to different mobile ion concentrations (a-c) and corresponding numerical simulations (d-f). The plots show (d) Nyquist representation, (e) capacitance vs frequency, and (f) imaginary part of impedance vs frequency. Further simulation parameters are in **Table S9**.

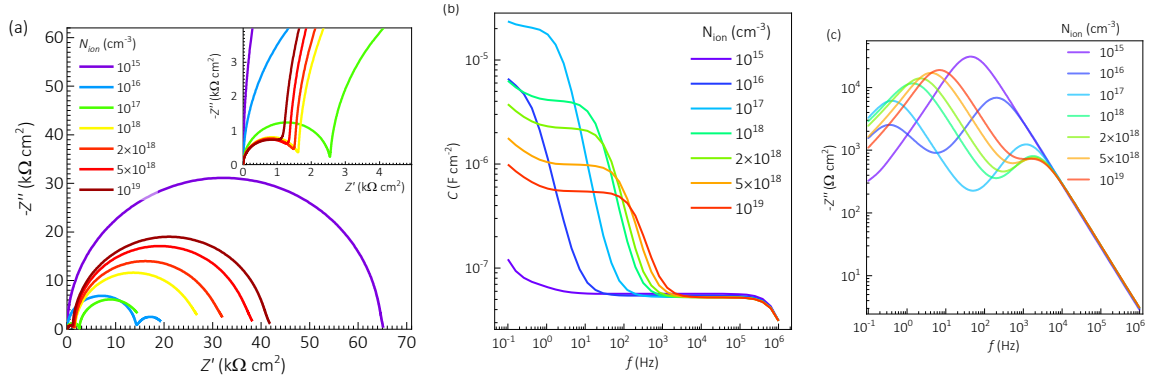


**Figure S44.** Simulated impedance spectra in (a) Nyquist plot and Bode plots of (b) capacitance and (c) imaginary part of impedance for different perovskite mobile ion concentrations, as indicated. The simulation parameters include  $R_{sh} = 10^6 \Omega \cdot \text{cm}^2$ ;  $R_s = 2.5 \Omega \cdot \text{cm}^2$ ;  $\epsilon_r=100$ ;  $G = 4 \times 10^{20} \text{ cm}^{-3}\text{s}^{-1}$ , besides those in the **Table S9**.

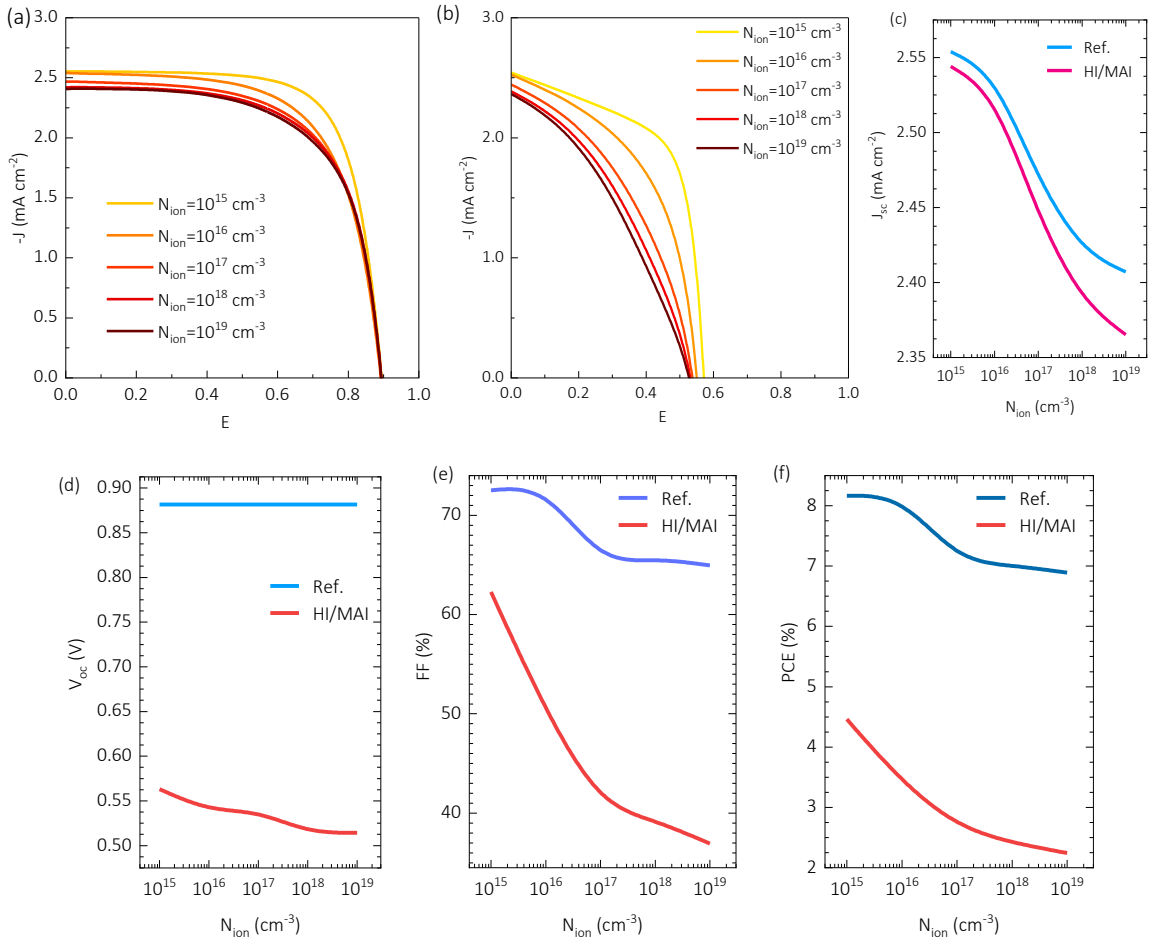


**Figure S45.** Simulated  $J$ - $V$  curves under 0.2 sun for (a) the ref. sample and (b) the HI/MAI samples considering different values of mobile ion concentration, and corresponding photocurrent (c), photovoltage (d), fill factor (e) and efficiency (f), as indicated. The simulation parameters include scan rate of 70 mV s<sup>-1</sup>, generation rate of  $4 \times 10^{20} \text{ cm}^{-3}\text{s}^{-1}$ , in addition to those values in Table S9. Notably, shunt resistance is  $R_{sh}=1 \text{ M}\Omega \cdot \text{cm}^2$  and  $1 \text{k}\Omega \cdot \text{cm}^2$ , and electron mobility is  $\mu_e=2$  and  $0.2 \text{ cm}^2\text{V}^{-1}\text{s}^{-1}$  in (a) and (b), respectively.

### S6.5. Bulk (of the perovskite) charge carrier recombination effects.

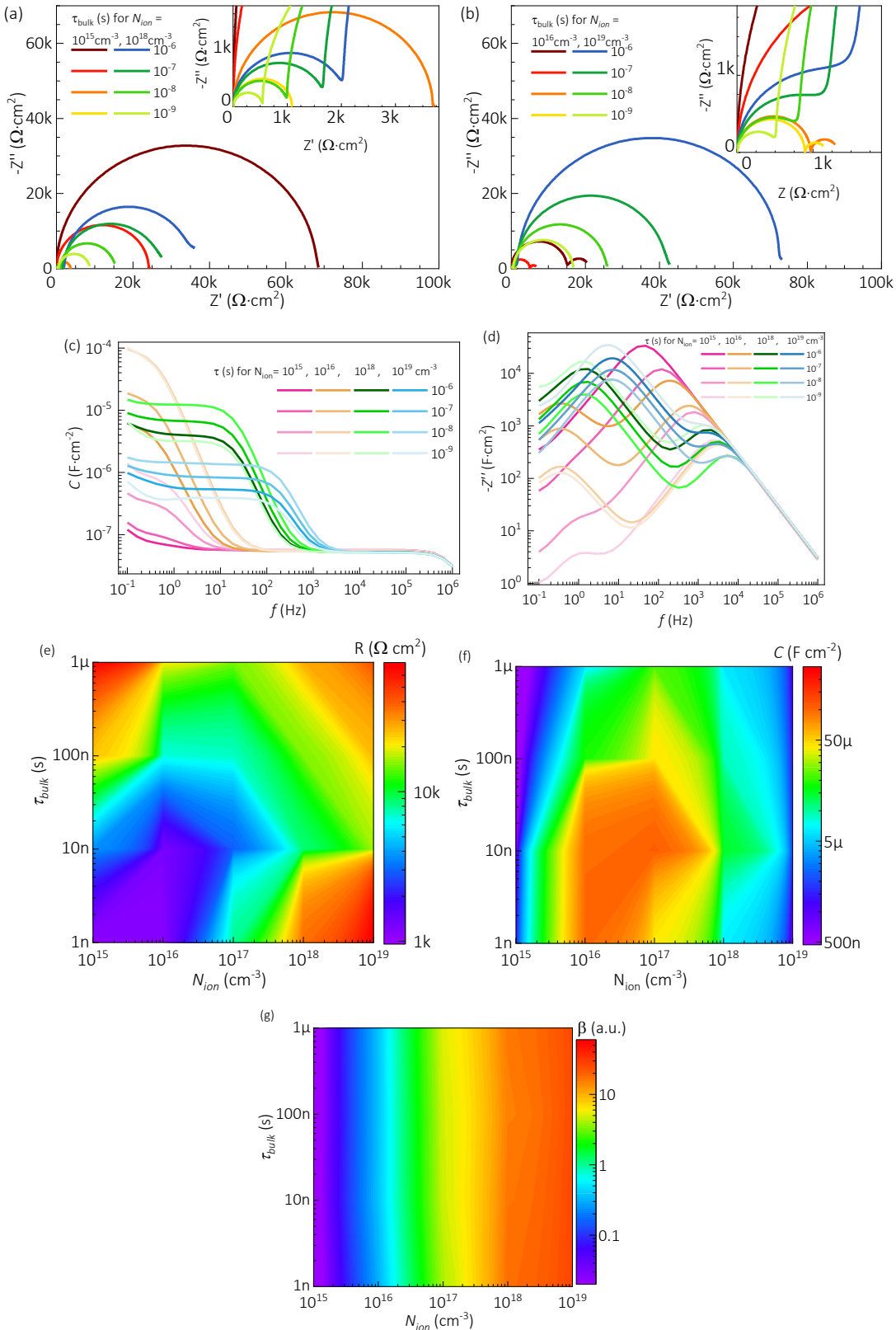


**Figure S46.** Simulated impedance spectra in short-circuit for de reference sample with different concentration of mobile ions and bulk trap recombination lifetime values, as indicated. The Nyquist plots in (a) and (b) show different values of the bulk recombination lifetime and the total resistance, capacitance and resistance frequency ratio are shown in (e, f, g), respectively. The physical simulation parameters are in the **Table S9**.

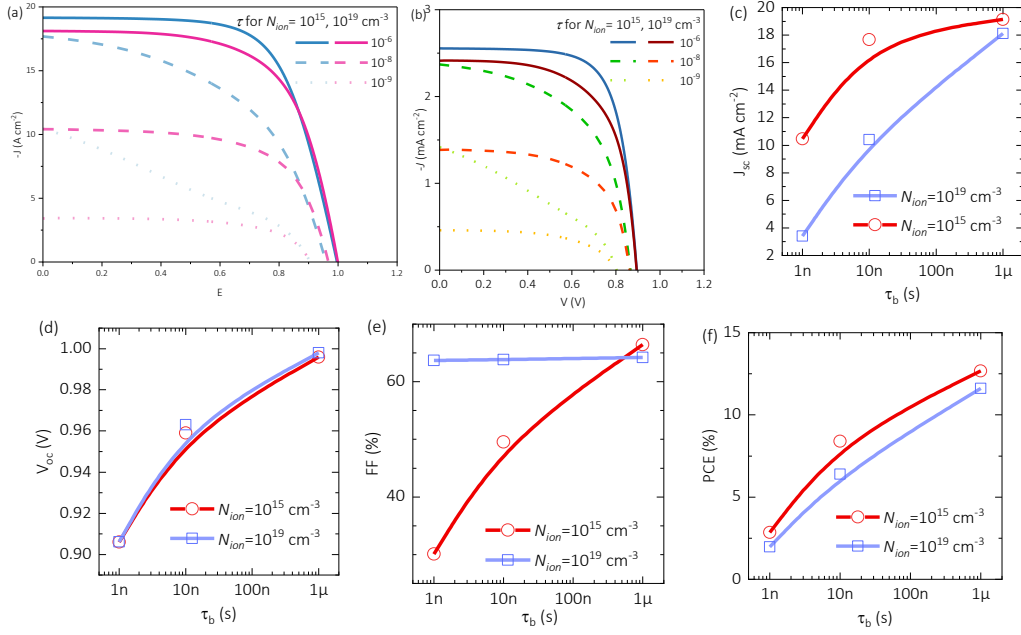


**Figure S47.** Simulated current-voltage curve under (a) 1 and (b) 0.2 sun illumination for the reference sample considering different values of mobile ion concentration and trap recombination lifetime  $\tau$  within the perovskite bulk, as indicated. The performance parameters for (a) are in (c-f). The simulation parameters include scan rate of  $70 \text{ mV s}^{-1}$ , generation rate of  $4 \times 10^{20} \text{ cm}^{-3} \text{s}^{-1}$ , in addition to those values in **Table S9**.

### S6.6. Interface (perovskite/HTL) charge carrier recombination effects

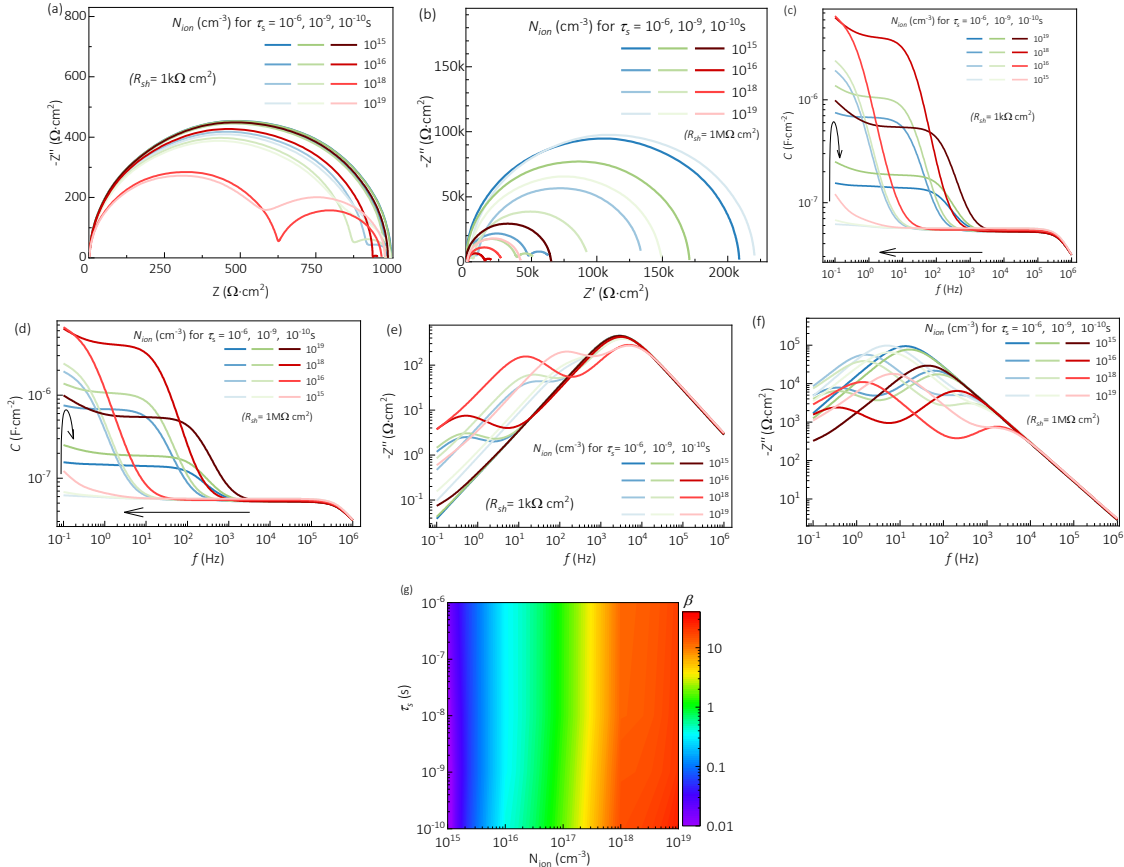


**Figure S48.** Simulated IS spectra in SC for different concentrations of mobile ions and trap recombination lifetime values at the interface considering  $R_{sh} = 1 \text{ k}\Omega \text{ cm}^2$  and  $1 \text{ M}\Omega \text{ cm}^2$ , for the left and right panels, respectively. The resistance frequency ratio in (g) corresponds to the simulations for  $R_{sh} = 1 \text{ M}\Omega \text{ cm}$ . Further simulation parameters are in the **Table S9**.

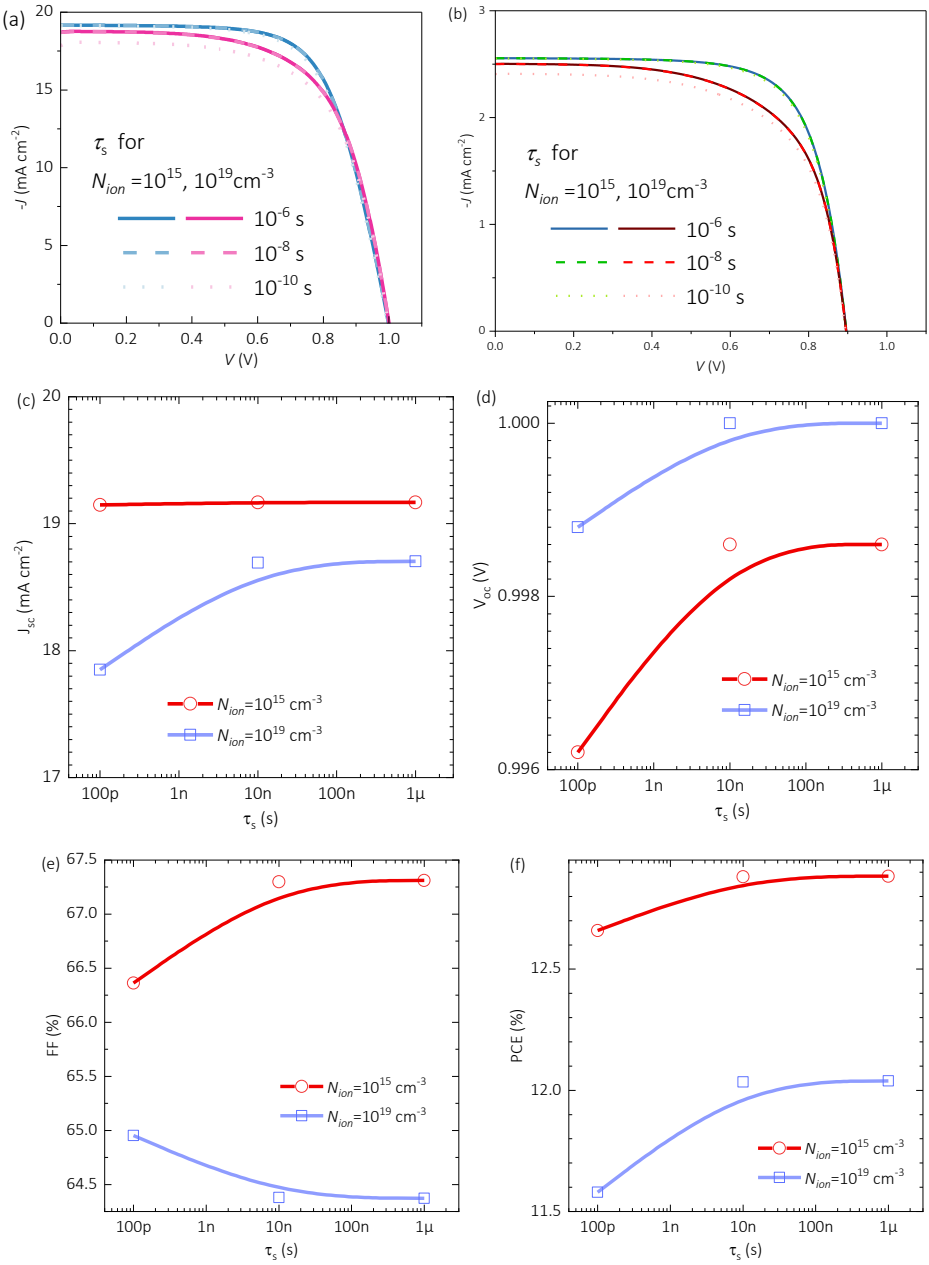


**Figure S49.** Simulated  $J-V$  curve under (a) 1 and (b) 0.2 sun illumination for the ref. sample considering different values of mobile ion concentration and surface recombination lifetime at the interface between the perovskite and the  $\text{NiO}_x$  HTL, as indicated. The simulation parameters include scan rate of  $70 \text{ mV s}^{-1}$ , generation rate of  $2 \times 10^{21} \text{ cm}^{-3} \text{s}^{-1}$ , in addition to those values in **Table S9**. Performance parameters for (a) and in (c-f).

### S6.7. Electron/hole/anion mobility (of the perovskite) effects

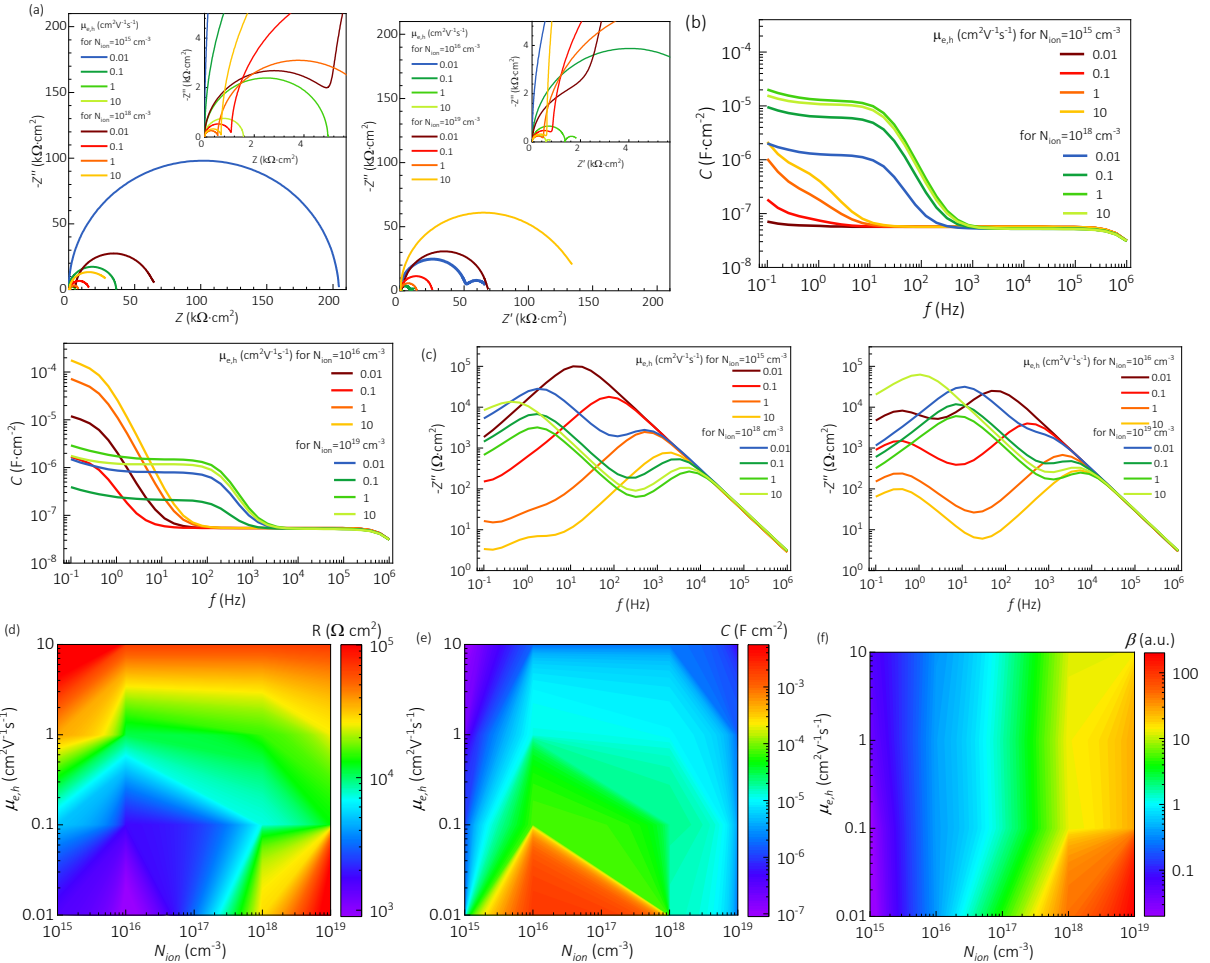


**Figure S50.** Simulated IS spectra in (a) Nyquist and Bode plots of (b) capacitance and (c) imaginary part of impedance considering different mobile ion concentration and electron/hole mobilities in the perovskite, as indicated. The contour plots summarize the resulting total (d) resistance, (e) capacitance and (f) frequency resistance factor. The simulation parameters include  $R_{\text{sh}} = 1 \text{ M}\Omega$ , in addition to those parameters in the **Table S9**.

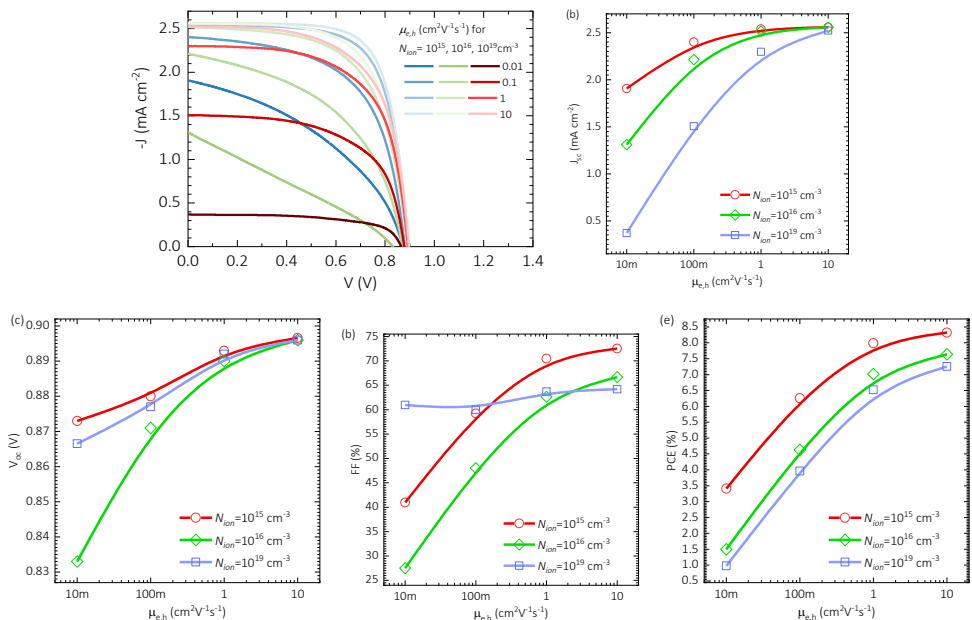


**Figure S51.** Simulated current-voltage curves for the reference sample under 0.2 sun illumination intensity considering different mobile ion concentration and electron and hole mobilities in the perovskite bulk, as

indicated. The performance parameters of (a) are summarized in (b-e). Further simulation parameters can be found in the **Table S9**.

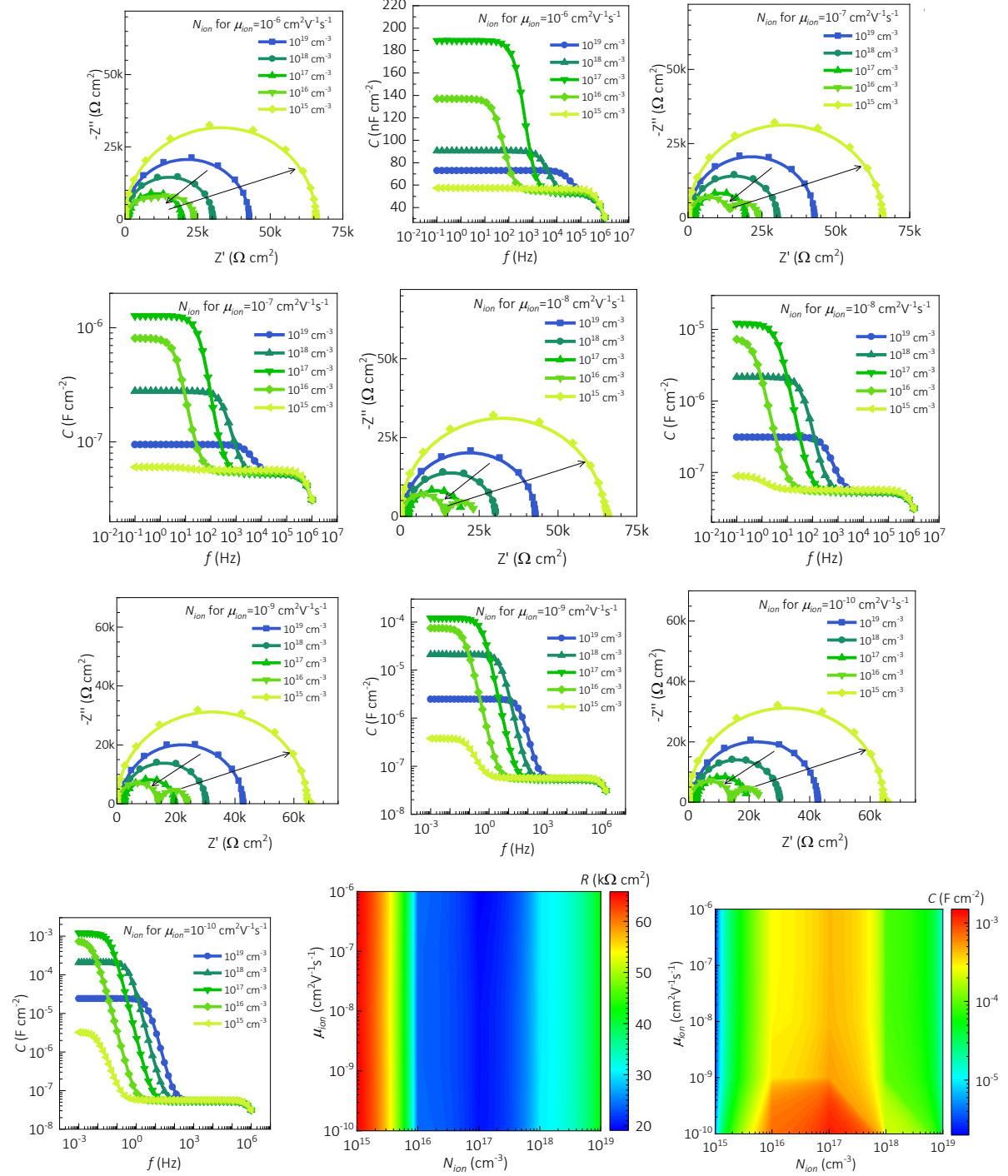


**Figure S52.** Simulated impedance spectra in Nyquist and capacitance Bode plots for different mobile ion concentration and mobility in the perovskite, as indicated. The lower panel summarizes total capacitance and resistance in contour plots. The same concentration and mobility is considered for both the anions and cations. The simulation parameters include  $R_{sh} = 1 \text{ M}\Omega$ , in addition to those parameters in the **Table S9**.

## S6.8. Hole mobility effects at the NiO<sub>x</sub> hole transport layer

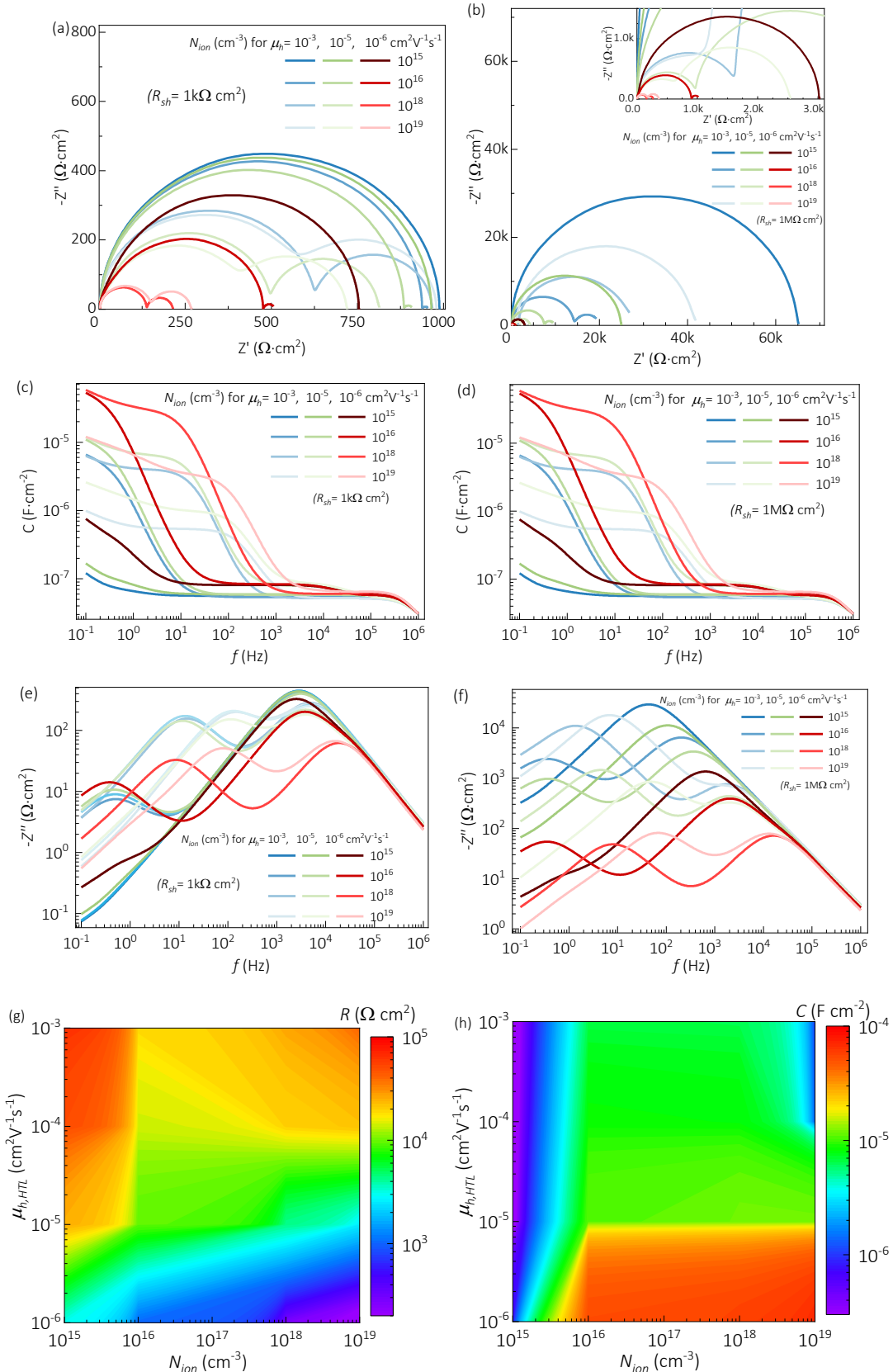


**Figure S53.** Simulated impedance spectra in SC for different concentrations of mobile ions, shunt resistance and hole mobility at the hole transport layer, as indicated. The total resistance and capacitance for the simulations with  $R_{sh}=1\text{M}\Omega\text{cm}^2$  are in (g) and (h), respectively. The simulation parameters are in the **Table S9**.

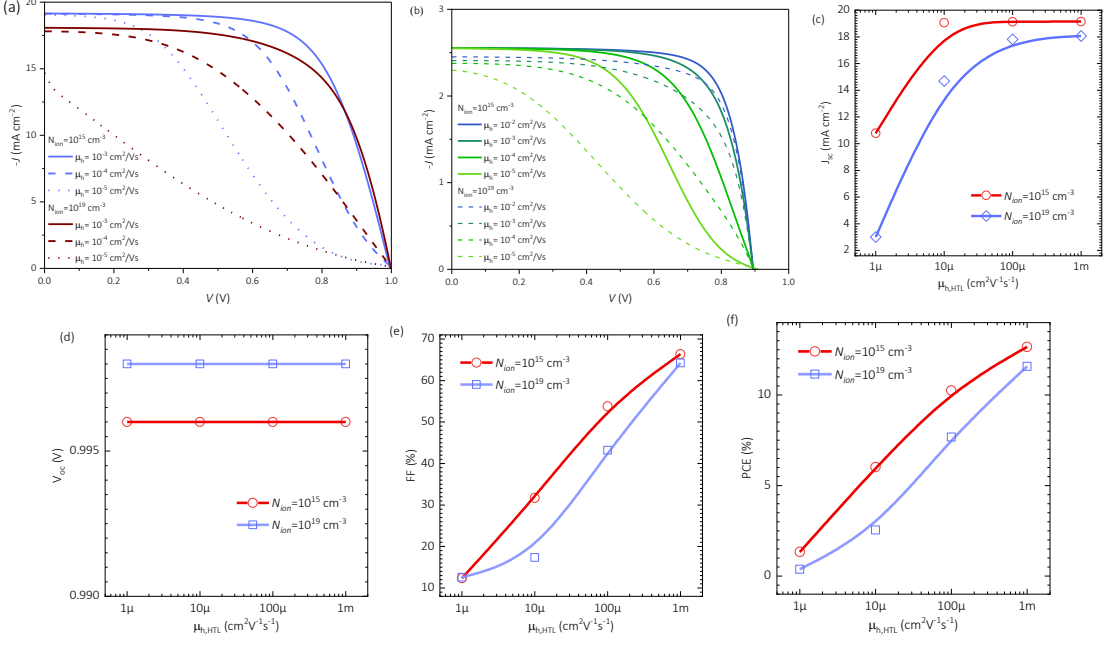


**Figure S54.** Simulated current-voltage curve under (a) 1 and (b) 0.2 sun illumination for the reference sample in SC considering different values of mobile ion concentration and hole mobility at the  $\text{NiO}_x$  transport layer, as indicated. The performance parameters for (a-f) are in (c-f). The simulation parameters include scan rate of 70 mV s<sup>-1</sup>, generation rate of  $2 \times 10^{21} \text{ cm}^{-3}\text{s}^{-1}$ , shunt resistance of  $1\text{M}\Omega\text{cm}^2$ , in addition to those values in **Table S9**.

### S6.9. Dielectric permittivity (of the perovskite) effects

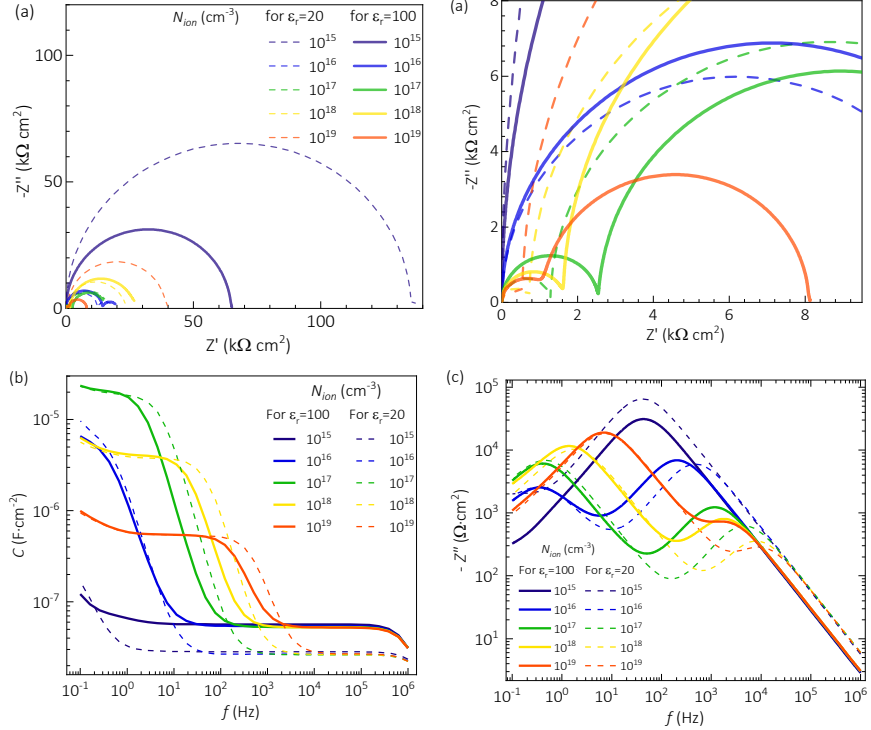


**Figure S55.** Simulated impedance spectra in (a) Nyquist and Bode plots of (b) capacitance and (c) imaginary part or impedance for the reference sample considering different mobile ion concentrations and dielectric permittivity of the perovskite, as indicated. The lower the mobile ion concentration the stronger the influence of the dielectric permittivity. The simulation parameters include  $R_{sh}=1 \text{ M}\Omega \text{cm}^2$ , besides those in **Table S9**.

## Acknowledgment

J.A.A acknowledges the Ministerio de Ciencia e Innovación of Spain, Agencia Estatal de Investigación (AEI) and EU (FEDER) under grants PID2019-110430GB-C22 and PCI2019-111839-2 (SCALEUP). O.A. thanks the AEI of Spain for the Juan de la Cierva Fellowship grant 2021 (FJC2021-046887-I). P.L.V. thanks the French Government in the frame of the program of investment for the future (Programme d'Investissement d'Avenir – ANR-IEED-002-01). J.M. and S.O. thank the Ministry of Economic Affairs Innovation, Digitalization and Energy of the State of North Rhine-Westphalia for funding under the grant SCALEUP (SOLAR-ERA.NET Cofund 2, id: 32).

## References

- [1] SETFOS: Simulation Software for Organic and Perovskite Solar Cells and LEDs, <https://www.fluxim.com/setfos-intro>, accessed: 28.03.2024.
- [2] Philip Calado, Ilario Gelmetti, Benjamin Hilton, Mohammed Azzouzi, Jenny Nelson, Piers R. F. Barnes, Driftfusion: an open source code for simulating ordered semiconductor devices with mixed ionic-electronic conducting materials in one dimension, *J. Comput. Electron.* **2022**, 21, 960, <https://doi.org/10.1007/s10825-021-01827-z>
- [3] Firoz Khan, Seong-Ho Baek, Jae Hyun Kim, Intensity dependency of photovoltaic cell parameters under high illumination conditions: An analysis, *Appl. Energy* **2014**, 133, 356, <https://doi.org/10.1016/j.apenergy.2014.07.107>
- [4] S. N. Agbo, T. Merdzhanova, U. Rau, O. Astakhov, Illumination intensity and spectrum-dependent performance of thin-film silicon single and multijunction solar cells, *Sol. Energy Mater. Sol. Cells* **2017**, 159, 427, <https://doi.org/10.1016/j.solmat.2016.09.039>
- [5] M. Chegaar, A. Hamzaoui, A. Namoda, P. Petit, M. Aillerie, A. Herguth, Effect of Illumination Intensity on Solar Cells Parameters, *Energy Procedia* **2013**, 36, 722, <https://doi.org/10.1016/j.egypro.2013.07.084>
- [6] Firoz Khan, S. N. Singh, M. Husain, Effect of illumination intensity on cell parameters of a silicon solar cell, *Sol. Energy Mater. Sol. Cells* **2010**, 94, 1473, <https://doi.org/10.1016/j.solmat.2010.03.018>
- [7] Kai Shen, Qiang Li, Dezhao Wang, Ruilong Yang, Yi Deng, Ming-Jer Jeng, Deliang Wang, CdTe solar cell performance under low-intensity light irradiance, *Sol. Energy Mater. Sol. Cells* **2016**, 144, 472, <https://doi.org/10.1016/j.solmat.2015.09.043>
- [8] Dana Lübke, Paula Hartnagel, Markus Hülsbeck, Thomas Kirchartz, Understanding the Thickness and Light-Intensity Dependent Performance of Green-Solvent Processed Organic Solar Cells, *ACS Materials Au* **2023**, 3, 215, <https://doi.org/10.1021/acsmaterialsaу.2c00070>
- [9] John Mohanraj, Bipasa Samanta, Osbel Almora, Renán Escalante, Lluis Marsal, Sandra Jenatsch, Arno Gadola, Beat Ruhstaller, Juan Anta, Maytal Caspary Toroker, Selina Olthof, NiO<sub>x</sub> Passivation in Perovskite Solar Cells: From Surface Reactivity to Device Performance, **2024**, <http://arxiv.org/abs/2402.10286>
- [10] Osbel Almora, Gebhard J. Matt, Albert These, Andrii Kanak, Ievgen Levchuk, Shreetu Shrestha, Andres Osvet, Christoph J. Brabec, Germà Garcia-Belmonte, Surface versus Bulk Currents and Ionic Space-Charge Effects in CsPbBr<sub>3</sub> Single Crystals, *J. Phys. Chem. Lett.* **2022**, 13, 3824, <https://doi.org/10.1021/acs.jpclett.2c00804>